

ÉCOLE DOCTORALE /
DOCTORAL SCHOOL

PROGRAMME DOCTORAL EN PHYSIQUE /
DOCTORAL PROGRAM IN PHYSICS



ÉCOLE POLYTECHNIQUE
FÉDÉRALE DE LAUSANNE

Development of a Millikelvin Scanning Tunneling Microscope for Applications in Ultra High Vacuum and High Magnetic Fields

Stuttgart, October 19, 2011

Maximilian Assig

Abstract

In this thesis we discuss the realization of a scanning tunneling microscope (STM) operating at temperatures below 20 mK. This is accomplished by attaching the STM to a dilution refrigerator. We can apply high magnetic fields up to 14 T perpendicular and 0.5 T parallel to the sample surface. A full ultra high vacuum (UHV) preparation chamber is attached to the cryostat allowing *in situ* preparation of the samples to investigate. This setup allows us to investigate low temperature phase transitions in solids and offers the possibility for ultimate energy resolution tunneling spectroscopy measurements on the atomic scale.

The concept of realizing the mK-STM is given. A main point of concern was the design of the STM unit. The choice of materials should be well adapted for the use at very low temperatures and in high magnetic fields. A special concern are thermal expansion coefficients and thermal conductivity. In addition, we analyzed the variation of the tip sample distance for a given external excitation for our STM design and two variations of the Besoke-STM by using a one dimensional mass spring model. This gives us the possibility to extract an optimization criterion for our design to limit the response of the tip sample distance to vibrations that are transmitted to the STM. The external damping mechanism, which ensures a low mutual vibration level of the STM as well as the grounding concept for the electronics are explained.

To characterize the STM at operating temperatures of 1.5 K, 800 mK and 15 mK we measured topography images of Au(111) and Cu(111) surfaces. This allows us to extract the stability between tip and sample. A statistical analysis of the noise in the tunneling current without activated feedback loop yields a stability of 2.7 ± 0.1 pm in a frequency range $f \approx 0.03 - 25$ Hz at 800 mK. To verify if tip and sample are cooled efficiently, we measured the temperature at their positions with additional thermometers. We achieved 17 mK at the tip and 20 mK at the sample position, respectively. The energy resolution of the STM setup was verified by taking tunneling spectra between a superconductor and a normal conducting metal. These spectra could be fitted using the BCS theory of superconductivity. From those fits we can extract the upper limit of the effective temperature of the electrons which is $T_{\text{eff}} = 87 \pm 3$ mK for our best measurement. This corresponds to an energy resolution of $3.5k_bT_{\text{eff}} = 26 \pm 1$ μ eV.

Further, the tunneling conductance between two superconductors was investigated. A sub-gap structure, which can be related to Andreev reflections in asymmetric tunneling junction was observed. In addition, at zero bias voltage a peak due to the Josephson effect can be measured. Side peaks with intensities that scale with this zero bias conductance peak appear most probably due to the interaction of Cooper pairs with the electromagnetic environment in which the junction is placed.

Investigating the dependence of the conductance between a superconducting tip and a normal conducting sample on externally applied magnetic fields leads to the appearance of shoulders in the coherence peaks. These shoulders shift linearly with the external magnetic field. Such an effect has been measured for planar tunnel junctions and can be explained with the lifting of the spin degeneracy of the quasi-particle density of states in a supercon-

ductor. It was observed for the first time by Meservey, Tedrow and Fulde. The fact, that we are now able to prepare STM tips showing the Meservey-Tedrow-Fulde effect enables us to measure the absolute spin polarization at E_F with atomic resolution.

Keywords: Scanning Tunneling Microscopy
tunneling spectroscopy
superconductors
Josephson effect
Andreev reflections
Meservey-Tedrow-Fulde effect
spin splitting of the quasi-particle density of states
very low temperatures
dilution refrigeration

Zusammenfassung

Im Rahmen dieser Arbeit wird die Realisierung eines Rastertunnelmikroskops (RTM) diskutiert, welches bei Temperaturen unter 20 mK arbeitet. Das RTM wird dazu an einen Mischkryostaten angeschlossen. Die Probe kann hohen Magnetfelder bis zu 14 T senkrecht und 0.5 T parallel zu der Probenoberfläche ausgesetzt werden. Eine Ultrahochvakuumkammer ist mit dem Kryostaten verbunden, was uns ermöglicht, die zu untersuchenden Proben *in situ* herzustellen. Dieser Versuchsaufbau erlaubt uns Phasenübergänge zu messen, die bei tiefen Temperaturen auftreten, sowie tunnelspektroskopische Experimente mit ultimativer Energieauflösung vorzunehmen.

Es wird das Konzept zur Realisierung des mK-RTMs erklärt. Einer der Hauptpunkte, auf die wir uns konzentriert haben, ist das Design des Rastertunnelmikroskops. Die Materialien müssen für die Verwendung bei tiefen Temperaturen und in hohen Magnetfeldern geeignet sein. Es ist wichtig, thermische Ausdehnungskoeffizienten sowie thermische Leitfähigkeiten zu berücksichtigen. Desweiteren wurde die Variation im Abstand zwischen Spitze und Probe von unserem RTM Design, sowie für zwei Varianten des Besoke-RTMs, mit einem einfachen eindimensionalen Massemodell für eine gegebene äussere Anregung analysiert. Mit dieser Analyse haben wir die Möglichkeit, ein Optimierungskriterium für unser RTM Design zu formulieren, welches den Effekt von externen Schwingungen auf den Abstand zwischen Probe und Spitze minimiert. Desweiteren wird das Dämpfungskonzept erläutert und das Erdungsschema erklärt.

Für die Charakterisierung des mK-RTMs bei üblichen Arbeitstemperaturen von 1.5 K, 800 mK und 15 mK wurden Bilder der Oberflächen von Au(111) und Cu(111) gemessen. Diese Messungen erlauben, die Stabilität zwischen Probe und Spitze abzuschätzen. Eine Analyse des Tunnelstroms mit geöffneter Regelschleife des RTMs resultiert in einer Stabilität von 2.7 ± 0.1 pm in einem Frequenzbereich von $f \approx 0.03 - 25$ Hz bei 800 mK. Um die effiziente Kühlung von Probe und Spitze zu testen, wurden zwei zusätzliche Thermometer an deren Positionen angebracht. Es wurde eine Temperatur von 17 mK direkt an der Spitze und 20 mK an der Probe gemessen. Die Energieauflösung des RTMs wurde durch tunnelspektroskopische Messungen zwischen einem Supraleiter und einem normalleitenden Metall bestimmt. Zur Modellierung der Spektren wurde die BCS Theorie der Supraleitung benutzt und so eine obere Grenze für die effektive Temperatur der Elektronen abgeschätzt. Aus unserer besten Messung konnte so eine effektive Temperatur von $T_{\text{eff}} = 87 \pm 3$ mK bestimmt werden, was einer Energieauflösung von $3.5k_B T_{\text{eff}} = 26 \pm 1$ μeV entspricht.

Desweiteren wurde die Tunnelleitfähigkeit zwischen zwei Supraleitern untersucht. Eine Peakstruktur wurde in der Energielücke gemessen, die mit Andreev Reflektionen in asymmetrischen Tunnelkontakten erklärt werden kann. Zusätzlich wurde ein Peak bei null Volt angelegter Spannung gemessen, der von dem Josephson Strom herrührt. Zu beiden Seiten dieses Peaks wurden Seitenpeaks gemessen, die mit dem Josephson Peak skalieren und höchstwahrscheinlich durch die Wechselwirkung der Cooper Paare mit der elektromagnetischen Umgebung, in die der Tunnelübergang eingebettet ist, erklärt werden können.

Bei höheren äusseren Magnetfeldern bilden sich in der Leitfähigkeit, zwischen einem Supraleiter und einem Normalleiter, Schultern in der Zustandsdichte der Quasiteilchen

aus. Diese Schultern ändern sich linear mit dem äusseren magnetischen Feld. Dieser Effekt wurde in planaren Tunnelübergängen durch Meservey, Tedrow und Fulde entdeckt. Mit der Verwendung von RTM Spitzen, die den Meservey-Tedrow-Fulde Effekt zeigen, ergibt sich die Möglichkeit, die absolute Elektronenspinpolarisation einer Probe an der Fermienergie auf atomarer Skala, zu messen.

Stichwörter: Rastertunnelmikroskopie
Tunnelspektroskopie
Supraleiter
Josephson Effekt
Andreev Reflektionen
Meservey-Tedrow-Fulde Effekt
Spinaufspaltung der Zustandsdichte von Quasiteilchen
Tiefsttemperaturen
Entmischungskühlung

Contents

1	Introduction	9
2	Scanning Tunneling Microscopy (STM)	13
2.1	Theory of Scanning Tunneling Microscopy	15
2.2	Spectroscopy and electronic resolution	17
2.3	Experimental basics	19
3	Theory of Superconductivity	23
3.1	BCS theory of superconductivity	24
3.2	Andreev reflections	27
3.3	Josephson effect	29
4	Refrigeration below 100mK: Dilution Refrigeration	33
4.1	Physical properties of ^3He and ^4He	34
4.2	Mixtures containing of ^3He and ^4He	34
4.3	Working principle and main components of a dilution refrigerator	38
4.4	Custom designed dilution refrigerator adapted for scanning probe experiments	42
4.5	Thermometry below 100mK	47
4.6	Cooling power and performance of the system	54
5	Realization of the mK-STM	59
5.1	Optimization criteria for an STM	60
5.2	STM unit	72
5.3	Tip and sample transfer mechanism	76
5.4	Link structure	77
5.5	Wiring of cryostat and STM	78
5.6	UHV system	81
5.7	Vibration isolation system	82
5.8	Electronics and filtering	86
5.9	Tests systems for the STM head	89
6	Performance of the mK-STM	91
6.1	Mechanical stability	91

Contents

6.2	Temperature at tip and sample	96
6.3	Electronic resolution	97
7	Measurements with Superconductors	103
7.1	Tunneling measurements between a V tip and a V sample	104
7.2	Lifting the spin degeneracy of a quasi-particle density of states on the local scale	111
8	Summary and Outlook	117
8.1	Spin polarized tunneling using the Meservey-Tedrow-Fulde effect	118
8.2	Measuring the hyperfine interaction of single atoms on the local scale . . .	119
A	Abbreviations and Symbols	121
B	Component models and companies	123
	Bibliography	124
	Curriculum Vitae	133
	Acknowledgments	135

Chapter 1

Introduction

This year we celebrate the 100th birthday of superconductivity. In 1911, the Dutch physicist Heike Kamerlingh-Onnes investigated the low temperature resistance of mercury when he found a sudden drop to zero when it was cooled to temperatures below 4.2K [1]. This effect was named superconductivity and marked the beginning of a new field in physics. At this time the phenomenon was totally unexpected and theoretical methods to explain it were still missing. The theory of quantum mechanics had to be developed and based on it Bardeen, Cooper and Schrieffer formulated in 1957 a microscopic theory which could explain the phenomena related to superconductivity [2]. In short, two electrons can couple via an attractive interaction mediated by phonons to the so called Cooper pairs. These Cooper pairs are of bosonic nature.

Related to superconductivity is an effect first described by Meservey, Tedrow and Fulde in 1970 [3]. In superconducting 5 nm thin aluminum films the density of states of electrons that are excited out of Cooper pairs (quasi-particles) can split into a spin up and spin down part when external magnetic fields are applied. The energy shift of the spin separated densities of states (DOS) scales with the external magnetic field due to a rather small Zeeman interaction. For example, an applied magnetic field of 1T leads to an energy separation of $2\mu_B B \approx 114 \mu\text{eV}$ for the two spin parts of the DOS. When using such an aluminum film in a tunneling experiment where the second electrode is a ferromagnetic material, the probability for tunneling into the spin polarized states of the Al film depends on the initial spin state of the tunneling electron [4]. If no spin flip processes occur in the tunneling barrier this method gives an absolute probe for the spin polarization of the ferromagnetic electrode. Instead of planar tunneling junctions it should also be possible to use a scanning tunneling microscope (STM) for detecting this effect which however has not been reported yet.

Adapting the effect of Meservey, Tedrow and Fulde in an STM [5–7] would provide the capability to measure the absolute magnetization of a spin polarized nanostructure on the local scale. To realize this, a superconducting STM tip has to be used in externally applied magnetic fields. For such an experiment a high energy resolution of the STM setup is required to resolve the lifting of spin degeneracy already at moderate magnetic fields. This energy resolution can be achieved by cooling the STM to very low temperatures.

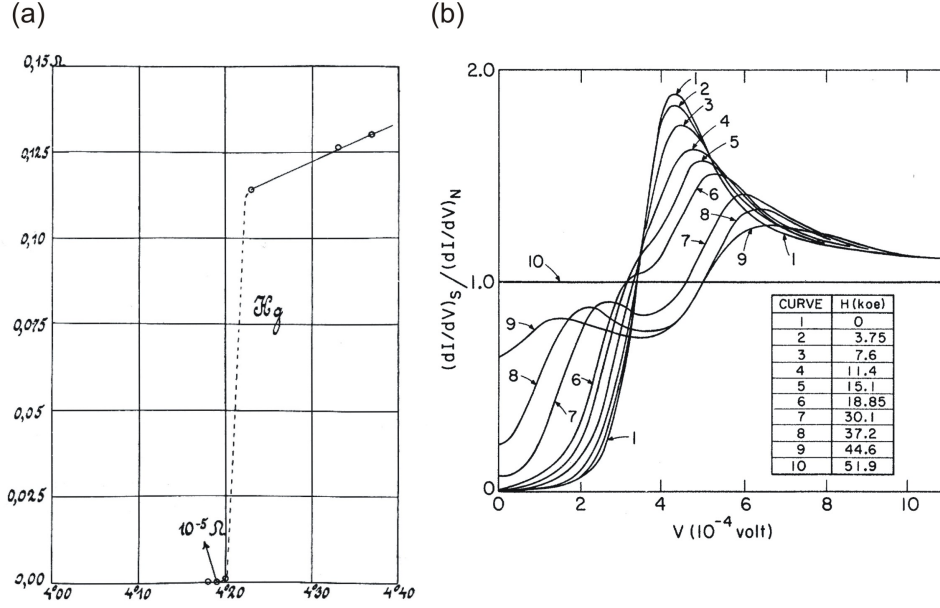


Figure 1.1: Pioneering measurements with superconductors. (a) The resistance drop in mercury observed by Heike Kamerlingh-Onnes [1]. (b) Splitting of the quasi-particle density of states of thin Al films in a magnetic field reported by Meservey, Tedrow and Fulde [3].

We have developed an STM experiment which can be cooled to temperatures below 20 mK by attaching the STM unit to the mixing chamber of a dilution refrigerator. The refrigerator is compatible to ultra high vacuum (UHV) and a full UHV sample preparation unit is attached to it. This allows *in situ* preparation of the samples to investigate [8]. Magnetic fields of 14 T perpendicular and 0.5 T parallel to the sample surface can be applied. Systems that combine an STM with a dilution refrigerator have been reported in the literature, but most of them are not attached to a UHV sample preparation chamber [9–11]. Thus, samples that are investigated are limited to layered materials that have to be cleaved in cryogenic vacuum in order to have a clean surface for STM measurements. So far only two systems that combine mK temperatures, UHV preparation and high magnetic fields have been reported by Matsui *et al.* [12] and Song *et al.* [13].

The thesis is organized as follows. The basics of STM are given in Chap. 2. The theory which is used for modeling tunneling spectra is explained. The main principles of measuring the local density of states and the energy resolution expected from a spectroscopic measurement are derived.

An introduction into superconductivity is given in Chap. 3. The BCS model is introduced and a corresponding fitting formula for the tunneling conductance between a normal conducting sample and a superconducting tip is derived. In addition, effects that are important for the explanation of tunneling spectra involving two superconductors like the sub-gap structure and the Josephson effect are described.

Chap. 4 summarizes the physics and technology which is needed to cool an experiment

to temperatures below 20 mK. Special features of our dilution cryostat are mentioned and the temperature calibration of our thermometers is shown. This chapter concludes with measurements of the base temperature and the cooling power of the cryostat.

A detailed description of the different parts of the mK-STM system is given in Chap. 5. Here the STM unit, our solution for an easy and reliable tip and sample transfer, the UHV preparation system and the electronic setup are explained. Measurements from various test systems that were set up during this project are given in the last section of this chapter.

The performance concerning scanning stability and energy resolution is shown in Chap. 6. STM topographs are given at various temperatures demonstrating the mechanical stability of our mK-STM system. To estimate the temperature, which is directly at tip and sample position, we use pre-calibrated resistive thermometers placed in the STM unit instead of a tip and sample. The temperature evolution at these spots is measured when a small sine waveform is applied to the z electrode of the scanning piezo. For extracting the effective temperature of the electrons in the tunneling junction the quasi-particle density of states of an aluminum superconductor is measured. By using BCS theory to fit these results an effective temperature which is related to the electronic resolution is obtained.

In Chap. 7 measurements on superconductors at temperatures of 800 mK and 15 mK are shown. We use vanadium as tip and sample material which becomes superconducting at a temperature of 5.4 K. The superconductor-vacuum-superconductor junction was investigated at various normal state tunneling resistances R_N . Finally we applied a magnetic field such, that the bulk vanadium crystal lost the superconductivity and only the superconducting tip remained. We investigated the dependence of the quasi-particle density of states on externally applied magnetic fields. For the first time we could observe the Meservey-Tedrow-Fulde effect with an STM.

Chapter 2

Scanning Tunneling Microscopy (STM)

Scanning Tunneling Microscopy (STM) is a method to study structural and electronic properties of single atoms and molecules on surfaces with atomic spacial resolution [5–7]. An atomically sharp metal probe (tip) is moved close to a conducting or semiconducting surface (sample) with a voltage applied between them (Fig. 2.1). Even though, tip and sample are not in electrical contact a current flow is detected which depends exponentially on their spacing. In general, a shorter distance between tip and sample leads to a higher current flow. To keep the distance fixed, the current is recorded and deviations from a fixed set-point value lead to corrections in the height of the tip above the sample. While the tip is moved line by line across the sample, these corrections correspond to the surface profile of the sample and are used to construct an image of it.

The phenomenon of detecting a current without mechanical contact is called tunnel effect. This quantum mechanical effect describes the probability of finding an electron in a region of space, which would under classical aspects not be allowed¹. Assuming tip and sample are in electrical equilibrium (no voltage is applied between them) both Fermi energies are equal with respect to the vacuum level (Fig. 2.2(a)). Only thermally activated tunneling of electrons across the potential barrier is possible. A current flow in this case is not detected. The work functions in Fig. 2.2 are equal which is not necessary for the general case. If a positive voltage is applied to the sample the combined system is not in equilibrium anymore. The densities of states in both electrodes are shifted with respect to each other as indicated in Fig. 2.2 (b). Electrons tunnel from occupied tip states into unoccupied states of the sample. A current is detected due to the potential difference between the electrodes. The situation reverses when the applied sample bias is negative (Fig. 2.2 (c)). Now, the energy shift has changed the sign and electrons tunnel from occupied states of the sample into unoccupied states of the tip.

In the following the theory of STM is described. In Sec. 2.1 the tunneling process and basic steps for deriving the tunneling current are discussed. This includes the Bardeen approximation and the Tersoff-Hamann model for tunneling between a sharp tip and a

¹ The tunneling effect was first observed during field emission of electrons in vacuum by R.W. Wood in 1897. In nuclear physics it was used to explain the decay of radioactive elements by Rutherford in 1902.

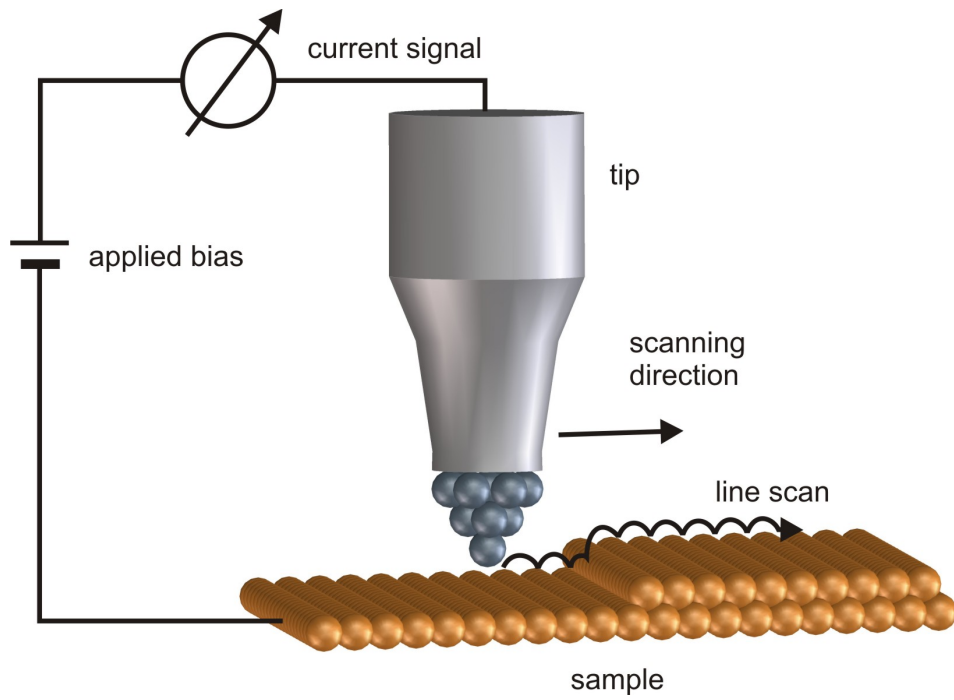


Figure 2.1: Principal schematic of STM.

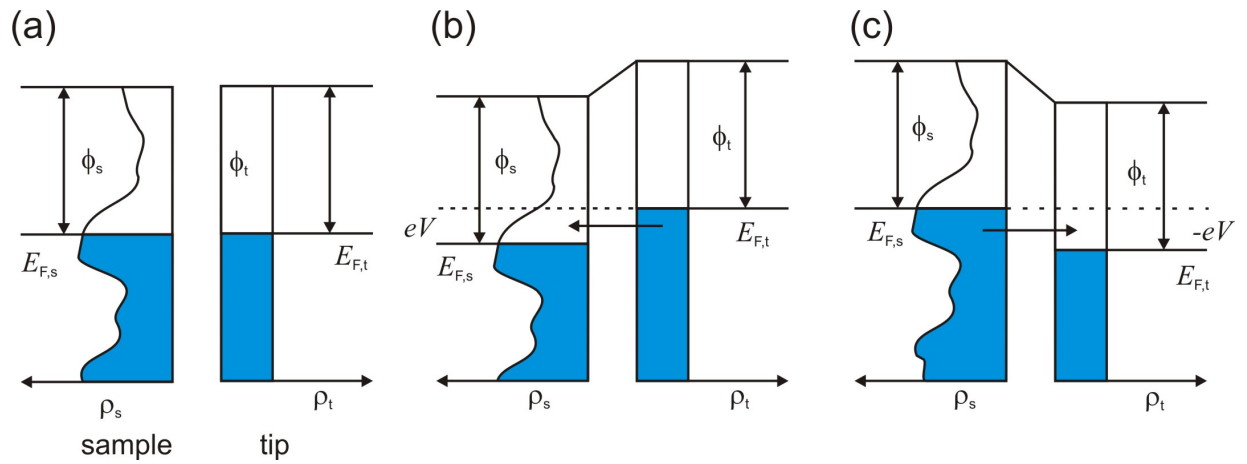


Figure 2.2: Energy scheme of the tunneling process. (a) No bias voltage is applied between the two electrodes. (b) Positive bias applied to the sample with respect to the tip. (c) Negative bias applied to the sample with respect to the tip.

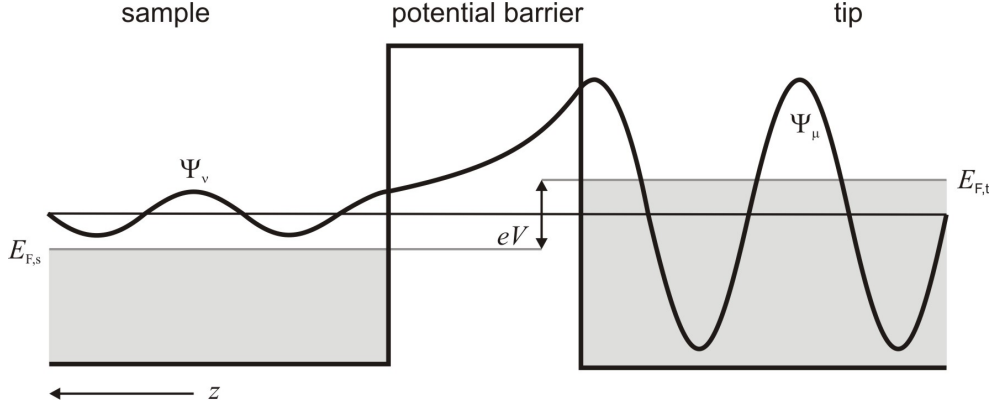


Figure 2.3: Tunneling between two discrete energy states. An electron tunnels from an occupied tip state ψ_μ (right hand side of the potential barrier) into an unoccupied sample state ψ_ν (left hand side of the potential barrier).

surface. The spectroscopy mode of STM and how the density of states of the sample can be measured is described in Sec. 2.2. A brief overview of the experimental basics is given in Sec. 2.3.

2.1 Theory of Scanning Tunneling Microscopy

In a tunneling experiment, electrons in tip and sample experience a potential barrier due to the vacuum between the two. In Fig. 2.3 the scheme of tunneling between two discrete electron states is shown. An electron enters the potential barrier from an occupied tip state. The probability density of observing it at a place z inside the potential barrier is

$$|\psi(z)|^2 = |\psi(0)|^2 e^{-2\kappa z}, \quad \kappa = \sqrt{\frac{m_0}{\hbar} (\phi_t + \phi_s - eV_t)}. \quad (2.1)$$

The electron mass in the rest frame is m_0 , \hbar the Planck constant, ϕ_t and ϕ_s the work functions of tip and sample and V a voltage applied between tip and sample. The work functions are in the order of 5 eV for metals [14]. The electron is transmitted to an unoccupied state at the other side of the potential barrier ψ_ν having a lower, but not vanishing probability density. According to Equ. 2.1 the probability density changes an order of magnitude when the distance z is increased about 0.1 nm.

Bardeen formalism

An elegant formalism of describing the tunneling between two electrodes was developed by Bardeen [15] describing experiments with planar tunneling junctions by Giaever [16]. He approached the problem by introducing two separated subsystems instead of solving the

combined system of two electrodes separated by a tunneling barrier. Using time dependent perturbation theory he could calculate the rate of transferring an electron from an occupied state in one electrode ψ_μ to an unoccupied state in the other electrode ψ_ν . The tunneling matrix element $M_{\mu\nu}$ is only proportional to the overlap of the wave functions of both states at an arbitrary separation surface between the two electrodes

$$M_{\mu\nu} = -\frac{\hbar^2}{2m} \int d\vec{S} (\psi_\mu^* \nabla \psi_\nu - \psi_\nu \nabla \psi_\mu^*) . \quad (2.2)$$

It can be used to calculate the tunneling probability between the states ψ_μ and ψ_ν . Summing over all states and taking the occupation probability into account gives the tunneling current

$$I = \frac{4\pi e}{\hbar} \sum_{\mu\nu} (f(E_\mu) - f(E_\nu)) |M_{\mu\nu}|^2 \delta(E_\mu - E_\nu - eV) \quad (2.3)$$

where $f(E, T) = 1/(1 + \exp(E/k_B T))$ is the Fermi function which describes the distribution of the electrons within the available energy states in one electrode as a function of temperature T . All energies are given with respect to the corresponding Fermi energies. Using the density of states $\rho_t(E) = \sum_\mu |\psi_\mu|^2 \delta(E_\mu - E)$ and $\rho_s(E) = \sum_\nu |\psi_\nu|^2 \delta(E_\nu - E)$ instead of the discrete states ψ_μ and ψ_ν the tunneling current reads

$$I = \frac{4\pi e}{\hbar} \int_{-\infty}^{\infty} (f(E - eV) - f(E)) \rho_t(E - eV) \rho_s(E) |M_{t,s}(E, V, z)|^2 dE \quad (2.4)$$

where $|M_{t,s}(E, V, z)|^2$ is the matrix element for tunneling between continuous states. In an one dimensional picture $|M_{t,s}|^2$ can be expressed the following way

$$|M_{t,s}(E, V, z)|^2 = \exp \left(-2z \sqrt{\frac{m_e}{\hbar^2} (\phi_t + \phi_s - eV + 2E)} \right) . \quad (2.5)$$

Approximations

Eqs. 2.4 and 2.5 are one dimensional equations for evaluating the tunneling current. Depending on the scientific system to investigate they can be simplified further. As a first point, the work functions of sample ϕ_s and tip ϕ_t can be assumed as equal because quite often the tip is conditioned and shaped by slightly dipping it into the sample surface. This covers the apex with the sample material leading to $\phi_t = \phi_s = \phi$.

If the energy width Γ of a spectroscopic feature is much broader than the thermal energy of tip and sample $\Gamma \gg k_B T$ the Fermi functions can be approximated by step like functions. The tunneling current (Equ. 2.4) can be rewritten in this case to

$$I(V) \sim \int_0^{eV} \rho_s(E) \rho_t(E - eV) |M_{t,s}(E, V, z)|^2 dE \quad (2.6)$$

with the density of states of tip ρ_t and sample ρ_s and the tunneling matrix element $|M_{t,s}(E, V, z)|^2$.

Often the spectroscopic features of interest in ρ_s are close to the Fermi energy. Their energy is small compared to the work functions of tip and sample. This means the work functions ϕ_s and ϕ_t are the dominating energies in the exponential term of Equ. 2.5. In this case we can assume that the tunneling matrix element is constant in energy depending only on z

$$|M_{t,s}(z)|^2 = \exp\left(-2z\sqrt{\frac{m_e}{\hbar^2}(\phi_t + \phi_s)}\right) \quad (2.7)$$

which leads to a simplified expression of the tunneling current

$$I(V) \sim |M_{t,s}(z)|^2 \int_0^{eV} \rho_s(E) \rho_t(E - eV) dE. \quad (2.8)$$

Tersoff-Hamann model of the tunneling matrix element

A simple description of $|M_{t,s}|^2$ for a local tunneling experiment where one electrode consists of a single atom was given by Tersoff and Hamann [17, 18]. They assumed the density of states at the apex of the STM tip as spherical which means that only s -like states contribute to the tunneling process. Furthermore, they made the assumption that the densities of states in both electrodes for the energy interval of interest is constant and only elastic tunneling processes are considered. This yields an analytical expression for the tunneling matrix element

$$M_{t,s} = -\frac{2\pi C \hbar}{\kappa m_0} \psi_\nu(\vec{r}). \quad (2.9)$$

Here C is a constant and κ defined as in Equ. 2.1. The transition matrix element depends only on the wavefunction of the sample at the position \vec{r} of the last tip atom and is independent of the density of states of the tip. At zero temperature ($T=0$ K) and small bias voltages ($V_{\text{Bias}} \ll \phi/e$) the tunneling current is given by a simple formula

$$I = \frac{16\pi^3 C^2 \hbar^3 e}{\kappa^2 m_e^2} \rho_t \int_0^{eV} \rho_s(E) dE. \quad (2.10)$$

2.2 Spectroscopy and electronic resolution

Aside from using the STM as imaging tool, it can be used to perform spectroscopy on a local scale. It gives direct access to the local density of states of surfaces and single atoms or molecules which bind to them [19–24].

Spectroscopy

Starting from Equ. 2.4 the derivative of the tunneling current is

$$\begin{aligned} \frac{dI}{dV} \sim \int_{-\infty}^{\infty} & (-\rho_s(E)\rho'_t(E-eV)f_t(E-eV) \\ & -\rho_s(E)\rho_t(E-eV)f'_t(E-eV) \\ & +\rho_s(E)\rho'_t(E-eV)f_s(E))dE \end{aligned} \quad (2.11)$$

where ρ_t, ρ_s are the densities of states of tip and sample and $f_t(E), f_s(E)$ the corresponding Fermi functions. The first derivative of ρ_t with respect to an energy is

$$\rho'_t(E) = \frac{\partial \rho_t(E)}{\partial E} \quad (2.12)$$

as well as the derivative of the Fermi function $f'_t(E)$

$$\begin{aligned} \frac{\partial f_t(E)}{\partial E} &= -\beta \left(\frac{\exp(\beta E)}{(1 + \exp(\beta E))^2} \right) \\ &= -\beta \frac{1}{\exp(-\beta E) + \exp(\beta E) + 2} \\ &= -\frac{\beta}{4} \operatorname{sech} \left(\frac{1}{2} \beta E \right) \end{aligned} \quad (2.13)$$

with $\beta = 1/k_B T$.

Equ. 2.11 describes the full derivative of the tunneling current. As tip material often metals are used which ideally show no features in the DOS. This leads to the assumption that the DOS is constant in the energy range of interest resulting in $\rho'_t = 0$. Additionally at zero temperature ($T = 0$ K) we find $f'_t(E, T)_{k_B T \rightarrow 0} = -\delta(E)$ where $\delta(E)$ is the Dirac distribution. This gives a simplified expression of Equ. 2.11

$$\frac{dI}{dV} \sim - \int_{-\infty}^{\infty} \rho_s(E)\rho_t(E-eV)\delta_t(E-eV)dE = -\rho_s(eV)\rho_t(0) \quad (2.14)$$

Equation Equ. 2.14 directly relates the first derivative of the tunneling current to the sample DOS. To measure the pure DOS of the sample it is important that ρ_t is constant near E_F . Also the need for very low temperatures becomes obvious: the energy scale of the spectroscopic feature to investigate should be large compared to the thermal energy otherwise $f'_t(E, T) = -\delta(E)$ is not valid any more.

The dI/dV is measured by placing the tip above the object of interest and keeping the distance fixed. The bias, which is applied between tip and sample is ramped through a certain voltage interval. The voltage at the tunneling junction can be related to the energy out of which the electrons tunnel. The first derivative of the tunneling current is recorded with the help of a lock-in amplifier.

Lock-In derivative

As described in the previous section the density of states of the sample is correlated to the first derivative of the tunneling current. In an experiment the first derivative is measured by adding a small modulation voltage V_{mod} to the applied bias signal V . Expanding the current signal in a series of cosine terms [25] gives

$$\begin{aligned} I(V + V_{\text{mod}} \cos(\omega t)) = I(V) &+ \frac{dI}{dV} V_{\text{mod}} \cos(\omega t) \\ &+ \frac{1}{2} \frac{d^2 I}{dV^2} V_{\text{mod}}^2 (1 - \cos(2\omega t)) \end{aligned} \quad (2.15)$$

where ω is the frequency of the modulation voltage. From Equ. 2.15 one recognizes that picking out the signal component which varies with ω gives the first derivative of the current. Analogue the signal component which modulates with 2ω is proportional to the second derivative. These components can be detected by a lock-in amplifier which converts them into a direct voltage that is proportional to their oscillation amplitudes.

Energy resolution

The energy resolution is the minimal distance in energy of two neighboring spectroscopic features which still can be resolved. The total energy resolution ΔE is the sum of a thermal ΔE_{therm} and an instrumental ΔE_{instr} contribution [26]

$$\begin{aligned} \Delta E &= \sqrt{(\Delta E_{\text{therm}})^2 + (\Delta E_{\text{instr}})^2} \\ &\approx \sqrt{(3.5k_B T)^2 + (2.5eV_{\text{mod}})^2}. \end{aligned} \quad (2.16)$$

Here V_{mod} is the amplitude of the modulation voltage which is added to the bias signal in order to measure the first derivative of the tunneling current with a lock-in amplifier. The pre-factor for the thermal broadening changes to 5.4 for inelastic tunneling processes [27, 28]. In Fig. 2.4 Equ. 2.16 is shown for different modulation voltages in the temperature range between 0 to 20 K. If the instrumental part becomes dominant, increasing the energy resolution by decreasing the temperature is not possible any more. The smaller the modulation voltage is, the smaller will be ΔE_{instr} . But decreasing the modulation to much results in less measurement signal. It is always a trade off between the amount of signal one needs for a spectroscopic measurement and the desired energy resolution. As an example, the best energy resolution which can be achieved in a spectroscopy measurement using a bias modulation $V_{\text{mod}} = 10\mu V$ is $25\mu eV$.

2.3 Experimental basics

In this section the main experimental basics are explained. It is done on a general basis because the details of the STM which was developed during this thesis are described in Chap. 5. A simplified scheme of an STM setup is depicted in Fig. 2.5.

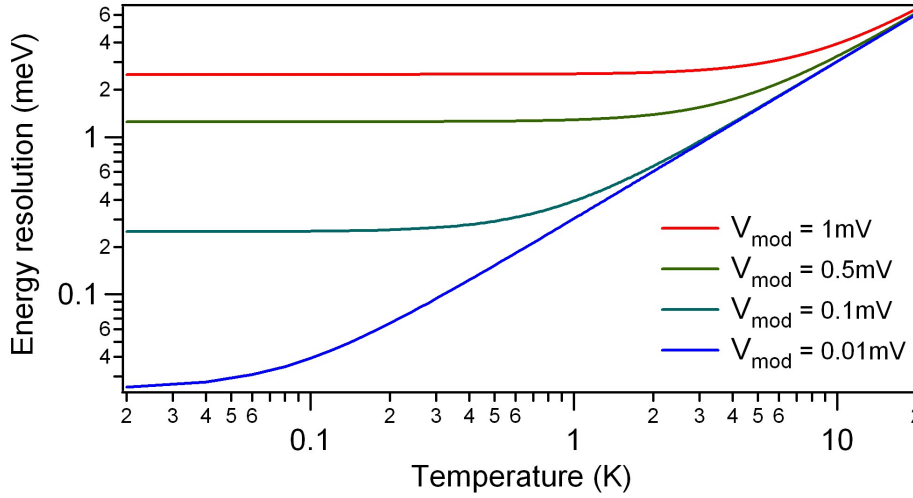


Figure 2.4: Energy resolution in tunneling spectroscopy. The energy resolution is a combination of thermal and instrumental contributions. The experimental contributions are restricted to the broadening due to the modulation voltage added to the direct voltage signal of the bias. A decrease in temperature increases the energy resolution in the tunneling spectroscopy only if the modulation voltage is low enough not to be the dominant contribution in Equ. 2.16.

The STM tip is mounted to a tube piezo (from now on referred to as scanning piezo (SP)) which is used for the precise motion when the tip is in tunneling contact to the sample. The SP is a tube made of a lead zirconate titanate ceramic (PZT)² including a set of electrodes to drive the motion in x,y and z direction. To the electrodes high voltages (HV) are applied to bend, extend or shrink it.

To reach tunneling contact the tip has to overcome a macroscopic distance of approximately 1 to 5 mm, depending on the STM setup. This cannot be done by the SP alone, therefore it is attached to a coarse motor (CM). In literature different approaches for the CM design can be found [29–31]. It depends on the boundary conditions of the setup in which the STM is implemented which one is chosen. Our STM uses a one-dimensional commercial inertial stepper motor based on the principle of the motor proposed by Pohl [32].

The bias signal is generated by an *ex situ* voltage source and is often applied to the sample. The current is detected through the tip, converted into a voltage signal and amplified by an *ex situ* current voltage converter (I-V converter). The amplified current signal is now fed to the input of the control electronics where it is further processed.

The control electronics is used to keep the distance between tip and sample constant. The measured current signal is compared to a fixed set-point value. In a control loop the signal that has to be applied to the z-electrode of the scanning piezo in order to minimize

²PZT is a ceramic perovskite material which was developed by researchers from the Tokyo Institute of Technology in 1952.

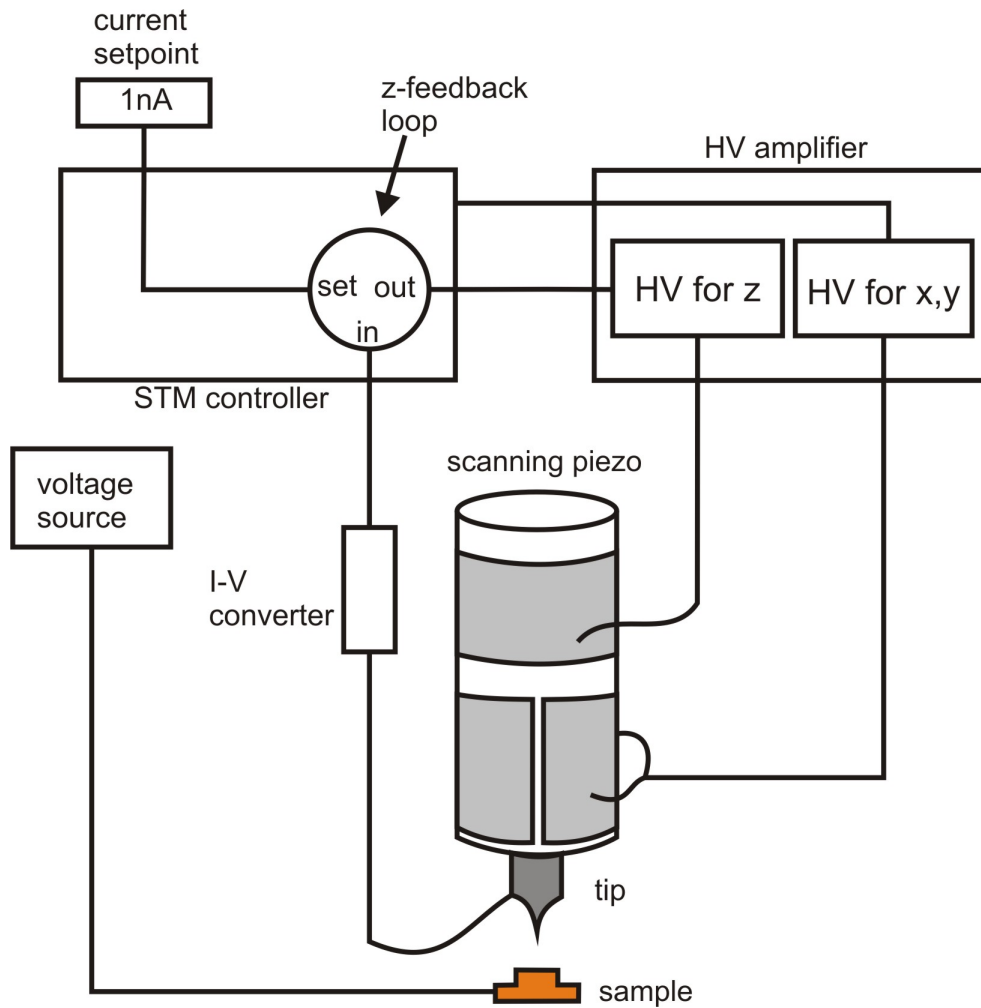


Figure 2.5: Setup of an STM experiment.

the deviation between the measured current signal and the set-point value is estimated. Control signals for the motion of the tip during the scanning process are sent to a HV amplifier generating the appropriate voltages to drive the scanning piezo. Also spectroscopy measurements are performed by the electronics. Here the tip is placed above an object of interest. The feedback loop is opened and the bias is swept through the desired voltage range recording the current and the first derivative.

Chapter 3

Theory of Superconductivity

Superconductivity is the phenomenon of vanishing resistance in metals and metal compounds if they are cooled below a critical temperature T_C . The discovery went hand in hand with great advances in refrigeration technology. The Dutch physicist Heike Kamerlingh-Onnes (1853-1926) succeeded in liquifying ^4He in his lab in Leiden in 1909. This was a main break-through on the way of discovering superconductivity. Two years later, on the 8th of April 1911¹ he observed a sudden drop to zero in the resistance of mercury when it was cooled below 4.2K. With this measurement he set the starting point of a new field in physics. The vanishing resistance is a property, which all superconductors have in common.

A second important property is the Meissner-Ochsenfeld effect [34]. This effect describes the expelling of weak magnetic fields from the superconductor. It can be explained by the formation of screening super-currents \vec{j} . These currents are the origin of an internal magnetization $\nabla \times \vec{M} = \vec{j}$ and a magnetic field $\vec{M} = -\vec{H}$ within the superconducting sample which cancels any external field up to a critical field H_C . This leads to a susceptibility $\chi = dM/dH = -1$. A superconductor is therefore an ideal diamagnet.

The first theory describing both phenomena was given by Fritz and Heinz London [35]. It can be derived on the basis of the classical Drude model for conductivity in metals. The London brothers assumed that the whole density of conduction electrons is composed out of a dissipative n_n and a superconducting part n_s . This leads to the London equations

$$\frac{\partial \vec{j}_s}{\partial t} = \frac{n_s e^2}{m} \vec{E} \quad (3.1)$$

$$\nabla \times \vec{j}_s = -\frac{n_s e^2}{mc} \vec{B} \quad (3.2)$$

where \vec{j}_s is the superconducting current, n_s the density of electrons in the superconducting state, e the elementary charge, m the electron mass, c the speed of light and \vec{E} and \vec{B} the electric as well as the magnetic field.

¹The disappearance of the resistance in mercury was simply stated in the lab books with the entry: "The temperature measurement has been successful. Mercury practically zero". This was the birth of a new branch of physics. Kamerlingh-Onnes and his coworkers also witnessed the suprafluid transition of ^4He at 2.2 K resulting in the observation of two novel and important quantum phenomena in one day [33]!

Superconductors can be classified into the main classes

- Type I superconductors
- Type II superconductors

depending whether they allow the penetration of a finite magnetic field into their bulk or not. An external magnetic field applied to a type I superconductors is completely screened due to the Meissner-Ochsenfeld effect as long as it does not exceed a critical value H_C . At this field strength the superconductivity breaks down and the sample becomes normal conducting. For the case of the type II superconductor, an intermediate state can form for magnetic fields greater than a first H_{C1} but smaller than a second H_{C2} critical field $H_{C1} < H < H_{C2}$. The flux density inside the superconductor increases linearly for these field values. Vortices are formed, around which the supercurrent circulates. The area within the vortices is in a normal state through which the magnetic field can penetrate the superconductor. If a magnetic field $H > H_{C2}$ is applied the superconducting state vanishes. This intermediate state was first described by the Russian physicist Alexei A. Abrikosov [36].

3.1 BCS theory of superconductivity

The first microscopic theory which succeeded in describing superconductivity was presented by Bardeen, Cooper and Schrieffer (BCS) in 1957, 46 years after its discovery [2]. In the early years of superconductivity the quantum mechanical framework for a complete microscopic description was still missing. The main idea behind the BCS theory is the formation of Cooper pairs which can only be explained by quantum mechanics.

An attractive interaction between two electrons added to the Fermi ground state, leads to the formation of a bound state. This bound state can have a lower energy than the energy of the Fermi ground state. The attractive interaction acts only between the two electrons leaving the other electrons of the Fermi sea unaffected. It can be shown that the binding energy between the two electrons is largest when they have opposite wavevectors. The total wavefunction $\psi_{-\vec{k},\vec{k}}$ of the two electrons has to be antisymmetric considering the exchange between them which leads to an antisymmetric spin state resulting in a singlet pairing of the spins [25, 37, 38]. The electrons form a pair with opposite wavevector and spin $(\vec{k} \uparrow, -\vec{k} \downarrow)$.

Now the question arises what the physical origin of the attractive interaction is. First ideas were pointed out by Fröhlich in 1950 [39] followed by a mathematical description by Fröhlich and Bardeen *et al.* [40, 41]. Such an interaction can be realized if the motion of the ionic cores in the solid is considered. On its way through the crystal, a first electron polarizes the medium by attracting the positively charged atomic cores. This results in a small distortion of the crystal which is felt by a second electron. The distortion of the lattice shows, that lattice dynamics including phonon frequencies have to play a role. An electron is scattered from the momentum state \vec{k} to \vec{k}' leading to the momentum the phonon has to

supply $\vec{q} = \vec{k} - \vec{k}'$. The frequency scale for phonon processes in a solid is given by the Debye frequency resulting in typical energies in the order of $\hbar\omega_D$. Therefore, electrons interacting attractively with each other originate from an energy interval $E_F - \hbar\omega_D < E < E_F + \hbar\omega_D$ around the Fermi energy E_F .

Using the probabilities $v_{\vec{k}}$ of finding a Cooper pair ($\vec{k} \uparrow, -\vec{k} \downarrow$) in the occupied state $|1\rangle_{\vec{k}}$ and $u_{\vec{k}}$ for finding it in the unoccupied state $|0\rangle_{\vec{k}}$ (which are in the following reduced to v , $|1\rangle$, u and $|0\rangle$) it is possible to write the two electron wavefunction

$$|\psi\rangle_{\vec{k}} = u|0\rangle + v|1\rangle \quad \text{with} \quad u^2 + v^2 = 1. \quad (3.3)$$

Up to now we just looked at two electrons forming a Cooper pair, but an attractive interaction influences all electrons near the Fermi surface. Including all Cooper pairs that are formed, the BCS ground state is symbolized by the macroscopic wavefunction

$$|\Psi_{\text{BCS}}\rangle = \prod_{\vec{k}} (u|0\rangle + v|1\rangle). \quad (3.4)$$

By using the creation operator $c_{\vec{k}\uparrow}^* c_{-\vec{k}\downarrow}^*$ for creating a Cooper pair in the state ($\vec{k} \uparrow, -\vec{k} \downarrow$) the BCS wave function can be rewritten to

$$|\Psi_{\text{BCS}}\rangle = \prod_{\vec{k}} (u + v c_{\vec{k}\uparrow}^* c_{-\vec{k}\downarrow}^*) |\Psi_0\rangle \quad (3.5)$$

where $|\Psi_0\rangle$ is the vacuum state with no Cooper pairs present. The probability of finding a Cooper pair in an occupied state $|v|^2$ is given by the expression

$$|v|^2 = \frac{1}{2} \left(1 - \frac{E}{\sqrt{E^2 - \Delta^2}} \right). \quad (3.6)$$

Here the quantity Δ (gap parameter) appears, which symbolizes the binding energy of the two electrons in a Cooper pair. To split the Cooper pair into two electrons an energy of at least 2Δ has to be supplied. The single electrons which are excited out of the Cooper pair are referred to as quasi-particles (QP). This also holds for single electrons that are injected into the BCS ground state finding no corresponding partner for building Cooper pairs. Their energy is given by

$$E_{QP} = \pm \sqrt{\epsilon_k^2 + \Delta^2} \quad \text{with} \quad \epsilon_k^2 = \left(\frac{(\hbar k)^2}{2m} - E_F \right). \quad (3.7)$$

We find an energy spectrum that is reminiscent of the band structure model in semiconductor physics, which is often used to explain physical phenomena related to quasi-particles. It is important to keep in mind that the physics is different in the case of superconductors compared to semiconductors.

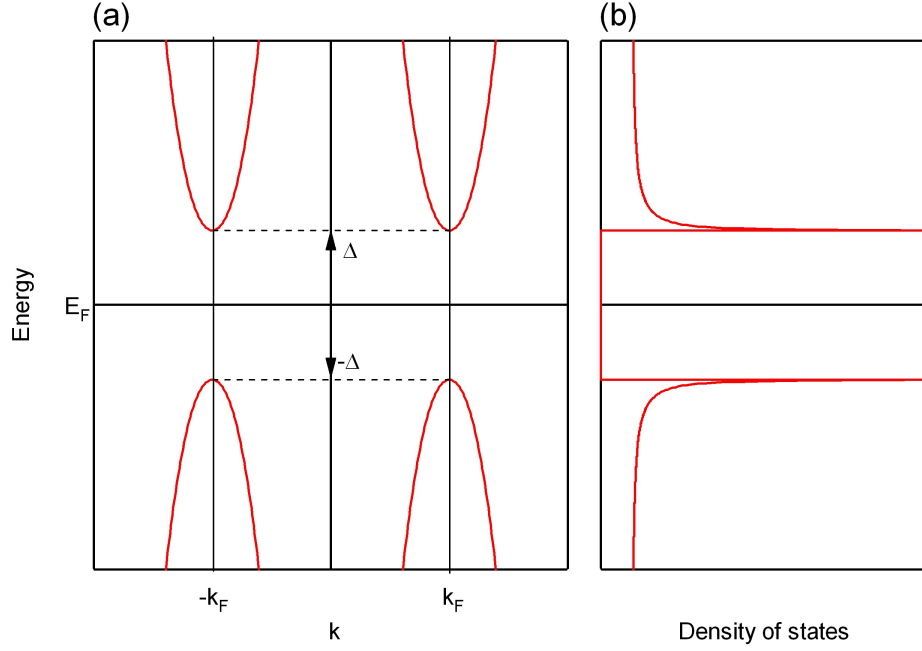


Figure 3.1: Semiconductor model of superconductivity and quasi-particle density of states at $T \approx 0$ K. (a) Energies of the quasi-particles according to Equ. 3.7. (b) The corresponding density of states calculated from Equ. 3.8. The lifetime broadening parameter Γ was set to zero.

In STM, a convolution between the densities of states of tip and sample is measured. Therefore, one needs an expression for the quasi-particle density of states ρ_{QP} rather than the energy spectrum. This was given by BCS and later extended by Dynes [2, 42]

$$\rho_{QP}(E, \Gamma) = \left| \text{Re} \left(\frac{E - i\Gamma}{\sqrt{(E - i\Gamma)^2 - \Delta^2}} \right) \right|. \quad (3.8)$$

The Γ parameter was added by Dynes *et al.* to include broadening processes due to a limited lifetime of the quasi-particles in the states at $\pm\Delta$.

The complete calculation for the derivative of the current with respect to the voltage is given by Equ. 2.11. For modeling the tunneling conductance between a superconducting tip and a normal conducting sample we apply Equ. 2.11 with the indices for tip and sample exchanged. This means we have a constant DOS at the sample and a superconducting DOS at the tip. Further assuming that the whole temperature dependence is covered by the Fermi function of the sample, we find the following equation for modeling the density of states in a tunneling experiment between a superconducting tip and a normal conducting sample

$$\frac{dI}{dV} \sim \int_{-\infty}^{\infty} \rho_t(E) f'_s(E - eV) dE \quad (3.9)$$

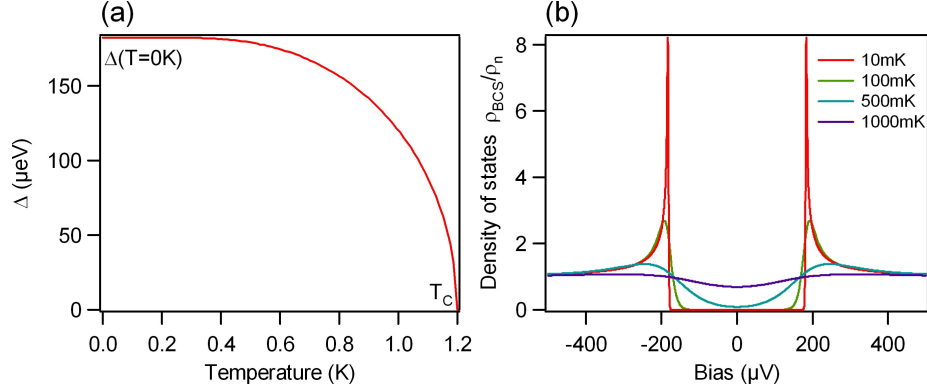


Figure 3.2: Temperature dependence of Δ and the quasi-particle density of states for aluminum. (a) Variation of Δ with the temperature according to the BCS theory. It is calculated by solving Eqs. 3.11 and 3.12 self consistently. The Debye temperature for Al which is used to calculate $\hbar\omega_D$ is $T_D = 433$ K. (b) Quasi-particle excitation gaps calculated for different temperatures for Al. $T_C = 1.2$ K, $\Delta(T = 0) = 182 \mu\text{eV}$.

where $\rho_t(E)$ is the density of states of the tip and $f'_s(E - eV)$ the energy derivative of the Fermi function (see Equ. 2.13). For $\rho_t(E)$ we have to insert the quasi-particle excitation spectrum from Equ. 3.8.

If the critical temperature T_C of a BCS superconductor is known, the energy position of the quasi-particle excitation peaks can be calculated to [37]

$$\Delta(T = 0) = 1.764k_B T_C. \quad (3.10)$$

This position of the quasi-particle states Δ depends on the temperature and is determined by the following equation which has to be solved for pairs of T and Δ [37]

$$\frac{1}{\lambda} = \int_0^{\hbar\omega_D} \frac{\tanh \frac{1}{2k_B T} \sqrt{\epsilon^2 + \Delta^2}}{\sqrt{\epsilon^2 + \Delta^2}} d\epsilon \quad (3.11)$$

where $1/\lambda$ is the dimensionless electron-phonon coupling parameter. By using the Debye energy $\hbar\omega_D$ it is calculated according to [37]

$$\frac{1}{\lambda} = \int_0^{\hbar\omega_D/(2k_B T)} \frac{\tanh x}{x} dx. \quad (3.12)$$

The corresponding energy $\hbar\omega_D$ can also be calculated through the Debye temperature $k_B T_D$. A simulation of the temperature dependence of Δ and the corresponding quasi-particle densities of states for aluminum is shown in Fig. 3.2.

3.2 Andreev reflections

Tunneling involving a superconductor can lead to novel reflection processes. It does not matter if the other electrode is a metal or a superconductor. This processes where first

described by A.F. Andreev in 1964 [43]. Blonder, Tinkham and Klappwijk developed a theory for describing the current voltage characteristic of microbridges and point contacts between two superconductors [44, 45] on the basis of Andreev reflections.

These processes require the condition i) $\Delta < |eV| < 2\Delta$ for tunneling between two equal superconductors (SIS) or (ii) $0 < |eV|$ in the case of superconductor–normal tunneling (SIN) for the applied bias voltage between both electrodes to be fulfilled. This process is depicted for the case of SIS tunneling in Fig. 3.3. In Fig. 3.3 (a) an incoming electron from the occupied states of the left superconductor approaches the tunneling barrier (1). As it does not find any empty states in the second superconductor to go to, it forms a Cooper pair while creating a hole (2). The energy of the hole is the mirrored energy of the original electron at the Fermi energy of superconductor two and its spin is reversed. The hole tunnels back into superconductor one where plenty available empty hole states are, leaving the tunnel junction in the opposite direction. Thus the (\vec{k}, \uparrow) electron is transferred into a $(-\vec{k}, \downarrow)$ hole transporting two charges across the junction. These processes can also occur at higher orders as shown in Fig. 3.3 (b). Two electrons and one hole are involved, resulting in three unit charges that are transported across the junction.

Concerning the transport properties, every new order gives an additional unit charge, resulting in steps of the current at the applied bias voltage where the Andreev reflection sets in. In the case of equal superconductors the voltage positions are given by $2\Delta/(ne)$, $n \in \mathbb{N}$, which results in a subgap structure of the measured conductance curve [44, 46, 47]. It is important to note that the gap sizes of both superconductors do not have to be equal [46]. This results in modified positions for the current steps $\pm\Delta_1/(ne)$, $\pm\Delta_2/(ne)$ and $\pm(\Delta_1 + \Delta_2)/((2n + 1)e)$ where e is the electron charge and $n \in \mathbb{N}$ an integer. Another phenomenon coming along with Andreev reflections is the excess current. The high voltage limit of the current does not extrapolate back to zero for $V=0$ V. The 0 V intercept at the current axes is referred to as excess current.

In the case of tunneling between a normal and a superconductor, the subgap structure is absent but the excess current is still observed. The current steps that indicate the energy positions of the quasi-particles smears out, with increased probability for Andreev reflections [45].

Andreev reflections can be described in terms of an energy dependent reflection coefficient $A(E)$. The wavefunction of the incoming electron to a tunneling junction involving a superconductor in one dimension is

$$\psi_{\text{inc}} = \begin{pmatrix} 1 \\ 0 \end{pmatrix} \exp(ikx) \quad (3.13)$$

The reflected hole wavefunction is

$$\psi_{\text{ref}} = a \begin{pmatrix} 0 \\ 1 \end{pmatrix} \exp(-ikx) \quad (3.14)$$

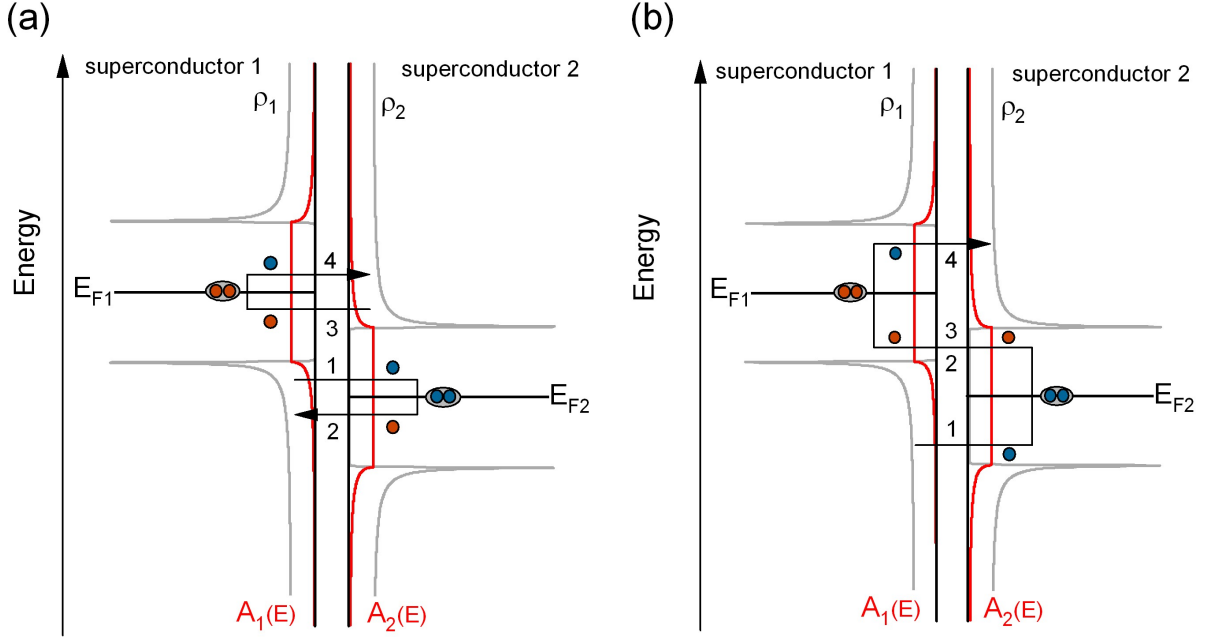


Figure 3.3: Andreev reflection processes between two superconductors. The grey lines indicate the quasi-particle density of states where the red lines are the probability for an electron to be Andreev reflected. (a) Second order processes. (b) Third order processes. The sketch is reproduced from [47].

The reflection coefficient $A(E) \equiv aa^*$ is

$$A(E) = \begin{cases} 1, & |E| < \Delta; \\ \frac{|E| - \sqrt{E^2 - \Delta^2}}{|E| + \sqrt{E^2 - \Delta^2}}, & |E| \geq \Delta. \end{cases} \quad (3.15)$$

The calculated reflection coefficient is shown in Fig. 3.3 as red curve. For a single superconductor the probability of a particle to be Andreev reflected inside the gap region is one. Outside the gap this value decreases fast, until it reaches zero.

3.3 Josephson effect

In a tunneling experiment between two superconductors, a finite current even at zero bias is measured resulting in a pronounced peak in the conductance curve. This effect was first described by Brian D. Josephson in 1965 [48]. The magnitude of this peak changes with the coupling between the superconductors.

The reason for this current is a coherent tunneling of Cooper pairs from one electrode to the other. We can assign wave functions to the superconducting condensates in the

electrodes $\Psi_{1,2} \exp i\phi_{1,2}$ containing the phases $\phi_{1,2}$. Using the phase difference $\Delta\phi = \phi_1 - \phi_2$ one can express the current at zero bias voltage [37]

$$I_J = I_C \sin \Delta\phi \quad (3.16)$$

where I_C is the critical current. Depending on the coupling, which can be related to the normal state tunneling resistance $R_N = V_{\text{Bias}}/I_N$, one can find an expression for I_C . When tunneling between two superconductors with different gap-parameters Δ_1 and Δ_2 one gets [49, 50]

$$I_C = \Delta_2(T) K \frac{1}{R_N} \tanh \left(\frac{\Delta_2(T)}{2k_B T} \right) \quad (3.17)$$

where Δ_2 is the smaller gap of the two and $K = K(\sqrt{1 - \Delta_2(T)^2/\Delta_1(T)^2})$ Jacobis complete elliptical integral of first kind.

Further, if a voltage is applied across the junction the phase difference $\Delta\phi$ will change with time

$$\frac{d(\Delta\phi)}{dt} = \frac{2eV_J}{\hbar} \quad (3.18)$$

where e is the elementary charge, V_J the voltage across the junction and \hbar Plancks constant. In standard text books Equ. 3.16 is often referred as dc Josephson effect and Equ. 3.18 as the ac Josephson effect.

The critical current in Equ. 3.16 can also be seen as an estimate how strong the two superconductors are coupled. The corresponding energy, which is referred to as Josephson binding energy is given by [37]

$$E_J \equiv (\hbar I_C / 2e). \quad (3.19)$$

When analyzing the Josephson current, often the binding energy E_J is compared to the thermal energy $k_B T$. The effective temperature for the electrons in our system is about 100 mK which corresponds to a thermal energy of $8.6 \mu\text{eV}$.

To estimate the Josephson current, it is important to consider the whole experimental environment. This means the voltage drop across the cables of the experimental setup has to be taken into account as well as their capacitances. This leads to a scheme which is depicted in Fig. 3.4. Following Joyez *et al.* one can derive an equation for the current, depending on the ratio of the Josephson binding energy and the temperature of the electrons [51].

$$I(\chi) = I_C \langle \sin \delta\phi \rangle = I_C \text{Re} \left[\frac{\mathfrak{S}_{1-i\eta} \left(\frac{E_J}{k_B T_{\text{eff}}} \right)}{\mathfrak{S}_{-i\eta} \left(\frac{E_J}{k_B T_{\text{eff}}} \right)} \right] \quad (3.20)$$

with

$$\eta = \frac{E_J}{k_B T_{\text{eff}}} \chi. \quad (3.21)$$

\mathfrak{S}_n are the modified Bessel functions of the first kind and complex order n . Eqs. 3.20 and 3.21 are depicted for different values of $E_J/(k_B T_{\text{eff}})$ in Fig. 3.5. The larger the ratio $E_J/(k_B T_{\text{eff}})$ is, the less effects have thermal fluctuations on the junction. This results in a

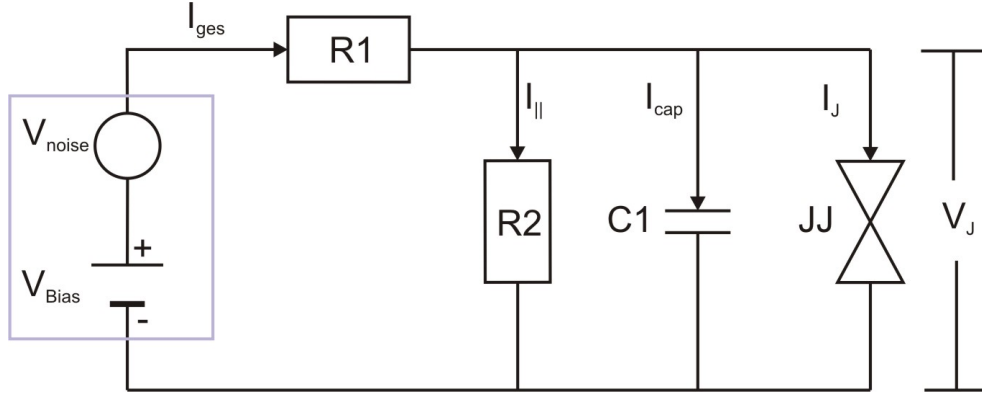


Figure 3.4: The Josephson junction integrated into the experimental setup. The Josephson junction (JJ) is symbolized by \bowtie . In a voltage biased circuit the resistances and capacitances of the cables have to be taken into account. From this schematic a differential equation for the current can be derived allowing the calculation of I_J [51].

steeper onset for I . The fact, that the curves have an onset before the current reaches the maximum I_{\max} , is an effect of the finite temperature of the junction.

For normal state tunneling resistances R_N which are of the order of the total cable resistance of the setup (including filters, I-V converter) we have to compensate the voltage drop across the cables. For the compensation the following equation is used

$$V_J = V_B - R_1 I_T(V_B). \quad (3.22)$$

For our system the total resistance R_1 from the output of the bias source including high frequency filter, voltage divider, I-V converter and wiring of the cryostat is $(1.3 \pm 0.1) k\Omega$. Therefore a compensation of the I-V curve is not necessary because the normal state tunneling resistances (R_N) presented in this thesis are much higher than R_1 .

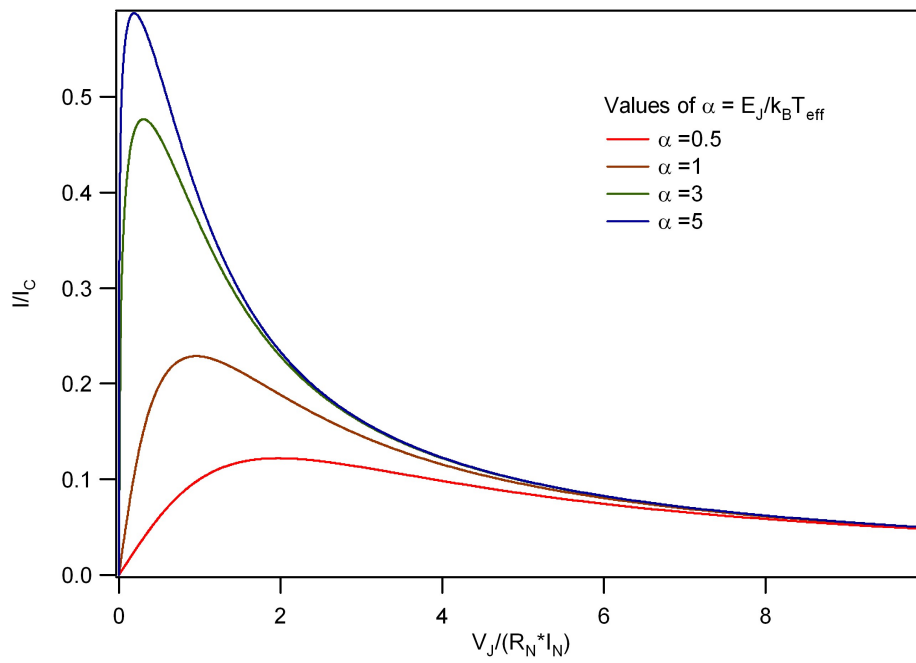


Figure 3.5: Calculated Josephson current for different ratios of $E_J/(k_B T_{\text{eff}})$. For the calculation Eqs. 3.20 and 3.21 were used.

Chapter 4

Refrigeration below 100mK: Dilution Refrigeration

To cool matter below 100 mK, four refrigeration methods are available: Demagnetization of electron [52–54] or nuclear spins [55–57], Pomeranchuk cooling by solidification of ^3He [54, 58, 59] and dilution refrigeration by spontaneous separation of ^3He and ^4He [52, 54, 60]. The first methods are only used as single shot methods, while a dilution refrigerator (DR) can operate continuously.

In contrast to single shot methods, a continuous refrigerator can supply cooling power to an experiment without any time limit. This is a enormous advantage if one considers a constant heat flowing to an experiment through wires, thermal radiation and heat release from moving piezos.

Dilution refrigeration is generated on a proposal by H. London in 1951 [61] which was published by H. London, G.R Clarke, and E. Mendoza eleven years later [62]. Instead of using the latent heat of evaporation of liquid Helium as refrigeration principle (which was the common method in these days to reach temperatures below 1K) they suggested to use the latent heat of mixing of the two He isotopes ^3He and ^4He . A first refrigerator based on this proposal was realized by Das, De Bruyn Ouboter and Taconis [63]. However, the first refrigerator that was able to cool below 100 mK was reported by Hall, Ford and Thompson [64]. With moderate experimental efforts dilution refrigerators can continuously reach temperatures of 30 mK while more advanced setups can cool even below 10 mK. The lowest temperature achieved by dilution refrigeration is 1.9 mK which was reported by Frossatti and coworkers first in Grenoble and later in Leiden [65, 66].

This chapter is dedicated to the cryogenic part of the thesis. Most of the theory presented here is taken from the books of Lounasmaa [52] and Pobell [54], which are excellent reviews on the field of low temperature physics and instrumentation. I will start with a description of the properties of pure ^3He and ^4He (Sec. 4.1) and extend it to mixtures of these two isotopes (Sec. 4.2). These basics are used in Sec. 4.3 to explain the working principle of a dilution refrigerator. The highly specialized dilution refrigerator which we use for our STM experiment is described in Sec. 4.4. An important task is the measurement of temperatures, which is not straight forward below 100 mK. The thermometry is explained

in Sec. 4.5 including the calibration procedure of the thermometers used in our system. The performance of the refrigerator is shown in Sec. 4.6.

4.1 Physical properties of ^3He and ^4He

Helium at very low temperatures does not behave like a classical gas anymore [67]. The two He isotopes (^3He and ^4He) differ only in the number of nuclei and therefore have different nuclear spin. The nucleus of ^4He consists of two protons and two neutrons resulting in a total spin of $I_{^4\text{He}} = 0$ which implies that ^4He follows Bose statistics. ^4He starts to form a Bose-Einstein condensate at a transition temperature of 2.17 K (superfluid transition) and is in the quantum mechanical ground state below 0.5 K where the condensate contains all the ^4He atoms. Nearly no phonons and rotons are excited anymore and the viscosity, entropy and specific heat vanishes. On the other hand the nucleus of ^3He contains two protons and one neutron. The nuclear spin is $I_{^3\text{He}} = 1/2$ and it has to obey Fermi statistics as well as the Pauli exclusion principle. This means only two atoms with different spins are allowed to occupy one energy state. The atoms will fill the energy states that are available up to the Fermi energy like electrons in a metal. The difference between the two is striking if one compares their Fermi temperatures. The Fermi temperature of electrons in a metal is of the order 10^4 K compared to ^3He with 1 K. This means that the influence of Fermi statistics in ^3He shows up only at very low temperatures ($T \ll 0.1$ K). Like electrons, ^3He also undergoes a transition to a Bose ground state which occurs at a temperature of 2.7 mK. Similar to metals, Bose condensation is achieved through pairing of ^3He atoms into quasi particles, which can condensate in a single ground state.

4.2 Mixtures containing of ^3He and ^4He

For understanding the working principle of a dilution refrigerator, it is necessary to know about the basic behavior of the refrigerant, which is the $^3\text{He}/^4\text{He}$ mixture [68–71]. During the cooling process, two phases with different ^3He concentration will form. Therefore it is convenient to define the concentrations of the different He isotopes in these phases as follows

$$x = x_3 = \frac{n_3}{n_3 + n_4} \quad \text{and} \quad x_4 = \frac{n_4}{n_3 + n_4} \quad (4.1)$$

where $x = x_3$ is the concentration of ^3He in the mixture, x_4 the concentration of ^4He , n_3 is the number of ^3He atoms and n_4 the number of ^4He atom in percent or moles.

Phase diagram of $^3\text{He}/^4\text{He}$ mixtures

The behavior of a $^3\text{He}/^4\text{He}$ mixture as a function of ^3He content is described by the phase diagram in Fig. 4.1 [13, 52, 54]. Pure liquid ^4He turns superfluid at a temperature of 2.17 K. This is the starting point of the lambda line which separates the normal liquid

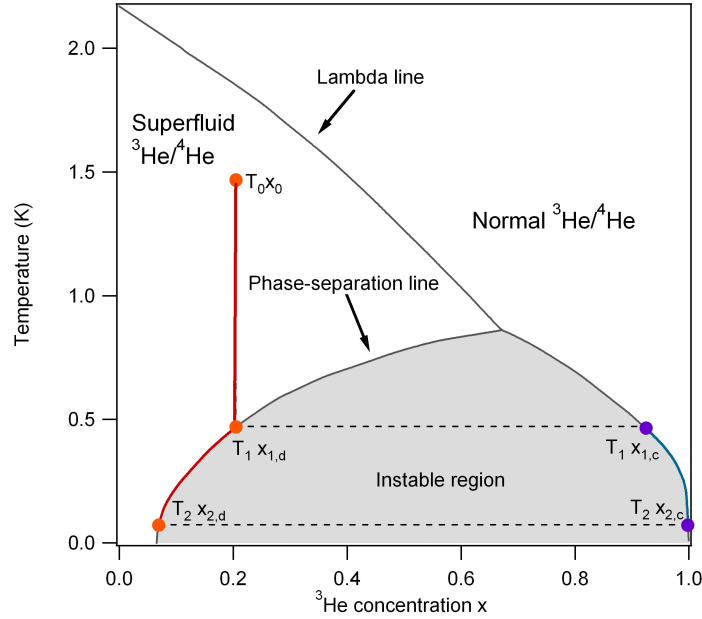


Figure 4.1: Phase diagram of a liquid $^3\text{He}/^4\text{He}$ mixture. The graph is reproduced from [13] and an example for cooling down a mixture containing 20% ^3He is added.

phase from the suprafluid phase. Pure ^3He on the other hand undergoes the suprafluid transition at 2.7 mK. Adding ^3He step by step to the ^4He will result in a decrease of the superfluid transition temperature which is described by the shape of the lambda line. At a temperature of 0.867 K and a ^3He concentration of 67.5% the lambda line meets the phase separation line. Here the superfluidity of ^4He vanishes and further cooling results in a formation of two fluid phases with different concentration of ^3He (not to be mixed up with the superfluid phase): one phase which is rich in ^4He (diluted phase) and one which is rich in ^3He (concentrated phase). Below the phase separation line is a region of the phase diagram which is not accessible for any mixture state. The concentrated phase has a lower density and floats on top of the diluted phase. Following the phase separation line to a temperature of 0 K one notices that the concentrated phase contains only ^3He but the diluted phase is not pure ^4He . It still contains a finite amount of ^3He ($x = 6.6\%$) at saturated vapor pressure. Increasing the pressure above the helium mixture can enhance the limiting concentration in the diluted phase to 9.5% [72]. The finite amount of ^3He in the diluted phase is essential for the dilution refrigerator to work.

As an example one can consider cooling a mixture containing $x \simeq 20\%$ ^3He (Fig. 4.1 bold orange line). Below $T \simeq 1.85$ K it turns superfluid. The mixture is cooled from the initial values of temperature T_0 and concentration x_0 to the phase separation line at $T_1 \simeq 0.45$ K. At this temperature the two phases will form (the concentrated containing $x_{1,c}$ ^3He and the diluted containing $x_{1,d}$ ^3He). During further cooling to the final temperature T_2 the components of the mixture follow the branches of the phase separation line. This

results in the final ^3He concentration for the diluted phase $x_{2,d}$ and the concentrated phase $x_{2,c} = 100\%$.

Finite Solubility of ^3He in ^4He

An important fact for the realization of dilution refrigeration is the finite solubility of ^3He ($x_d = 6.6\%$) in the diluted phase at zero temperature [52, 54, 68]. The reason for this behavior becomes clear, if one compares the chemical potential of a single ^3He atom in the concentrated and the diluted phase and asks how the binding energy changes at $T = 0\text{ K}$. In the concentrated phase a ^3He atom is surrounded by other ^3He atoms. The chemical potential $\mu_{3,c}(0)$ at zero temperature and the binding energy are related to the latent heat of evaporation L_3 of ^3He under saturated vapor pressure

$$\mu_{3,c}(0) = -L_3. \quad (4.2)$$

In the diluted phase the ^3He atoms are surrounded by ^4He and the energy for removing a ^3He atom from a ^4He host is given by

$$-\epsilon_{3,d} = \frac{\mu_{3,d}(0)}{N_0} \quad (4.3)$$

where $\mu_{3,d}(0)$ is the chemical potential of ^3He in the diluted phase, N_0 is the Avogadro number and $\epsilon_{3,d}(0)$ the binding energy of the ^3He atom (the derivative is given for the limit of $T = 0\text{ K}$).

Both He isotopes have the same electronic configuration and therefore the same van der Waals interaction. Anyhow, due to the larger atomic mass of ^4He the zero point motion is smaller than for ^3He . A single ^3He atom is therefore more strongly bound in a ^4He than in ^3He host

$$\mu_{3,d}(0) < \mu_{3,c}(0) \quad (4.4)$$

$$-\epsilon_{3,d}(0) < -L_3/N_0. \quad (4.5)$$

When successively adding further ^3He atoms to the ^4He phase, two effects are acting against each other. The first one lowers the absolute binding energy of ^3He in ^4He and can be explained by a modified Fermi liquid theory [73]. Dilute ^3He in ^4He is still a Fermi system with an effective mass $m^*(x)$ and a Fermi energy $k_B T_F(x)$, both depending on the concentration x of ^3He (k_B is Boltzmanns constant and T_F the Fermi temperature). A modified Fermi liquid theory implies that available energy states can only be occupied by two ^3He atoms with different nuclear spins, up to the Fermi energy of the system $k_B T_F(x) = (\hbar^2/2m^*)(3\pi^2 x N_0/V_m)^{2/3} \sim x^{2/3}$. The second effect is attractive between two ^3He atoms and increases the absolute binding energy $\epsilon_{3,d}(x)$. Two ^3He atoms feel an attractive interaction due to the nuclear magnetic moments and their zero point motion. The larger zero point motion of ^3He compared to ^4He atoms results in a ^4He depleted volume around a ^3He atom. This low density region is felt by a second ^3He atom. The

chemical potential of a ^3He atom in a dilute solution with a ^3He concentration x is a contribution of both effects

$$\frac{\mu_{3,d}(x)}{N_0} = -\epsilon_{3,d}(x) + k_B T_F(x). \quad (4.6)$$

The change in the chemical potential of diluted ^3He is depicted in Fig. 4.2. The blue curve shows the chemical potential including attractive and repulsive effects where the red curve depicts only the contribution of attractive effects (Equ. 4.6). A steady increase of the ^3He concentration decreases the ^3He binding energy. The repulsive interaction out of the Fermi liquid behavior dominates above the attractive interaction in the diluted phase. At a concentration of $x = 6.6\%$ the binding energy of the ^3He in the diluted phase equals the binding energy of ^3He in the concentrated phase [60].

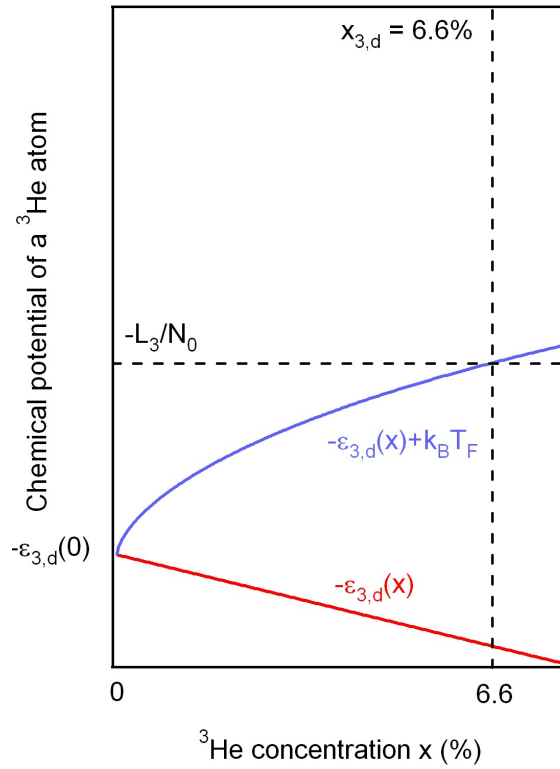


Figure 4.2: Chemical Potential of a ^3He atom in the diluted phase. The value $-L_3/N_0 = 2.473[\text{K}] \cdot k_B$ corresponds to the chemical potential of ^3He in the concentrated phase [54]. The chemical potentials of ^3He in both phases are equal at a ^3He concentration of $x_{3,d} = 6.6\%$.

4.3 Working principle and main components of a dilution refrigerator

Very nice reviews summarizing the construction aspects of dilution refrigeration can be found in the books of Lounasmaa and Pobell and in the review of Weathley [52, 54, 60, 74]. The basic working principle of refrigeration by dilution of ^3He is depicted in Fig. 4.3 [54]. In a gedanken experiment it can be compared to refrigeration through evaporation (for example pure ^3He) Fig. 4.3 (a), but one has to keep in mind that the physical background of both processes is different. In evaporative cooling one relies on the heat of evaporation. Particles from the liquid phase are passing the phase boundary into the gas phase lowering the internal energy of the liquid. They are removed from the phase boundary by means of an external pumping system and are feed back into the cryostat through a pre-cooling stage.

Cooling in the dilution process is realized in the mixing chamber (MC) by passing ^3He atoms from the concentrated phase into the diluted phase through the phase boundary. We have a different enthalpy of mixing of two quantum liquids in this situation [54]. The concentrated phase of ^3He floats on top of the diluted $^3\text{He}/^4\text{He}$ phase, which is depicted in 4.3 (b). Using the analogue of evaporative cooling, the concentrated phase can be associated to the liquid and the diluted phase to the gas phase.

A principle schematic of a DR is shown in Fig. 4.4 [52]. The dilution cycle which contains $^3\text{He}/^4\text{He}$ mixture is a closed cycle. The cooling process of the mixture is depicted in the enthalpy-pressure diagram in Fig. 4.5. The warm ^3He enters the refrigerator at room temperature. It has a pressure of 50 – 400 mbar and is precooled to $T=4.2\text{ K}$ in the main Helium reservoir, corresponding to point (A) in Fig. 4.5 [13, 75]. In a next step it is further cooled and fully liquified ($T=1.5\text{ K}$) in the 1K-Pot heat exchanger (or condenser) (Fig. 4.5 (B)) [76, 77].

The 1K-Pot is a little chamber which is connected to the main ^4He reservoir through a flow impedance. The pot is evacuated by a rotary pump and liquid He is sucked from the main ^4He bath into the pot. The pressure above the He inside the pot is about 2 mbar compared to the main He bath which is at saturated vapor pressure and therefor the pot is cooled to roughly 1 K.

After precooling the incoming ^3He in the 1K-pot a flow restriction, the main impedance, allows the ^3He to expand adiabatically to pressures around 20 mbar (Fig. 4.5 (C)). Due to the positive slope of the enthalpy curve in this region, the liquid ^3He slightly warms up again. Further cooling to temperatures of $T=1\text{ K} - 0.5\text{ K}$ is accomplished at the still heat exchanger. In combination with a second flow restriction (secondary impedance) this avoids bubbling and partial evaporation before the ^3He enters the main heat exchanger section of the DR.

On the way to the mixing chamber the incoming ^3He needs to be thermalized very carefully. As the enthalpy for the outgoing diluted phase is higher than for the incoming ^3He , it is used to precool the ^3He in several heat exchangers. First, ^3He passes a continuous heat exchanger right after the second impedance followed by several step heat exchangers.

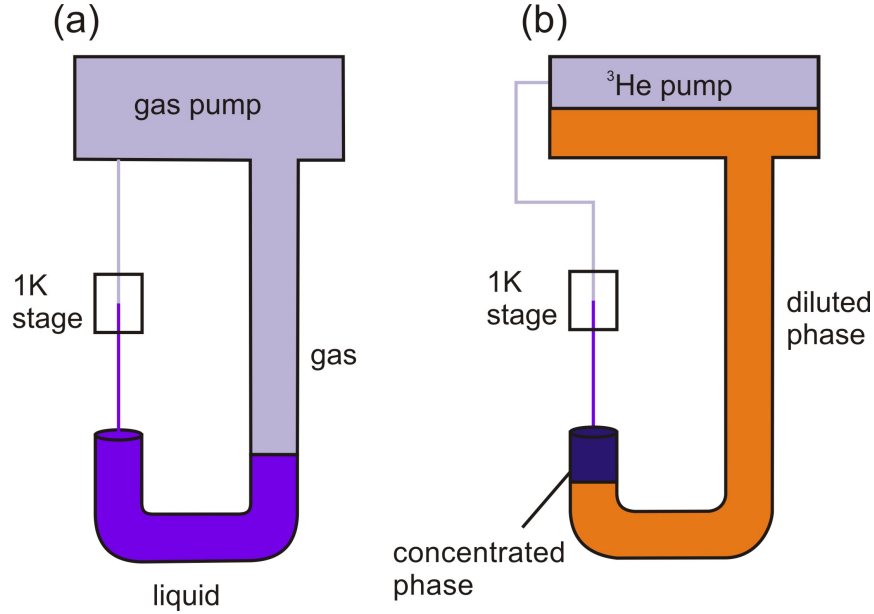


Figure 4.3: U-tube model of a dilution refrigerator. This gedanken experiment and model explains the basic idea of a DR [54]. See text for details.

For the performance of the DR it is necessary that the ^3He enters the MC at a temperature which is as close as possible to the desired base temperature. In other words, the lower the temperature is at which the ^3He leaves the last heat exchanger the lower will be the base temperature in the mixing chamber.

The MC is the coldest part in the cryostat. In a well operating system the boundary between concentrated and diluted phase is in the middle of the MC. Inside the mixing chamber the ^3He crosses the phase boundary and enters the diluted phase. The diluted phase fills up all the pipes on the outgoing side of the heat exchangers up to the still chamber. The ^4He in the diluted phase acts as a suprafluid background for ^3He which travels along the liquid column according to a difference in osmotic pressure between MC and Still. The temperature of the Still is adjusted in a way, that it is high enough to evaporate ^3He but still below the evaporation temperature of ^4He .

A little orifice with a cutting edge on the exit of the still chamber avoids that the suprafluid ^4He leaves it [60]. ^4He that leaves the still causes trouble during the recondensation of ^3He at the inlet (return side) side of the refrigerator. Partially phase separation takes place already in the heat exchangers and limits the efficiency of the precooling process.

After leaving the still the ^3He is pumped by a combination of a rotary and a roots pump at room temperature. It flows through a gas handling system (GHS) which is used for the operation of the DR (not shown in Fig. 4.4). A liquid Nitrogen and a liquid Helium cold trap are used to clean the mixture before it is fed to the return side of the dilution cycle again.

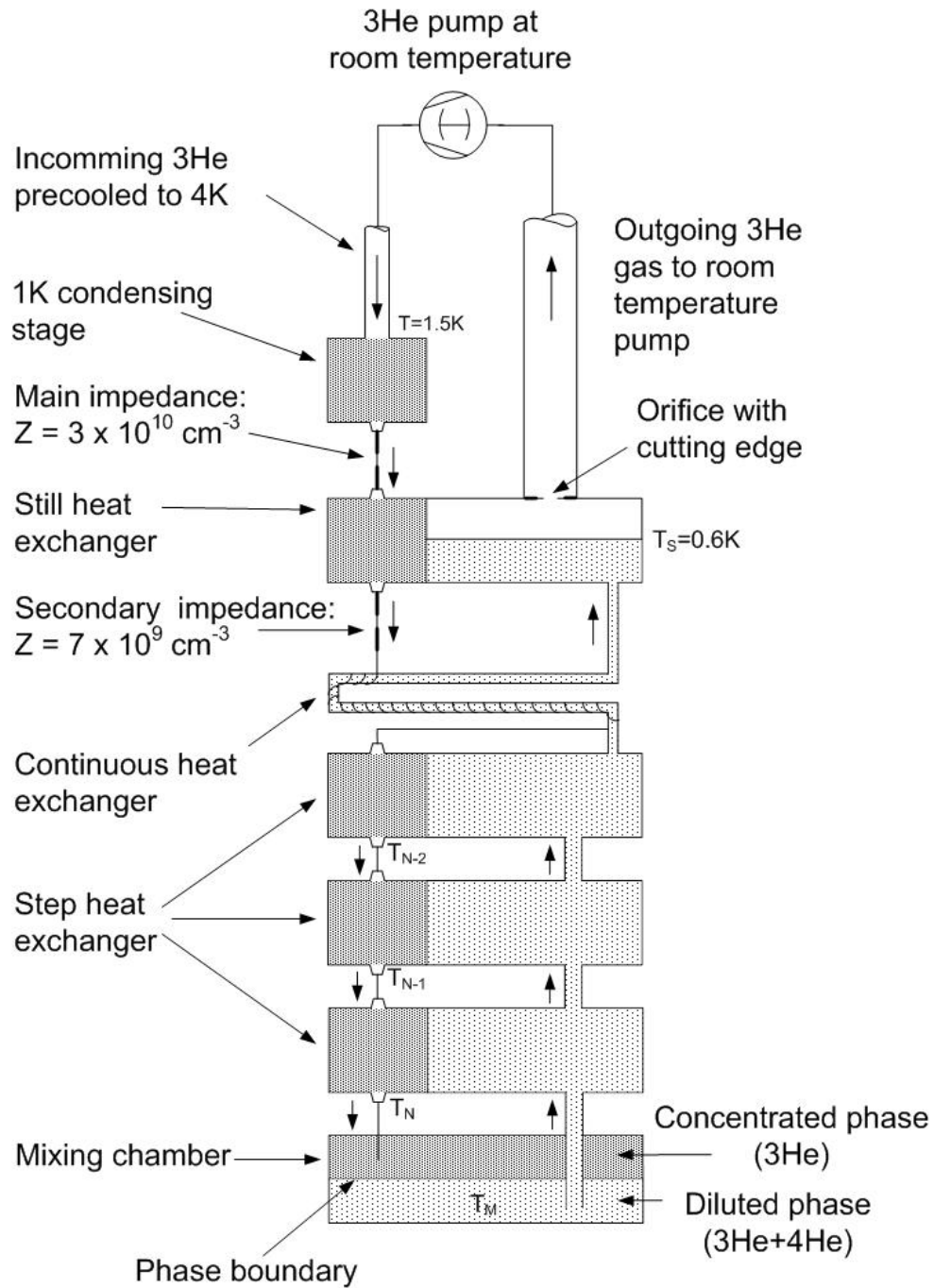


Figure 4.4: Schematic of a dilution refrigerator taken from [52].

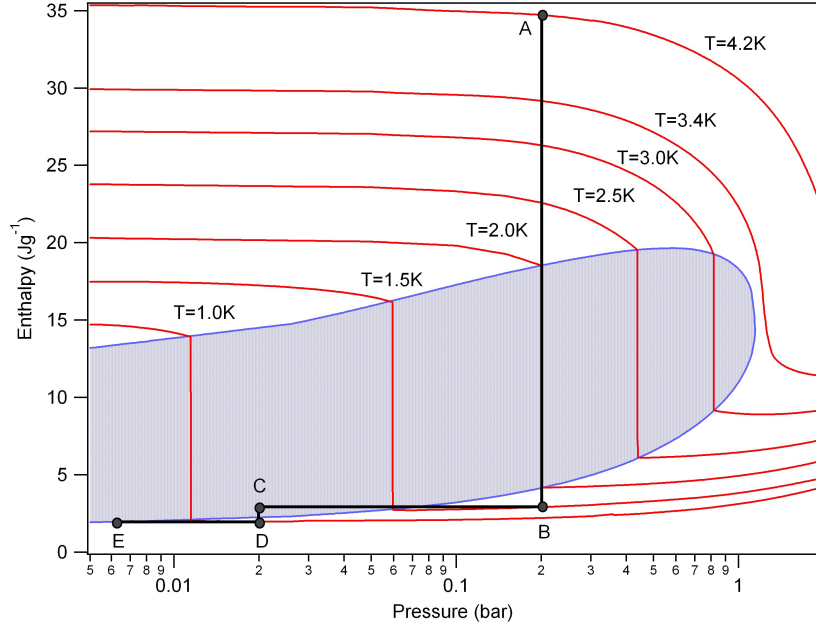


Figure 4.5: Enthalpy-pressure diagram of ^3He . The diagram is reproduced from [13, 75].

Cooling Power of a dilution refrigerator

The cooling power in general is defined as a particle flow between two phases times the difference in enthalpy between them [54]. In the derivation I will follow Pobell and the references therein. In the case of diluting refrigeration the cooling power \dot{Q} is the product between the molar flow rate of ^3He atoms crossing the phase boundary \dot{n} and the enthalpy difference between the concentrated $H_d(T)$ and diluted phase $H_c(T)$

$$\frac{d}{dt}Q = \dot{Q} = \dot{n}(H_d(T) - H_c(T)). \quad (4.7)$$

The condition $H_d(T) > H_c(T)$ is known from measurements of the specific heat $C_d(T)$ and $C_c(T)$ of both phases. The relation between the specific heat $C(T)$ and the enthalpy $H(T)$ is given by

$$H(T) - H(0) = \int_0^T C(T) dT. \quad (4.8)$$

As the diluted and concentrated phase are Fermi liquids, the specific heat in both phases varies linearly with temperature. For temperatures below $T=0.05\text{K}$ the concentrated phase consists only of ^3He . Measurements of the specific heat in the concentrated phase [78, 79] give the following relation at temperatures below $T = 0.04\text{K}$

$$C_c(T) = 22T [\text{J (mole of } ^3\text{He K)}^{-1}]. \quad (4.9)$$

This is a very large value due to the fact that the Fermi temperature (T_F) of ^3He is so small. In metals the specific heat is 10^4 times smaller at these temperatures.

Using Equ. 4.8 and Equ. 4.9 one gets for $H_c(T)$

$$H_c(T) = 11T^2 + H_c(0) \text{ [J (mole of } ^3\text{He)}^{-1}]. \quad (4.10)$$

In the case of the diluted phase we also deal with a Fermi liquid but the superfluid background of ^4He gives corrections to C_d . Most important are the properties of the diluted liquid in the mixing chamber where the ^3He concentration is 6.6 %. Including all approximations the specific heat reads

$$C_{d,6.6\%}(T) = 106T \text{ [J (mole of } ^3\text{He K)}^{-1}]. \quad (4.11)$$

Both phases are in thermic equilibrium, which means that their chemical potentials have to be equal

$$\mu_c(x_c, T) = \mu_d(x_d, T) \quad (4.12)$$

which lead to

$$H_c - TS_c = H_d - TS_d \quad (4.13)$$

by using the relation $\mu = H - TS$ where S is the entropy. Combining Equ. 4.13 with 4.9, 4.10 and 4.11 gives

$$H_d(T) = H_c(0) + 11T^2 + T \int_0^T \left(\frac{C_d(T')}{T'} - \frac{C_c(T')}{T'} \right) dT \quad (4.14)$$

$$= H_c(0) + 95T^2 \text{ [J (mole of } ^3\text{He)}^{-1}] \quad (4.15)$$

This result and Equ. 4.10 can be used to evaluate the cooling power Equ. 4.7

$$\dot{Q} = \dot{n}(H_d(T) - H_c(T)) = 84\dot{n}T^2 \text{ [W]}. \quad (4.16)$$

This equation gives the cooling power of the dilution process inside the mixing chamber. For more realistic cases it is necessary to add an additional term which incorporates external heat leaks \dot{Q}_{ext} . External heating can come from ^3He that enters the MC at higher temperatures as well as heat that is conducted along the wires and the metal parts of a refrigerator. Equ. 4.16 can be rewritten to

$$\dot{Q} = 84\dot{n}T^2 - \dot{Q}_{ext}. \quad (4.17)$$

4.4 Custom designed dilution refrigerator adapted for scanning probe experiments

Scanning tunneling microscopy and spectroscopy demands a lot of prerequisites from the refrigerator to which the microscope is attached. Dilution refrigerators in general are tools that advanced to standard cryogenic equipment in the last decades. Nevertheless combining a standard DR with a scanning tunneling microscope can lead to undesired results in terms of sample cleanliness, vibration stability, thermalization periods and stray magnetic fields

that disturb the measurements. The refrigerator that we developed in collaboration with JANIS research inc. is a highly specialized system adapted for the needs of STM [8]. It was manufactured by JANIS research inc. The refrigerator is compatible to ultra high vacuum especially to pressures below 1×10^{-10} mbar inside the experimental space of the refrigerator. It includes a magnet system which allows measurements in high magnetic fields of 14 T perpendicular and 0.5 T parallel to the sample surface. This implies new construction and fabrication techniques and limits the choice of materials to be used.

In addition a high mechanical stability is necessary to avoid mechanical vibrations at the STM. A main source of acoustical and mechanical noise is the dilution cycle especially the bubbling of partially liquified gases therein. The main contribution comes from the condenser unit (1K-pot) for two reasons: (i) Incoming mixture is only partially liquified and tends to boil and (ii) bubbling of liquid ^4He which experiences a temperature gradient in the siphon between the main ^4He reservoir and the 1K-pot. This causes a sudden phase transition of the ^4He when it enters the pot and can excite vibrations [80–82]. These vibrations are transmitted through the heat exchanger section to the STM.

The mK-STM system enables tip and sample transfer. To realize the transfer one has to implement an access to the microscope through the various cryoliquid reservoirs and radiation shields.

Bottom loading dilution refrigerator for STM applications

The cryostat is depicted in Fig. 4.6 and consists of a dewar section and the dilution insert. The dewar to which the dilution insert is mounted contains a liquid nitrogen (LN) reservoir ($\approx 70\text{l}$) as outer shell and a liquid Helium (LHe) reservoir ($\approx 160\text{l}$) acting as an inner shell. The superconducting magnet is immersed into the LHe bath. Both reservoirs are encapsulated by an UHV chamber which extends through the bottom of the magnet into the DR stage up to the inner vacuum flange (IVC flange) of the DR insert. A 77 K and a 4.2 K radiation shield attach to the respective reservoirs. They shield the inner parts from thermal radiation. The IVC flange of the insert is connected directly to the magnet through a conflat (CF) flange. This flange includes the feedthroughs for wires which are used in the UHV space, feedthroughs for the ^3He return line, the still pumping line and spare ports. The UHV part of the insert consists of the DR stage, which reaches from the condenser unit to the mixing chamber. Two additional radiation shields are used inside the UHV space of the cryostat to shield the parts that are at temperatures below 100 mK. The first shield attaches to the still support plate ($T \approx 0.5\text{ K}$) and extends into the magnet bore. It blocks thermal radiation to the MC and the STM. The second inner shield is attached to an intermediate cold plate (ICP) and covers the MC. It has a base temperature of $T \approx 60\text{ mK}$. The still pumping line leaves the vacuum space through the IVC flange into the main He reservoir. The diameter of the still pumping line is increased twice and has a final value of 100 mm when it leaves the cryostat. It is connected to a roots blower pumping station which includes a roots blower and a mechanical pump, that are hermetically sealed. The outlet of the rotary pump is connected to a room temperature

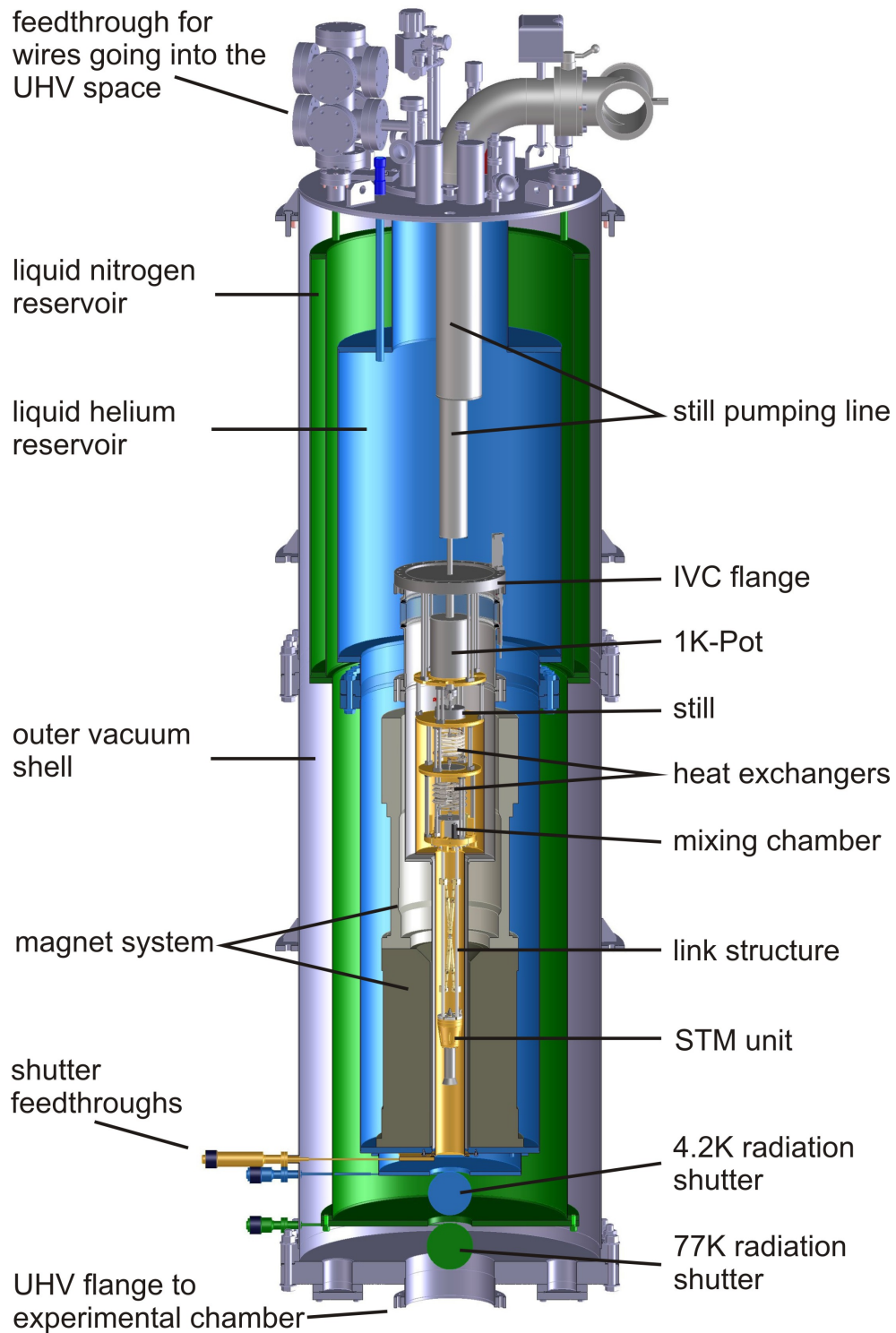


Figure 4.6: Overview of the complete dilution refrigerator.

gas handling system which includes the storage vessels for the mixture (dumps). A LN trap is used to remove residual air from the mixture. Directly in front of the ^3He return inlet of the cryostat we have installed a second cold trap which is mounted into the 1K-pot pumping line. It is cooled to about 10 K by the vapor coming from the 1K-pot and removes residual hydrogen from the mixture (hydrogen solidifies at 20 K) [83].

Ultra high vacuum (UHV) and magnetic field compatibility

The general guideline for designing an UHV compatible system is the use of low outgassing materials. Metal parts like support platforms and heat sinks for wires are mainly fabricated from gold plated copper. Normally an adhesive Ni layer is used underneath the gold plating to prevent the gold to diffuse into the Cu. This was avoided in our setup. The chambers for the dilution cycle, heat exchangers and mechanical supports between different platforms consist out of stainless steel. Electrically insulating parts are made of Polytetrafluorethylen¹ (PTFE) or Polyimide (Kapton) which are low outgassing, high performance polymers that are chemically inert and can stand temperature up to 300 °C without melting.

In addition, it is possible to bake out the cryostat to temperatures of 80 °C. This implies that all containers for the dilution cycle are welded or silver brazed. No indium seals are used because heating causes the indium to flow.

Also new strategies for precooling the DR stage needed to be adapted² to maintain the UHV environment. Precooling has to be done only when the cryostat is cooled down from room temperature. The standard procedure to precool a dilution stage is to use a small amount of exchange gas to achieve a thermalization of the DR stage inside the inner vacuum with the surrounding main He reservoir. But even if the exchange gas is pumped out after the thermalization, a residual gas film remains on the dilution stage and the STM. Concerning STM applications this He film can cause arc discharges between the high voltage electrodes of the piezo motors used in the microscope as well as degrading of the sample surface.

The special precooling loop which is used in our system is a hermetically sealed volume. It consists of a copper heat exchanger coil inside the main liquid He reservoir and passes through the IVC flange into the vacuum space. Little thermalization chambers are attached to the different temperature levels (1K-pot, still, 60 mK level, MC) of the dilution stage. Exchange gas is filled into this chambers which is cooled by the heat exchanger in the He tank. It thermalizes step by step the different temperature levels of the dilution stage to roughly 10 K.

¹Polytetrafluorethylen is commonly known as Teflon. It was discovered in 1938 by the chemist Roy Plankett, but for a long time no application was found for Teflon. This changed when scientists from the Manhattan project were looking for an inert storage vessel for highly reactive Uranhexafluoride.

²The dilution insert is thermically well isolated from the LN and LHe bath. Therefore it has to be precooled to roughly 10 K before the dilution cycle can be started.

Demand for low acoustical noise and vibrations

As mentioned in the introduction, keeping the mechanical and acoustical noise level in a dilution cryostat small is a challenging task. This section deals with disturbances from inside the cryostat due to boiling of cryogenics. We have to consider the following sources of mechanical noise

- LN reservoir
- LHe reservoir
- 1K-pot

To deal with the liquid nitrogen reservoir is rather straight forward. Pumping on the nitrogen reservoir reduces the vapor pressure and temperature of the liquid until it reaches the triple point at $p_{\text{triple}} = 125\text{ mbar}$. Here it starts to solidify until all nitrogen is frozen out, and does not cause bubbling and boiling anymore.

For the liquid helium in the main reservoir one does not need to apply special treatment. During evaporation the reservoir is under ambient pressure and does not produce significant disturbances.

The vibrational noise from the 1K-pot is more challenging. Several publications in the literature can be found dealing with this problem [80–82]. In our system ^4He is sucked through a needle valve into the pot by an external rotary pump. The reduced pressure above the liquid ^4He inside the pot causes it to cool from 4.2 K to 1.5 K. The He column in the siphon which connects the main ^4He reservoir and the 1K-pot experiences a temperature gradient from $T=4.2\text{ K}$ to temperatures near 1 K. As liquid ^4He turns superfluid at 2.17 K, the He inside the 1K-pot is in the superfluid state. Incoming ^4He immediately cools below the transition temperature and turns superfluid which causes undesired disturbances [81]. A possibility to overcome this problem (which is not implemented in our system) is to precool the incoming He before it enters the 1K-pot, which can be realized by thermal anchoring the inlet siphon at the pot itself (the ^4He from the main reservoir would turn superfluid before entering the 1K-pot). The second possibility (which is implemented in our system) is to stop the incoming ^4He flow completely. We simply would close the needle valve to the main He reservoir and operate the 1K-pot in single shot mode. This avoids a sudden phase transition of the He inside the pot. The volume of our 1K-pot is designed such, that we can operate the DR at lowest circulation for six hours until the pot is empty.

At higher ^3He circulation rates also the increased heat load to the 1K-pot can cause boiling of the liquid inside. The strategy to prevent vibrations in this case is to run the dilution cycle with a very low ^3He circulation rate without additional heater power applied to the Still. This minimizes the heat load to the 1K-pot and prevents the boiling of ^4He .

Sample transfer capability and link to the UHV system

A speciality of this particular cryostat design is the link to the UHV sample preparation chamber, from which we transfer tips and samples into the STM. The cryostat features a

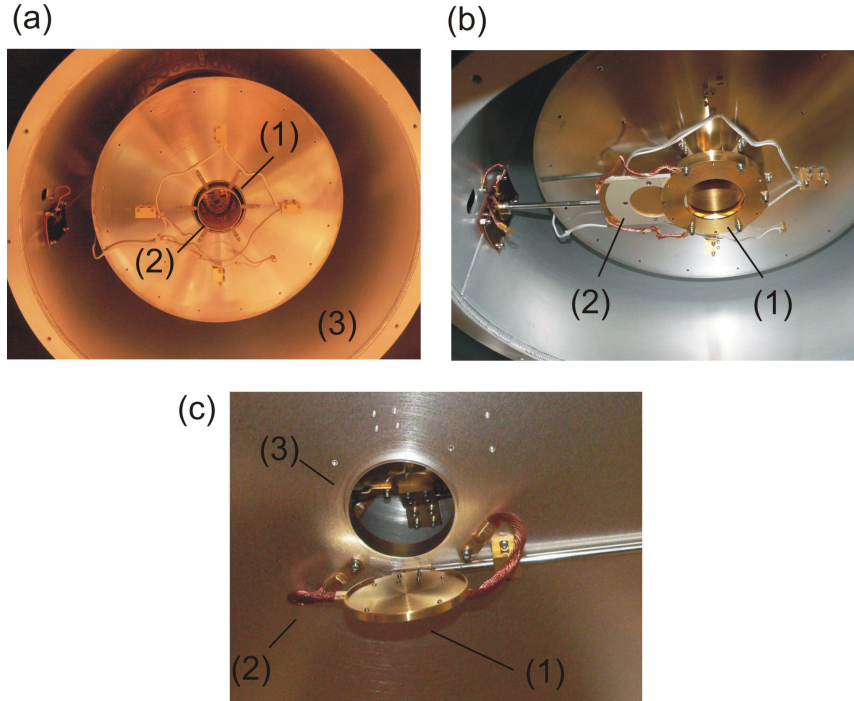


Figure 4.7: Arrangement of the radiation shutters. (a) View from the bottom into the partially assembled cryostat. (1) Magnet bore, (2) part of the still radiation shield that extends out of the magnet bore, (3) encapsulating 77K radiation shield. (b) Assembled still shutter. The image shows the shutter clamp (1) and the moving parts (2). (c) Encapsulation by the 77K radiation shield. The shutter cap (1) can be rotated by 90 degree to give access to the experiment (3). Thermalization braids (2) act as a thermal link to the shield.

bottom loading mechanism and therefore it is necessary to implement a door through the radiation shields which encapsulate the dilution stage (Fig. 4.7). The shutters for the 77 K and 4 K shields are little caps that open a passage by rotating it about an angle of 90° (Fig. 4.7 (c)). The still radiation shield is thermally sealed by a sliding shutter (Fig. 4.7 (a)). The mechanics of all shutters is accessible from outside through appropriate feedthroughs.

The UHV chamber is attached to the cryostat through a CF flange at the bottom.

4.5 Thermometry below 100mK

Temperature in general is measured indirectly by linking a certain physical property to it (vapor pressure, resistance, magnetization) [54,84]. One distinguishes between two classes of thermometers: (i) primary thermometers and (ii) secondary thermometers. In primary thermometry, the theoretical background how a measured physical property is related to the temperature is so good, that the temperature can directly extracted from the measurement of this property. On the other hand in secondary thermometers the measured physical

property depends on the temperature but cannot directly related to it. They need to be calibrated and fitted to a physical law. Secondary thermometers are mostly used in low temperature experiments because they are more reliable and accurate. They should fulfill the following requirements:

- thermometers should have a high temperature resolution in the desired temperature range
- they should work in a wide range of operating temperatures
- good reproducibility among different temperature measurements
- good thermalization within the thermometer and with the external environment is essential
- thermal equilibrium should be reached by the thermometer in a short time
- a temperature measurement should introduce a minimum of heating to the remaining experiment
- the sensitivity to noise should be small

In this section, the thermometers which are used in our DR to measure the various temperatures of the dilution stage are described. First the theoretical background including a description of their working principle is given. This is used to explain the calibration procedure.

Thermometers used in our dilution refrigerator

We use three different thermometer types in our system: a magnetization thermometer for measuring temperatures between 5 mK and 200 mK (CMN thermometer), a second magnetization thermometer containing superconducting impurities for calibrating the CMN thermometer, and resistive thermometers containing RuO clusters in a glass matrix. All of them are secondary thermometers. Both magnetization thermometers are mounted to the MC plate. The resistive thermometers are distributed among the 1K-Pot (1-1.5 K), the still (0.5-0.8 K), an intermediate cold plate (60 mK), the mixing chamber and the STM support (15 mK).

CMN thermometer The CMN thermometer measures the magnetization of an electronic paramagnetic test sample which is described by the Curie-Weiss law [85]. Cerium manganese nitrate (CMN) is a paramagnetic salt and has a low ordering temperature of about 2 mK³. A paramagnetic sample has the following temperature dependence of the susceptibility

$$\chi = \mu_0 M/B = \lambda/T \quad (4.18)$$

³ The ordering temperature of CMN can be further decreased by replacing a small amount of the Ce³⁺ ions by La³⁺ ions [79]

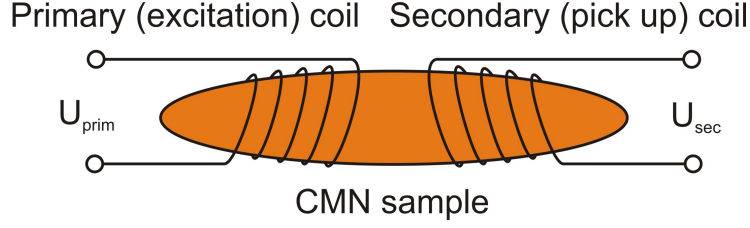


Figure 4.8: Measuring the susceptibility of a paramagnetic sample. A primary coil excites an effective magnetic field B in the sample which is picked up by a secondary coil. This method uses alternating currents which makes it possible to pick up the alternating field by means of an induction law in the second coil.

where μ_0 is the permeability of the vacuum, M the magnetization of the paramagnet, B the magnetic field that is felt by the paramagnetic moments, λ the Curie constant and T the temperature. The resulting magnetic field B which the moments in the paramagnetic dielectric experience, is a combination of the external field B_{ext} , the demagnetization field B_d which depends on the symmetry of the sample and the Weiss field B_W

$$B = B_{\text{ext}} + B_d + B_W. \quad (4.19)$$

This leads to the temperature dependent magnetic susceptibility χ

$$\chi = \chi_0 + \frac{\lambda}{T - \Delta} \quad (4.20)$$

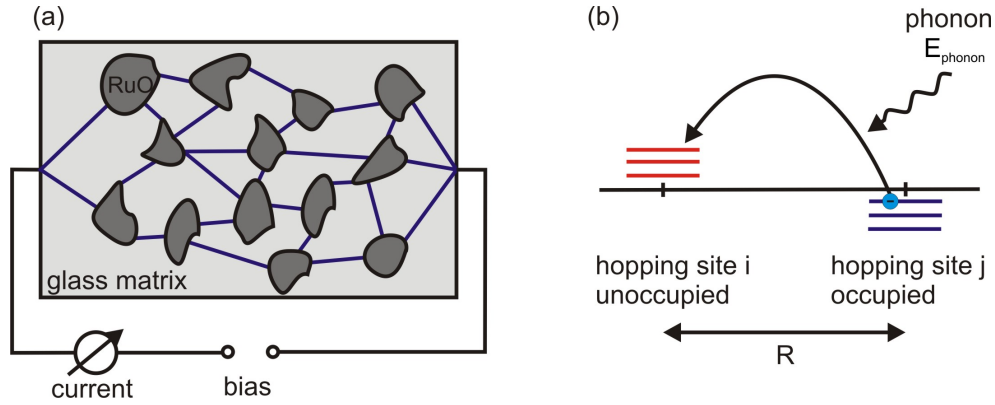
where χ_0 is a background contribution to χ and Δ the Weiss constant. For measuring χ a transformer measurement is performed. The basic setup is depicted in Fig. 4.8. An alternating current is sent through a primary coil, which results in a magnetic field $H = n_1 I_1 / l$. Here n_1 is the number of turns of the primary coil, l the length and I_1 the current which is sent through the coil. This causes a magnetic flux $\Phi = \int_A B dA$ which can be related to the field H ($B = \mu_0 \mu_r H$) and the current I by $\Phi = \mu_0 \mu_r A H = (\mu_0 \mu_r n_1 A) \cdot I_1 / l$. The magnetic field constant is μ_0 and the relative permeability μ_r . The voltage which is induced in the second coil having n_2 turns is $V_2 = -n_2 \cdot d\Phi / dt = (-n_1 n_2 \mu_0 \mu_r A / l) dI_1 / dt = L dI_1 / dt$. What finally is measured is the mutual inductance L which is related to the susceptibility through

$$L = A_1 + A_2 \cdot \chi = a_1 + a_2 / T \quad (4.21)$$

which is the general fitting law for L . All material parameters are included in the fitting parameters a_1 and a_2 .

FPD (Fixed point device) thermometer The main working principle of the FPD is the same as for the CMN thermometer [8]. In the FPD also the mutual inductance of a paramagnetic sample is measured. The difference between the two is that for the FPD superconducting impurities from different materials are added to the paramagnet.

Superconducting Impurity	Transition temperature (mK)
Cd	520
AuIn ₂	208
AuAl ₂	161
Ir	96

Table 4.1: Superconducting impurities and fixed points in the FPD thermometer.**Figure 4.9:** Principle of electron hopping conductivity. (a) The electron has to choose between the paths that are energetically available. (b) An electron is excited from an occupied site j to an unoccupied site i . The energy for this process comes from the absorption of an phonon. The distance R which the electron travels depends on the optimization of the tunneling and hopping probabilities.

These have different superconducting transition temperatures. If the thermometer is cooled through the transition temperature of one of the impurities a well defined jump in the susceptibility of the whole sample will occur. This is due to the Meissner-Ochsenfeld effect. The class of impurities that turned superconducting becomes an ideal diamagnet $\chi_{\text{SC}} = -1$ which influences the the susceptibility of the whole paramagnetic sample. The materials added to the FPD and the corresponding transition temperatures are listed in Tab. 4.1. The jumps can be related to well defined temperatures and are used to calibrate the CMN thermometer. The FPD was precalibrated against the ^3He vapor curve by the manufacturer (JANIS inc.).

Resistive thermometers (RuO-thermometers) The third kind of thermometer is a resistive thermometer [86]. Such thermometer is easy to handle, shows low magnetoresistance [87,88], has a high signal to noise ratio below 100 mK and is very reliable.

The thermometer consists of a resistive film of conducting ruthenium oxide (RuO) clusters in a glass matrix (Fig. 4.9 (a)). They belong to the class of negative temperature

coefficient resistors (NTCs). Electron transport through the film happens by thermally assisted hopping between discrete electronic states near the Fermi level on different clusters as depicted in Fig. 4.9 (b) [89–93]. These states form a narrow band around the Fermi level in which electrons can hop from cluster to cluster by absorbing energy from phonons. The lower the temperature, the less probable is the hopping process and therefore the higher the resistance of the sample. The probability of this process to occur was described by Sir Neville Mott, who first pointed out that hopping to the nearest neighbor site is not the most probable process at low temperatures [89]. At a given site the density of states near the Fermi level $n(R)$ within the radius R is

$$n(R) = (4\pi/3)R^3 N(E_F). \quad (4.22)$$

For the hopping process through a distance R the lowest possible activation energy ΔE is the reciprocal of the quantity in Equ. 4.22

$$\Delta E = \frac{1}{n(R)} = \frac{1}{(4\pi/3)R^3 N(E_F)}. \quad (4.23)$$

The probability p_{hop} of this process is proportional to

$$p_{\text{hop}} \sim \exp(-\Delta E/k_B T). \quad (4.24)$$

The transport process over larger distances includes thermally assisted hopping and tunneling in series. The probability for tunneling p_{tunnel} is proportional to

$$p_{\text{tunnel}} \sim \exp(-2\alpha R) \quad (4.25)$$

where $1/\alpha$ is the decay length of the localized wave function. The combined probability $p = p_{\text{hop}} \cdot p_{\text{tunnel}}$ is therefore

$$p \sim \exp(-2\alpha R) \exp(-\Delta E/k_B T). \quad (4.26)$$

The optimal distance R for the combined transport process is found when p becomes maximal. This happens when $f(R) = 2\alpha R + 3/(4\pi R^3 N(E_F))$ becomes minimal. The condition $f'(R) = 0$ yields $R = (9/(8\pi N(E_F)\alpha k_B T))^{1/4}$. The probability and thus the conductivity is of the form

$$\sigma = A \exp\left(\frac{-A'}{T^{1/4}}\right). \quad (4.27)$$

A modification of this formula was given by Efros and Shklovskii [94] who included also coulomb interaction between the hopping centers and got a different temperature exponent $x=1/2$ instead of $x=1/4$. Anyhow these models are not very satisfying at temperatures below 30 mK and do not describe a saturation of the resistance which we measure at lowest temperature. Various models have been proposed to eliminate discrepancies and some are summarized by Abe *et al.* [95].

As none of them is fitting our temperature data correctly we applied an empirical general fitting function for the conductivity of a RuO thermometer which is based on the Mott hopping law (Equ. 4.27)

$$\sigma_{\text{General}} = A_0 \exp \left[- \left(\frac{A_1}{T - T_0} \right)^x \right] + \sigma_0 \quad (4.28)$$

where A_0 , A_1 , T_0 , x and σ_0 are fitting parameters. A_0 is a scaling factor to the exponential function and σ_0 a temperature independent background. x is the exponent that distinguishes between Mott and Efros hopping. A_1 is a effective temperature that includes the density of states near the Fermi energy and the decay length of the wave functions of the localized states. T_0 is used in Equ. 4.28 to include a saturation of the conductivity at very low temperatures. The formula describes the low temperature behavior of the resistors very well. As we measure in our experiments the resistance we have to relate it to the conductivity simply through

$$R = \frac{1}{\sigma}. \quad (4.29)$$

Calibration procedure of the various thermometers

The procedure of temperature calibration is summarized in Fig. 4.10. In the first step the CMN thermometer is calibrated with the help of the FPD. Starting from base temperature, the MC is slowly warmed up crossing the different transitions of the FPD. In the middle of every transition the corresponding CMN value is recorded. As the transition temperatures are known, the CMN values are plotted against the inverse transition temperature as shown in Fig. 4.11. For fitting the data Equ. 4.21 is used.

In a next calibration step, the temperature scale of the CMN thermometer is used to calibrate the RuO thermometers at mixing chamber and STM support. It is possible to include the STM support RuO thermometer into the calibration because it can be assumed that its temperature deviates not much from the temperature of the mixing chamber. If the difference in temperature is 1 mK we nevertheless have an mismatch of 10 % between the real and the calibrated temperature of this RuO thermometer when the cryostat has a temperature of 10 mK. This value is still acceptable because the RuO thermometers are used to give an indication of the temperature.

A slow cool down of the cryostat from approximately 0.8 K to base temperature is performed. This procedure gives a set of CMN-temperature RuO-resistance pairs for each thermometer. The results of this calibration procedure are shown in Fig. 4.12. The resistance is converted into a conductivity to be fitted to Equ. 4.28. Rearranging Equ. 4.28 yields the conductivity dependence of the temperature

$$T = \frac{A_1}{\left(-\ln \frac{\sigma - \sigma_0}{A_0} \right)^{\frac{1}{x}}} + T_0. \quad (4.30)$$

The corresponding fitting parameters for the RuO thermometers at MC and STM support are summarized in Tab. 4.2. It is interesting to note, that we extract values for the

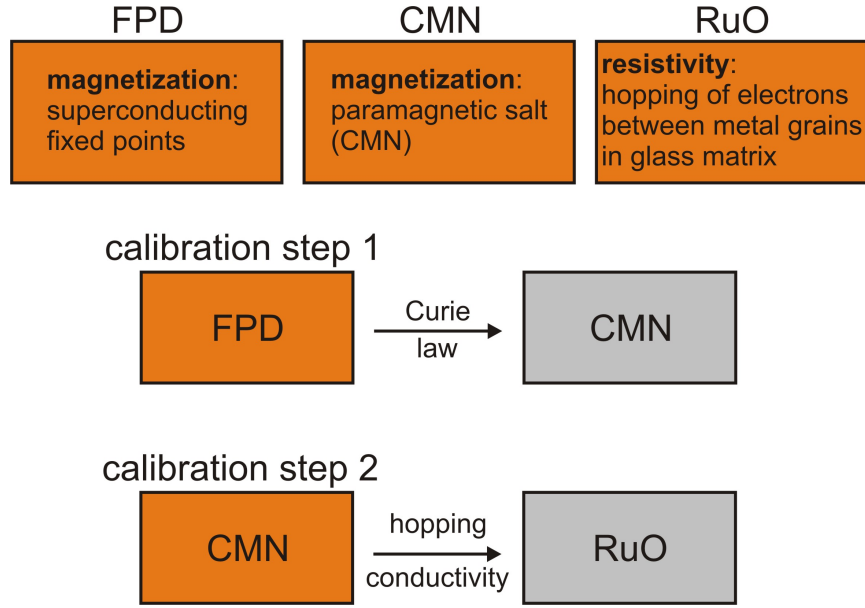


Figure 4.10: Schematic of temperature calibration. The CMN thermometer is calibrated against the fixed point device (FPD) in a first step. In a second step the CMN temperature scale is used to calibrate the resistive thermometers.

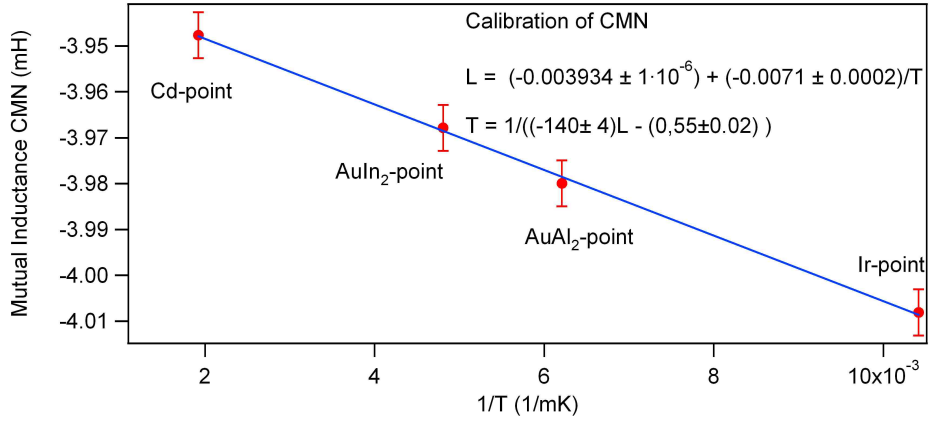


Figure 4.11: CMN thermometer calibration curve. The inverse temperatures known from the fixed point transitions are plotted against the CMN thermometer magnetization values. The data set can be fitted to the Curie-Weiss law (Equ. 4.21) to obtain a direct correlation between temperature and CMN magnetization.

Thermometer	$A_0 \times 10^{-3} (\Omega^{-1})$	$A_1 \times 10^3 (\text{mK})$	x	$\sigma_0 \times 10^{-6} (\Omega^{-1})$	$T_0 (\text{mK})$
MC	8.1 ± 0.1	64.7 ± 0.5	0.258 ± 0.001	1.04 ± 0.03	11.8 ± 0.4
STM support	6.0 ± 0.1	30.6 ± 0.5	0.283 ± 0.001	1.70 ± 0.03	9.6 ± 0.4

Table 4.2: Results of the resistive thermometer calibration.

$B_0 (\text{mK})$	$B_1 (\text{mK s}/\mu\text{mole})$	$B_2 (\text{mK s}^2/\mu\text{mole}^2)$
18.6 ± 0.8	-0.08 ± 0.01	0.00026 ± 0.00005

Table 4.3: Parameters to the base temperature fit.

exponent x near to $1/4$ which indicates the Mott hopping behavior of the transport in our RuO thermometers.

4.6 Cooling power and performance of the system

The two most important quantities for characterizing the performance of a dilution cryostat are the base temperature and the cooling power at a temperature of 100 mK. Both values depend on the ^3He circulation rate which is regulated by applying heat to the still chamber. The more ^3He atoms the phase boundary cross, the more cooling power has the refrigerator resulting in a decrease of the MC temperature. On the other hand, a larger ^3He circulation rate introduces more heat to the mixing chamber. If no additional heat is applied to the mixing chamber, the optimum in the relation between the heat leak through the circulating ^3He and the cooling power of the mixing chamber defines the base temperature of the cryostat.

To estimate the base temperature the Still heater voltage is increased in discrete steps and the corresponding flow is measured. When the MC temperature is settled its value is recorded and the heating power to the still is increased further. Fig. 4.13 shows the temperatures plotted against the measured circulation rate indicating a quadratic behavior. The following empirical law was used to fit the data

$$T = B_0 + B_1 \dot{n} + B_2 \dot{n}^2 \quad (4.31)$$

where \dot{n} is the ^3He circulation. The fitting results are summarized in Tab. 4.3. For our system the optimal circulation rate to obtain the base temperature of $11.4 \pm 0.3 \text{ mK}$ is $\dot{n} = 160 \pm 1 \mu\text{mole/s}$.

The cooling power at 100 mK (Fig. 4.14) is obtained in the following way: The circulation is set to a high value at which the mixing chamber has the most cooling power and the cryostat is still operating stable. Heat is applied to the mixing chamber by a heater which is placed at the mixing chamber plate. The heater is adjusted such that the equilibrium

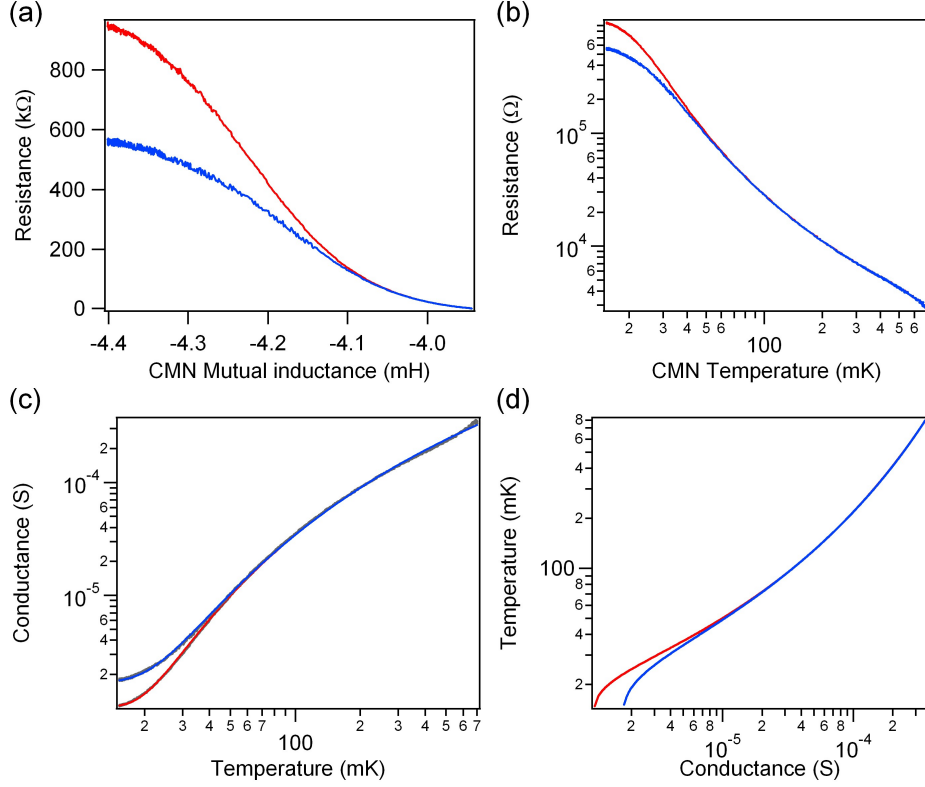


Figure 4.12: Calibration of RuO thermometers. Red: data from RuO thermometer at MC, blue: data from RuO thermometer at STM support. Double logarithmic plots are used to focus on the low temperature region where a saturation of the resistance occurs. (a) The temperature of the cryostat is slowly varied. CMN mutual inductance and RuO thermometer resistance are simultaneously recorded. Care was taken to keep all devices in thermal equilibrium. (b) The CMN thermometer temperature is used to define the temperature scale. (c) The resistance is converted into a conductance through Equ. 4.29 and fitted to Equ. 4.28. (d) From this fit the parameters for the final calibration curve are obtained.

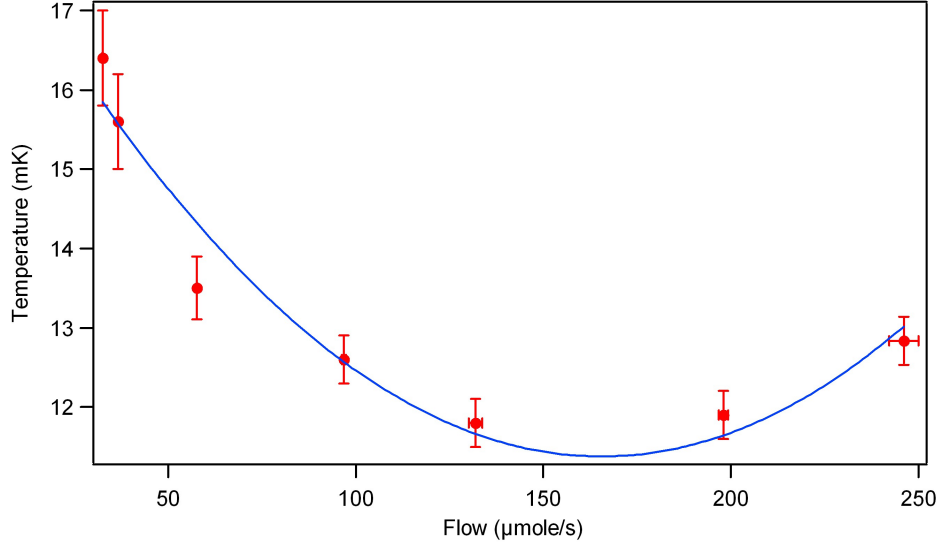


Figure 4.13: Base temperature at different ^3He circulations. The lowest temperature which is achieved with the cryostat is at a ^3He flow rate, where the heat introduced to the MC by the incoming ^3He and the cooling power \dot{Q} are in an optimal relation. This is exactly the flow rate where the parabola has a minimum. For fitting the data Equ. 4.31 was used.

temperature is a bit below 100 mK. At this temperature the heat input through the heater equals the cooling power of the mixing chamber. A second equilibrium temperature is set which is a bit above 100 mK. A linear interpolation between the two points gives the cooling power at 100 mK. For our system it is $396 \pm 5 \mu\text{W}$.

For a ^3He flow rate \dot{n} the general cooling power curve is depicted in Fig. 4.15. The ^3He circulation was set to $43 \mu\text{mole/s}$ for this experiment. In steps the external heating power is increased while measuring the temperature of the MC. In the linear range of the curve, the applied heating power corresponds directly to the cooling power of the mixing chamber at the given temperature because both compensate in this case. In the nonlinear region one has additional contributions from the heat leak due to the ^3He circulation. Fitting this curve to Equ. 4.17 gives an external heat leak due to the flow rate of ^3He $\dot{Q}_{\text{ext}} = 0.8 \pm 0.4 \mu\text{W}$. The flow rate extracted from the fit is $\dot{n} = 35 \mu\text{mole/s}$.

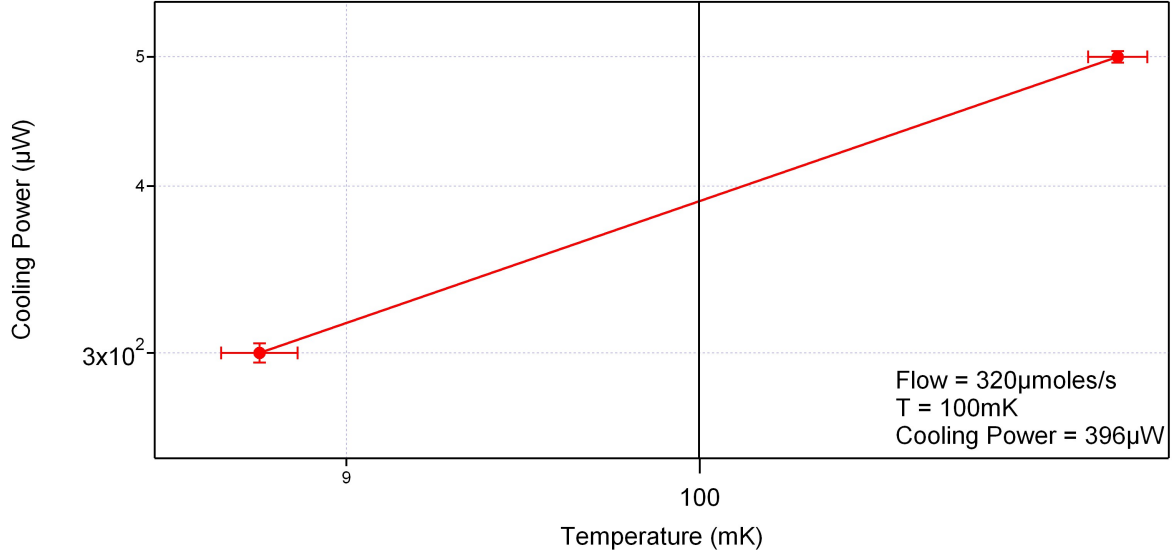


Figure 4.14: Estimation of the maximal cooling power. ^3He is circulated with the largest flow rate at which the cryostat is still stable. Heat is applied to the MC. The heater power is recorded slightly below and above 100 mK. Both points are used to extract the power at 100 mK.

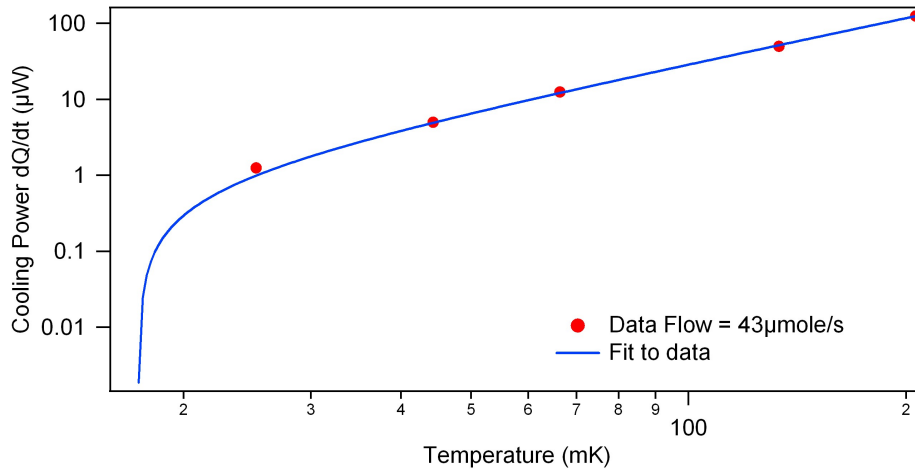


Figure 4.15: Full cooling power curve for a circulation of 43 μ mole/s. For fitting the data Equ. 4.17 was used.

Chapter 5

Realization of the mK-STM

Any STM design has to fulfill certain requirements. The need for a stable tunneling junction demands a low vibration level of the experimental chamber which houses the STM. Beside this we are working at temperatures below 100 mK, in UHV and in high magnetic fields up to 14 T. These are three extreme fields in instrumentation that have to be combined within one system. This chapter gives an overview about the strategy we choose to realize the mK-STM system.

The most critical point is the tunneling junction between tip and sample. Due to the distance sensitivity of the tunneling current, the spacing between the two needs to be well controlled. A variation in distance of 1 Å already results in a change in the tunneling current of one order of magnitude. Therefore a high mechanical stability between tip and sample is required. Normally, this has to be in the order of 1 pm or below. In our case the STM unit will be attached to a dilution refrigerator, where always a certain amount of ^3He is circulating introducing mechanical noise. Our STM has to be as insensitive to external disturbances as possible. A simple one dimensional mechanical model of our STM unit is given in Sec. 5.1. This model was used to extract optimization criteria for the geometrical design to limit the influences from vibrations coming from the inside of the cryostat [96].

Special care has to be taken in the material selection for the STM. To ensure the compatibility with UHV, all materials in use have to have a low vapor pressure. As the STM is to operate at temperatures below 100 mK, we need to take special cryogenic considerations into account. As the thermal conductivity through phonons is not efficient any more at low temperatures, parts through which cooling is realized should be machined out of metals. Preferred is high purity silver because it shows good thermal conductivity in the whole temperature range. No materials should be used that become superconducting, because they have nearly zero thermal conductivity. This, for example excludes titanium as material for the STM unit because it undergoes a superconducting transition at 400 mK. For the local investigation of magnetic systems and the use of the STM in high magnetic fields up to 14 T all materials have to be paramagnetic without any permanent magnetic moment. The actual design of the STM unit is explained in Sec. 5.2.

Further, the STM needs to have the possibility to exchange sample and tip without breaking the UHV. Our solution for a simple and reliable tip and sample transfer is given

in Sec. 5.3.

For the whole setup we followed a modular design strategy. This means we imagine the cryostat and the STM as two independent units. This has the advantage that both systems can be tested independently from each other which simplifies troubleshooting procedures. We included the possibility to remove the STM unit from the cryostat without the need of disassembling the whole refrigerator. To connect the STM to the cold spot of the cryostat and to extend it into the center of the magnetic field, we use a link structure. This structure serves as a rigid link and extends wires and cables from the MC to the STM (Sec. 5.4).

We designed a UHV chamber offering basic possibilities of *in situ* sample preparation. It is directly mounted to the cryostat bottom. The UHV chamber is explained in Sec. 5.6.

Mechanical vibrations transmitted to the cryostat through the floor can cause disturbances at the STM unit. This prevents a stable tunneling contact between tip and sample. To ensure a low vibration level, the whole cryostat including UHV chamber rests on a set of active and passive dampers. To prevent the coupling of mechanical noise through the pumping lines to the cryostat, they are additionally anchored on an actively damped platform. To avoid mechanical disturbances from the pumps to the floor level at which the isolation stage is placed, we put them into a separate room. They are assembled into a frame which is hanging from the ceiling through a set of springs. This avoids any contact between the pumps and the floor. The concept of vibration isolation for our system is described in Sec. 5.7.

As the tunneling current is detected through the STM tip all signal lines connecting tip and sample demand a low electrical noise level. Electrical noise decreases the energy resolution in the spectroscopy mode of STM dramatically. Furthermore, radio frequency radiation inside the wires which is picked up from the lab environment needs to be blocked at the input of the cryostat. This demands careful filtering of all signal lines going into the UHV space of the DR. The electronic concept and the filtering is described in Sec. 5.8.

We tested the STM unit independently from the dilution cryostat in two different systems mimicking the final setup. One of these systems works at room temperature while the other is used for variable temperature measurements. Results from these systems are presented in Sec. 5.9.

An overview of the final mK-STM setup is shown in Fig. 5.1. The cryostat is mounted in an upper lab from which we have access to all electrical connections concerning the STM unit and the thermometry of the cryostat. The UHV preparation chamber is attached to it from a lower lab. In this chamber we prepare our samples to investigate and transfer them into the STM unit.

5.1 Optimization criteria for an STM

In this section an improved model for an STM design is given which is optimized to be as less sensitive to external disturbances as possible. The results are also published at the following reference [96]. As introduced in Ch. 2 the tunneling current in an STM depends

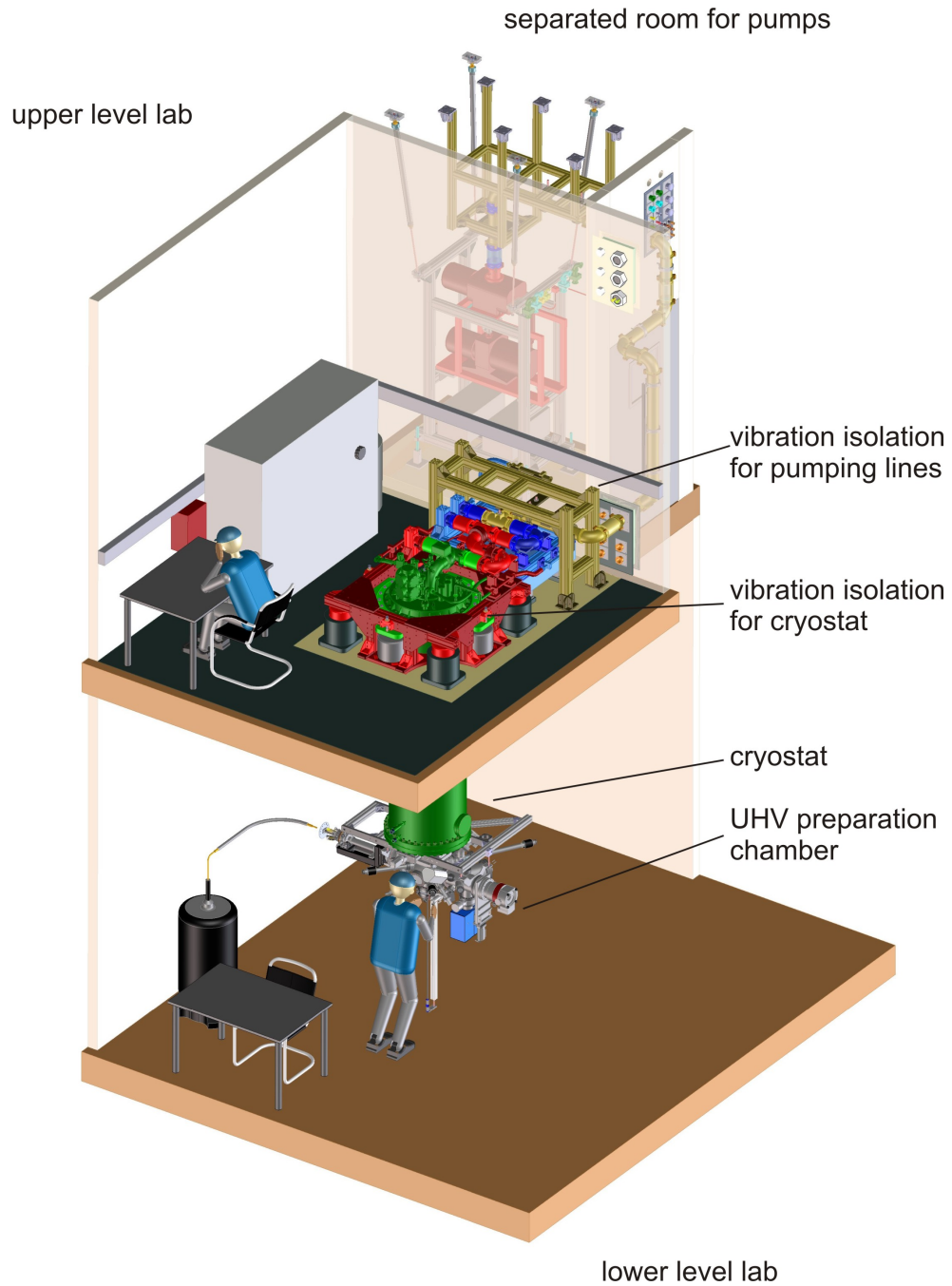


Figure 5.1: Overview of the mK-STM setup. The cryostat rests on a vibration isolation stage in an upper floor lab. It hangs through the ceiling into a lower lab where the access to the UHV preparation chamber is realized. The pumps are located in a separated room hanging from the ceiling to avoid mechanical disturbances to the floor on which the vibration isolation is placed.

exponentially on the tip-sample distance [5–7]. This makes it an extremely sensitive experimental tool. During a topography scan the tip-sample distance is controlled by a feedback loop such that the tunneling current remains constant. It is necessary to minimize the effects of external mechanical disturbances inducing an unwanted background signal in the tunneling current, since it is *a priori* impossible to distinguish it from the actual signal. Therefore, care must be taken to isolate the measurement setup as effectively as possible from the surrounding environment. Different approaches are various active and/or passive damping stages, on which the whole experimental setup is resting [97–102]. Others are to push the resonance frequencies as high as possible by building the STM as rigid as possible, or to decouple the STM, e. g. by means of an eddy current damping stage [103, 104]. These approaches work for most experimental setups quite successfully. However, under some conditions it is not possible or sufficient to apply the above damping mechanisms. For example, eddy current damping does not work if magnetic fields are to be applied, and external damping stages may be insufficient, when operating a flow cryostat [105, 106] or a dilution refrigerator because they present internal sources of mechanical noise, which are not adequately damped by external damping stages.

The main task is to reduce the response of the tip-sample distance to disturbances, which induce an unwanted signal in the tunneling current. The idea is to optimize the design of the STM itself, so that the response of the tip and the sample to disturbances is in phase and with the same amplitude over a broad range of frequencies. In this way, the response of the tip-sample distance to disturbances can be significantly reduced. In the following a simple one-dimensional model is presented, from which a number of optimization criteria for different STM designs are derived. The results presented here for STMs can also be extended to other scanning probe techniques. In the following, three STM designs are discussed, which essentially only differ by how the coarse approach mechanism is implemented. Schematics of these designs are shown in the left panels of Fig. 5.2. For the modeling we only consider the immediate surroundings of the tip and the sample. All systems employ a coarse motion mechanism (4) as well as a scan piezo (3), which moves the tip (2). They are connected to the rest of the experimental structure by a base plate (5), from which disturbances couple to the STM. The design in Fig. 5.2(a), which we have constructed, uses an attocube coarse-motion piezo stage. However, in the calculation this coarse motor can also be substituted by a different coarse-motion mechanism, e. g. the “Pan”-design [31]. The sample (1) is held by a cylindrical housing (6). The other designs shown in Fig. 5.2(b) and (c) are two “beetle”-type STMs [30], which differ only in the location of the scan piezo (3) and the sample (1). In this design the coarse motion piezos (4) are mounted on the base plate (5). The ramp (7) holds the sample (1) or the scan piezo (3) in Fig. 5.2(b) or (c), respectively.

In order to formulate a simple, mathematical model for these different STM designs, a few assumptions and simplifications have to be made. The simplified models are shown in the right panels of Fig. 5.2. They focus on the disturbances and the motion of the system to which the tip-sample distance is most sensitive. Therefore, these models are one-dimensional and consider only the longitudinal motion of the flexible components, while any bending motion is neglected. Since the bending motion has nonetheless some

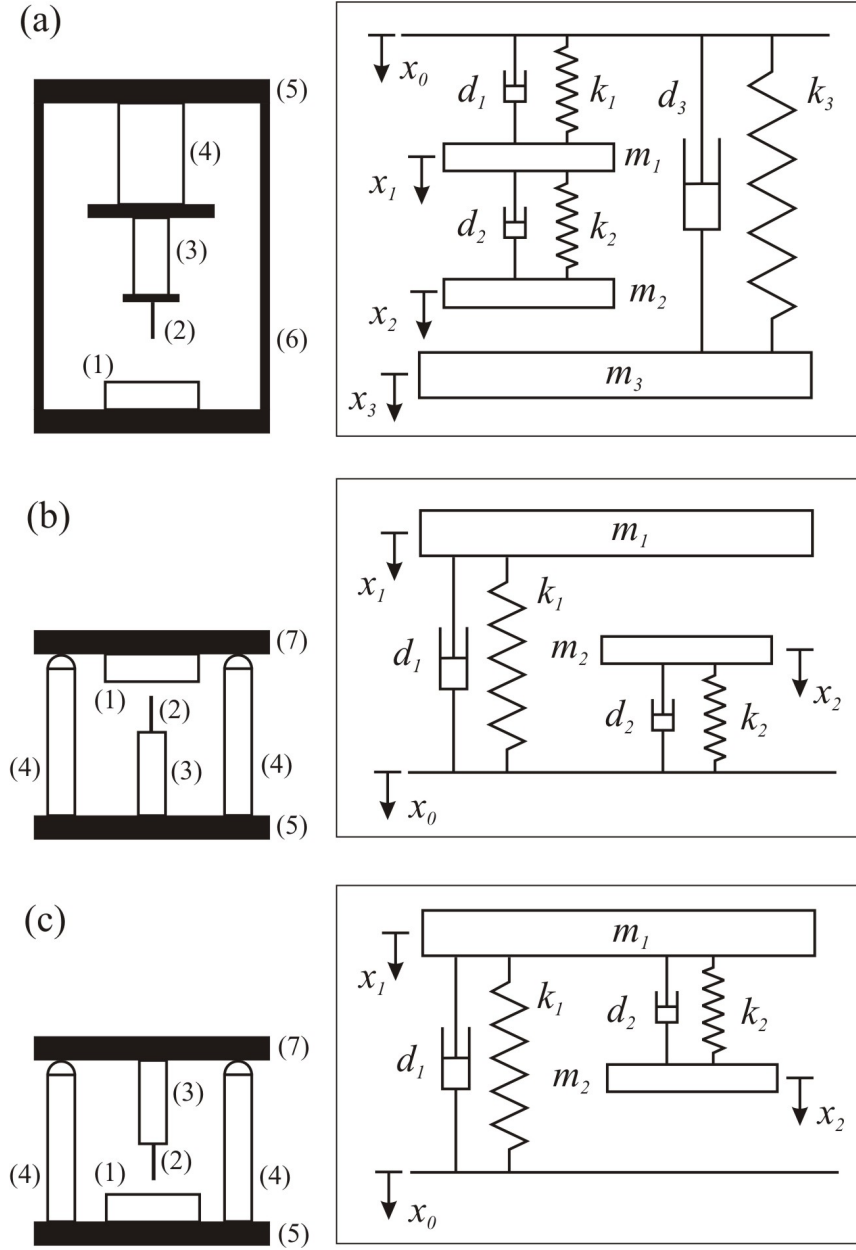


Figure 5.2: Different design concepts for an STM: (a) Design using an attocube coarse-motor (model 1), (b) “beetle”-type STM with a moving sample (model 2), (c) “beetle”-type STM with a moving tip (model 3). (1) sample, (2) tip, (3) scan piezo, (4) coarse motion piezo(s), (5) fixed mounting plate, (6) cylinder to hold the sample, (7) ramp moving on top of the coarse piezos.

Model	m_1	m_2	m_3	k_1	k_2	k_3
1	15	2	200	600	26.4	650
2 and 3	20	1.8	n/a	79.2	26.4	n/a
1 (opt)	15	2	67.681	600	26.4	650

Table 5.1: Typical values for the different masses m_i (in g) and spring constants k_i (in N/ μ m) in the different STM models. Models 1, 2, and 3 refer to Fig. 5.2(a), (b), and (c), respectively.

influence on the STM performance, it will be considered separately below. All piezos as well as the cylinder (6) in Fig. 5.2(a) are modelled as massless springs (spring constant k_i) with internal viscous damping d_i [107]. All other bodies (tip, sample, ramp, etc.) are assumed to be rigid bodies with mass m_i . Typical values for these quantities are given in Table 5.1. The assumption to separate masses and spring constants is feasible because by design the different bodies are connected in series and the piezos are usually softer in relation to other parts of the construction [107, 108]. To make the model more accurate, an effective mass of a part modelled as a spring can be attributed accordingly to the rigid bodies. The correspondence between the different masses and springs as well as the actual parts in the STM designs can be easily seen in Fig. 5.2.

To each mass m_i a coordinate x_i is assigned, which describes the deviation from the steady state position. The coordinate x_0 is associated with the disturbance, i. e. it models the motion of the base plate. The equations of motion [108] are:

$$\mathbf{M}_j \ddot{\vec{x}} = \mathbf{K}_j \vec{x} + \mathbf{D}_j \dot{\vec{x}} + \mathbf{H}_j \ddot{x}_0. \quad (5.1)$$

The index j refers to the model number 1, 2, and 3. The coordinates x_i are combined in the displacement vector $\vec{x} = [x_0 \ x_1 \ x_2 \ x_3]^T$. \mathbf{M}_j , \mathbf{K}_j , and \mathbf{D}_j are the mass, stiffness, and damping matrices, respectively. The vector \mathbf{H}_j is necessary to incorporate the second time derivative of the disturbance \ddot{x}_0 into the equation, which is comparable to a force exciting the system. The different matrices are:

$$\begin{aligned} \mathbf{M}_1 &= \begin{bmatrix} 1 & 0 & 0 & 0 \\ 0 & m_1 & 0 & 0 \\ 0 & 0 & m_2 & 0 \\ 0 & 0 & 0 & m_3 \end{bmatrix}, \quad \mathbf{K}_1 = \begin{bmatrix} 0 & 0 & 0 & 0 \\ k_1 & -k_1 - k_2 & k_2 & 0 \\ 0 & k_2 & -k_2 & 0 \\ k_3 & 0 & 0 & -k_3 \end{bmatrix}, \\ \mathbf{D}_1 &= \begin{bmatrix} 0 & 0 & 0 & 0 \\ d_1 & -d_1 - d_2 & d_2 & 0 \\ 0 & d_2 & -d_2 & 0 \\ d_3 & 0 & 0 & -d_3 \end{bmatrix}, \quad \mathbf{H}_1 = \begin{bmatrix} 1 \\ 0 \\ 0 \\ 0 \end{bmatrix}, \\ \mathbf{M}_2 &= \begin{bmatrix} 1 & 0 & 0 \\ 0 & m_1 & 0 \\ 0 & 0 & m_2 \end{bmatrix}, \quad \mathbf{K}_2 = \begin{bmatrix} 0 & 0 & 0 \\ k_1 & -k_1 & 0 \\ k_2 & 0 & -k_2 \end{bmatrix}, \end{aligned} \quad (5.2)$$

$$\mathbf{D}_2 = \begin{bmatrix} 0 & 0 & 0 \\ d_1 & -d_1 & 0 \\ d_2 & 0 & -d_2 \end{bmatrix}, \mathbf{H}_2 = \begin{bmatrix} 1 \\ 0 \\ 0 \end{bmatrix}, \quad (5.3)$$

$$\mathbf{M}_3 = \begin{bmatrix} 1 & 0 & 0 \\ 0 & m_1 & 0 \\ 0 & 0 & m_2 \end{bmatrix}, \mathbf{K}_3 = \begin{bmatrix} 0 & 0 & 0 \\ k_1 & -k_1 - k_2 & k_2 \\ 0 & k_2 & -k_2 \end{bmatrix},$$

$$\mathbf{D}_3 = \begin{bmatrix} 0 & 0 & 0 \\ d_1 & -d_1 - d_2 & d_2 \\ 0 & d_2 & -d_2 \end{bmatrix}, \mathbf{H}_3 = \begin{bmatrix} 1 \\ 0 \\ 0 \end{bmatrix}. \quad (5.4)$$

Using the state vector $\vec{z} = [\vec{x}^T \dot{\vec{x}}^T]^T$ as well as the input variable $u = \ddot{x}_0$ and defining y as the output variable, the equations of motion in state space form [109] can be written as

$$\begin{aligned} \dot{\vec{z}} &= \mathbf{A}_j \vec{z} + \mathbf{B}_j u, \\ y &= \mathbf{C}_j \vec{z}, \end{aligned} \quad (5.5)$$

where the matrices \mathbf{A}_j , \mathbf{B}_j , and \mathbf{C}_j are defined as:

$$\begin{aligned} \mathbf{A}_j &= \begin{bmatrix} 0 & \mathbf{E} \\ \mathbf{M}_j^{-1} \mathbf{K}_j & \mathbf{M}_j^{-1} \mathbf{D}_j \end{bmatrix}, \\ \mathbf{B}_j &= \begin{bmatrix} 0 \\ \mathbf{M}_j^{-1} \mathbf{H}_j \end{bmatrix}, \\ \mathbf{C}_1 &= [0 \ 0 \ 1 \ -1 \ 0 \ 0 \ 0 \ 0], \\ \mathbf{C}_2 &= [0 \ 1 \ -1 \ 0 \ 0 \ 0], \\ \mathbf{C}_3 &= [1 \ 0 \ -1 \ 0 \ 0 \ 0]. \end{aligned} \quad (5.6)$$

The output matrices \mathbf{C}_j are chosen such that the output variable y yields the tip-sample distance. Taking the Laplace transform of Equ. 5.5 (the transformed variables are denoted by the corresponding capital letters), the corresponding transfer functions $G_j(s)$ can be obtained [109]:

$$G_j(s) = \frac{Y(s)}{X_0(s)} = s^2 \mathbf{C}_j (s\mathbf{E} - \mathbf{A}_j)^{-1} \mathbf{B}_j. \quad (5.7)$$

The factor s^2 originates in the Laplace transform ($\ddot{x}_0 \mapsto s^2 X_0$) of the input variable.

The results are displayed for typical values of the masses and spring constants (see Table 5.1) in a magnitude Bode plot in Fig. 5.3 for model 1, model 2, and model 3. Some general features are the fairly high resonance frequencies in all three models. For excitation frequencies below the lowest resonance frequency, the response of the tip-sample distance decreases as the excitation frequency decreases. In this regime the individual transfer functions of tip and sample are close to one resulting in a value close to zero for the transfer function of the tip-sample distance, which shows that the response is almost in phase and

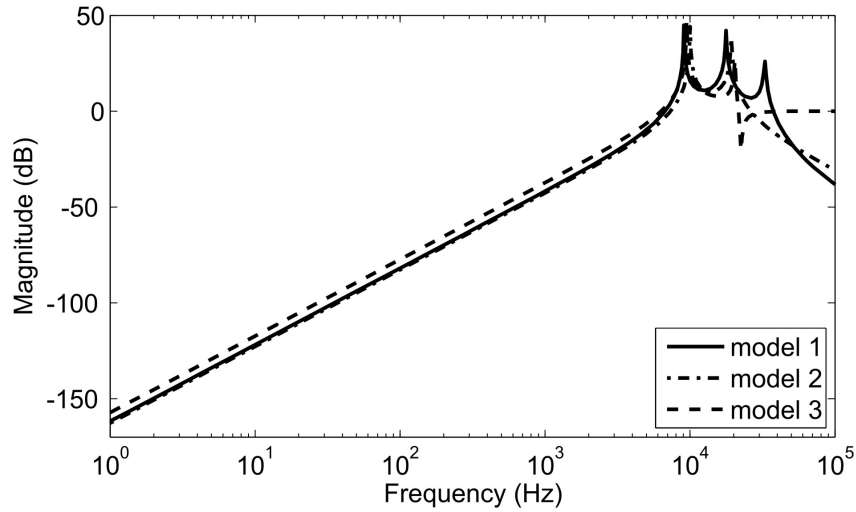


Figure 5.3: Magnitude Bode plot for the transfer functions of the tip-sample distance in the design using an attocube coarse-motor (model 1), the “beetle”-type STM with a moving sample (model 2), and the “beetle”-type STM with a moving tip (model 3). Typical values have been used for the design parameters.

with the same amplitude. For excitation frequencies above the highest resonance frequency the values for the transfer functions decrease again for models 1 and 2. Here, the individual transfer functions approach zero resulting again in a value close to zero for the transfer function of the tip-sample distance. For model 3, however, the value approaches one (0 dB). This can be understood by seeing that the sample in this model is directly coupled to the base plate and, therefore, to the excitation. The response for the tip assembly, however, will decrease with increasing excitation frequency leaving the system with an oscillating sample.

The frequency range relevant for the performance of the STM lies well below the lowest resonance frequency shown in Fig. 5.3. At 80 Hz, for example, we find a value of about -84 dB, which means a reduction of about four orders of magnitude in relation to the excitation amplitude. This means that the excitation amplitude has to be smaller than 10 nm if the resulting oscillations of the tip-sample distance, i. e. the noise in the z -direction, should not exceed 1 pm.

To improve the performance, the objective is to minimize the response of the tip-sample distance to disturbances coupling to the base plate. The ideal case would be if the transfer function $G_i(s)$ were zero over the whole frequency range meaning no response to disturbances. This, however, is even in the simple models presented here not always

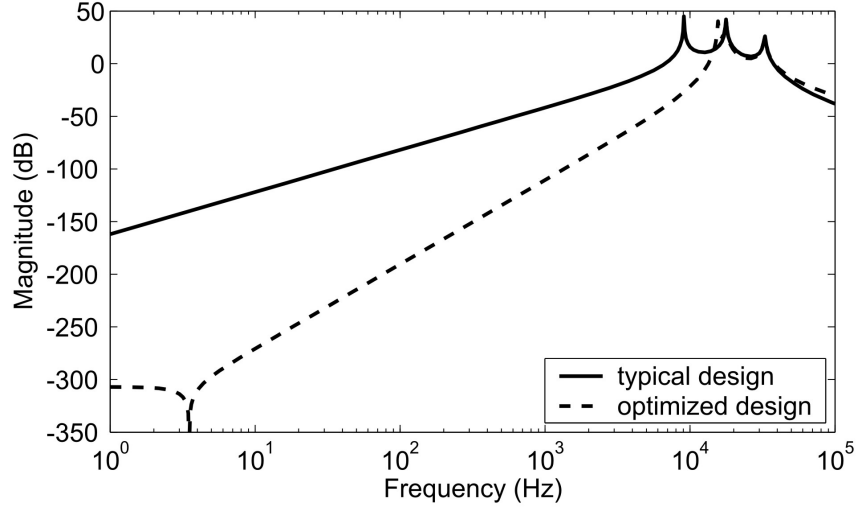


Figure 5.4: Magnitude Bode plot for the “typical” and optimized transfer functions of the tip-sample distance in model 1. The values are given in Table 5.1. The improvement can be several orders of magnitude.

possible. The transfer functions for the different models are in analytical form:

$$\begin{aligned}
 G_1(s) &= \frac{1}{\frac{m_1 m_2}{k_1 k_2} s^4 + \left(\frac{m_2}{k_2} + \frac{m_1 + m_2}{k_1}\right) s^2 + 1} - \frac{1}{\frac{m_3}{k_3} s^2 + 1}, \\
 G_2(s) &= \frac{1}{\frac{m_1}{k_1} s^2 + 1} - \frac{1}{\frac{m_2}{k_2} s^2 + 1}, \\
 G_3(s) &= \frac{1}{\frac{m_1 m_2}{k_1 k_2} s^4 + \left(\frac{m_2}{k_2} + \frac{m_1 + m_2}{k_1}\right) s^2 + 1} - 1.
 \end{aligned} \tag{5.8}$$

The damping values have been set to zero here and in the following, since they are assumed to be small compared to the other quantities. The main result is not altered by this assumption. The optimization criteria (i. e. $G_i(s) = \min$) for each model become evident by comparing the coefficients in Eq. 5.8. For model 1 the highest order term s^4 can be neglected because in the low frequency range, which is of interest here, it is small compared to the other terms. For models 1 and 2 the conditions are:

$$\begin{aligned}
 \text{Model 1} &: \frac{m_3}{k_3} = \frac{m_2}{k_2} + \frac{m_1 + m_2}{k_1}, \\
 \text{Model 2} &: \frac{m_1}{k_1} = \frac{m_2}{k_2}.
 \end{aligned} \tag{5.9}$$

For model 3 no optimization condition can be found. The only way to improve the performance of this type of STM would be to build it as stiff and light as possible to push the resonance frequencies as high as possible. This is not necessary for the other two models because in these cases an optimization means a matching of resonance frequencies.

For model 2 the transfer function actually becomes identically zero. This represents the ideal case. For model 1 this yields a minimum in response, which is displayed in Fig. 5.4 for the values given in Table 5.1 (see Model 1 (opt)). The mass m_3 has been adjusted to meet the optimization criterion in Equ. 5.9. A general improvement of the response in the lower frequency range for the optimized response (dashed line) compared to the response for the “typical” values (solid line) can be observed. At 80 Hz, for example, the optimized response now shows a reduction of -198.6 dB, which is an improvement by almost six orders of magnitude. In this case a 1 pm noise level can theoretically be achieved already for disturbances less than 1 mm.

Even though the models used here are quite simple, they do show whether or not it is in principle possible to improve the performance of a particular STM design. Applying these concepts to a real system, the response will only yield an estimate of the actual performance since other resonances from, e. g., bending motion, which generally lie lower in frequency than for the longitudinal motion, can interfere with the performance of the STM. This is because not only the vertical tip-sample distance is important but also a steady horizontal position of the tip with respect to the sample. Nevertheless, the optimization conditions in Equ. 5.9 give excellent criteria for improving the performance of a particular STM design.

For a real system, it is much more practical to determine the transfer function of an STM design from a set of resonance frequencies obtained from a Computer Aided Design (CAD) model by the Finite Element Method (FEM) [110] than to assign the appropriate masses and spring constants. Therefore, the transfer functions need to be rewritten in terms of the model’s resonance frequencies ω_i :

$$\begin{aligned} G_1(s) &= \frac{1}{(\frac{s^2}{\omega_1^2} + 1)(\frac{s^2}{\omega_2^2} + 1)} - \frac{1}{\frac{s^2}{\omega_3^2} + 1}, \\ G_2(s) &= \frac{1}{\frac{s^2}{\omega_1^2} + 1} - \frac{1}{\frac{s^2}{\omega_2^2} + 1}, \\ G_3(s) &= \frac{1}{(\frac{s^2}{\omega_1^2} + 1)(\frac{s^2}{\omega_2^2} + 1)} - 1. \end{aligned} \quad (5.10)$$

It should be noted that the resonance frequency ω_i is not equal to $\sqrt{k_i/m_i}$ for the coupled oscillators. The optimization conditions in terms of the resonance frequencies are:

$$\begin{aligned} \text{Model 1} &: \omega_3^2 = \frac{\omega_1^2 \omega_2^2}{\omega_1^2 + \omega_2^2}, \\ \text{Model 2} &: \omega_1 = \omega_2. \end{aligned} \quad (5.11)$$

The lowest resonance frequencies of the longitudinal motion obtained by a modal analysis of the FE model of the STMs can then be used to determine the individual ω_i . For model 1, the design of the coarse approach mechanism as well as the scan piezo with the tip will be fairly set in most cases. Therefore, the minimized response could be realized by matching the resonance frequency ω_3 of the outer cylinder to the optimization condition.

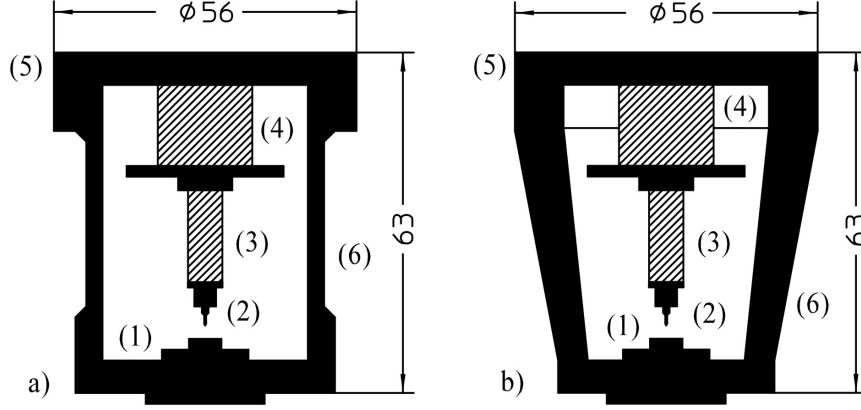


Figure 5.5: Original design (a) and new design (b) of the STM that has been used in the experiments. (1) sample, (2) tip, (3) scan piezo, (4) coarse motion piezo(s), (5) base plate, (6) cylinder/cone to hold the sample. All dimensions are given in mm.

For model 2, probably a combination of design changes for the scan piezo with the tip, the ramp with the sample, as well as the coarse motion piezos are necessary to fulfill the optimization condition in Equ. 5.11.

In order to test these design criteria, an optimized STM design was built according to model 1. A sectional drawing of the original and new STM designs used in the experiments are shown in Fig. 5.5(a) and (b), respectively. For clarity, unnecessary details have been omitted and only the outlines of the piezos are shown. The coarse motion piezo is a commercial z-stage by attocube, the scan piezo is a PZT ceramic tube and the outer cylinder is made of copper. While the original design employs a cylindrical fixture to hold the sample, in the new design this has been changed to a conical shape with different inner and outer slopes in order to increase its resonance frequency.

The resonance frequencies for the coupled oscillators (coarse motion and scan piezos) have been determined by an FEM simulation from a CAD model ($\omega_1 = 15.467$ kHz and $\omega_2 = 23.681$ kHz). The resonance frequency of the original design for the outer cylinder was $\omega_3 = 7.683$ kHz and for the optimized design it would be $\omega_3^{\text{opt}} = 12.949$ kHz. The magnitude of the transfer functions for the different designs are shown in Fig. 5.6. In the low frequency range, the transfer function of the optimized design (dash-dotted line) yields an improvement of about six orders of magnitude compared to the original design (solid line). The actual new design (dashed line) represents a compromise to accommodate spacial constraints in the design, such as some space for the bias voltage contact on the sample. The resulting resonance frequency for this new design according to the FEM simulation was $\omega_3^{\text{new}} = 11.572$ kHz. In order to achieve this, the cylinder holding the sample has been changed to a more conical shape. The resulting improvement in response compared to the original design is about one order of magnitude. This is also already a substantial improvement and it can enhance the performance of the STM.

It is difficult to experimentally verify the improvement in the performance of the STM

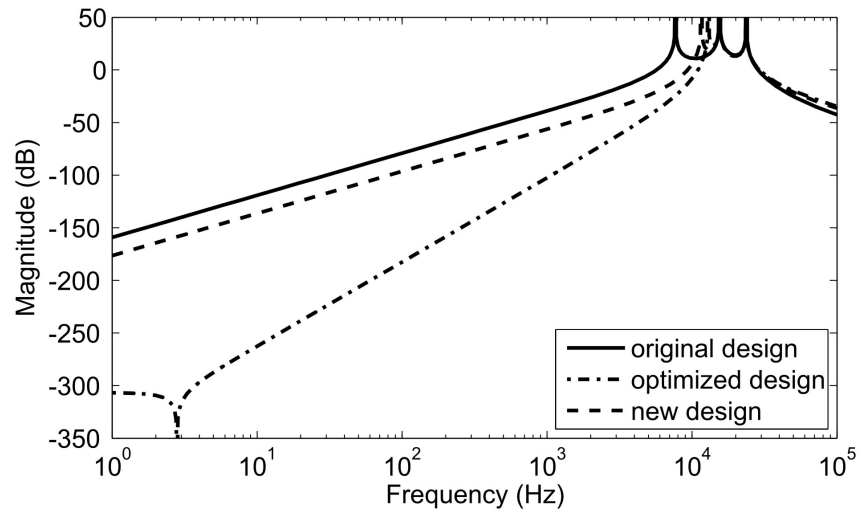


Figure 5.6: Magnitude Bode plot for the original, optimized and new STM designs.

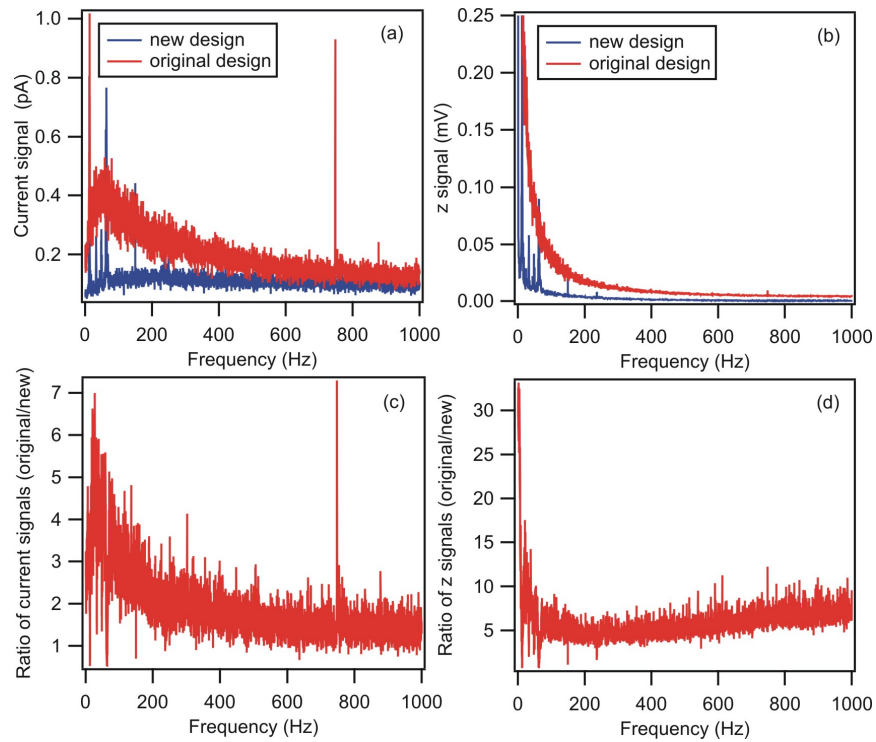


Figure 5.7: Fourier transforms of the tunneling current (a) and the z-signal (b) before (red/light gray) and after (blue/dark gray) the design optimization. The ratio between original and new design is shown for the tunneling current in (c) and for the z-signal in (d).

after the optimization procedure. This is essentially because the tunneling junction between tip and sample strongly depends on the quality of the tip and the sample, which makes it difficult to reproduce the same conditions for the measurements before and after the design optimization. Nevertheless, both, the original and new designs were used for an extended period of time to monitor the performance under different tunneling junctions. The graphs in Fig. 5.7(a) and (b) show the Fourier transforms of the tunneling current and the z-piezo signal measured over time when the tip is resting and the feedback loop is closed. They represent the best results for the STM design before and after the optimization. The red (light gray) and blue (dark gray) curves correspond to the original and the new design, respectively. The measurements were done at room temperature on a clean Ag(111) surface. The tunneling current was $I = 0.1 \text{ nA}$ with a bias voltage of $V_B = 1 \text{ V}$. The feedback loop parameters were also the same for both configurations. Both the current signal and the z-piezo signal clearly show a reduction in amplitude over the whole frequency range. In addition, the noise in the spectrum is also reduced for the new design compared to the original design.

In order to quantify the improvement of the response in the new design, the ratios between original and new design for the current signal and the z-piezo signal are plotted in Fig. 5.7(c) and (d), respectively. For the current signal there is an improvement by a factor between two and five for frequencies lower than 200 Hz. Above 200 Hz the factor lies between 1.5 and 2. For the z-piezo signal the improvement is always better than a factor of five and in the low frequency range it increases up to a factor of about 14. Over all this represents a significant improvement in the performance of the STM. In the real system other kinds of motion such as bending motion contribute to the response of the tip-sample distance to disturbances. As these and other effects have not been considered in our simple one-dimensional model, the improvement in performance is reduced compared to the theoretically predicted value.

The dynamics of the bending motion can be analyzed independently of the longitudinal motion, since only small flexible deformations occur here and the motions are therefore decoupled [111]. Nevertheless, an optimization of the resonance frequencies of the longitudinal motion affects the bending motion as well, because both resonance frequencies of bending and longitudinal motion are a function of the complex geometry of the STM. Thus, a simultaneous optimization of bending and longitudinal motion becomes very complicated, if possible at all.

Similar to the approach for the longitudinal motion a transfer function of the form

$$G_B(s) = \frac{1}{\frac{s^2}{\omega_{1B}^2} + 1} - \frac{1}{\frac{s^2}{\omega_{2B}^2} + 1} \quad (5.12)$$

can be derived for bending motions in model 1 [111], which relates horizontal disturbances in one direction acting at the base plate to horizontal deviations in the same direction of the tip from the sample. The index B denotes the bending motion. Since the STM is rotationally symmetric, the same dynamics applies to the bending motion in the perpendicular horizontal direction. A reduction in response to the bending motion, i. e. by

matching the frequencies ω_{1B} and ω_{2B} in Equ. 5.12, contributes thus more to the stability of the position of the tip rather than to the actual tip-sample distance, which is another important criterion in the performance of the STM. The optimization condition for the bending motion is similar to the optimization condition for G_2 in Eqs. 5.10 and 5.11.

In order to check if by optimizing the longitudinal dynamics the bending motion has been negatively affected, the lowest resonance frequencies of the bending motion of the tip assembly and the sample have been calculated for the new STM design (model 1) by FEM modal analysis as before for the longitudinal motion. The tip assembly (coarse motor, scan piezo, and tip) has a bending resonance at $\omega_{1B} = 2.01$ kHz. This remained untouched by the optimization process. The bending resonance for the original design for the sample (outer cylinder and sample) was at $\omega_{2B} = 1.76$ kHz, while for the new design it was at $\omega_{2B}^{\text{new}} = 2.386$ kHz. As noted above, it is extremely difficult to satisfy both optimization criteria for the bending motion and for the longitudinal motion at the same time. Nevertheless, the bending resonances in the new design are positioned such that the response is effectively the same. However, it should be noted that further extending the attocube coarse motion piezo results in a slightly lower bending resonance, which in turn results in a slightly worse response in the bending motion for the new design.

The simple one-dimensional model presented above is used to calculate the response of the tip-sample distance in an STM to disturbances. It is possible to significantly reduce this response by demanding that the tip and the sample react with the same amplitude and phase. The transfer functions for three different STM designs have been derived to find straightforward optimization conditions for design improvements. Using FEM analysis to find the corresponding resonance frequencies the optimization criteria can be directly incorporated into the design process of a new STM. The experimental implementation demonstrated that even though a very simple approach for the derivation of the optimization conditions was used, a noticeable improvement in performance is achievable in the actual STM as well. The new design that was developed and tested according to this model was finally used in the following stages of this work.

5.2 STM unit

In this section the design of the the STM unit is described. As mentioned in the introduction it has to be stable to external vibrations, the materials have to be compatible to UHV and cryogenic design considerations have to be taken into account. As the STM is used in high magnetic fields, the whole unit has to be made of materials that show no permanent magnetic moment.

The full design of the STM unit is depicted in Fig. 5.8. It consists of three sections: (i) base plate, (ii) outer body and (iii) sample stage. The base plate is machined out of oxygen free copper and will attach to a link structure. This link structure connects the STM to the MC of the DR insert (not shown in the image). For orientational reference of the base plate to the link structure four guiding pins are used that are inserted into the corresponding holes in the link structure support. They are machined from carbonated

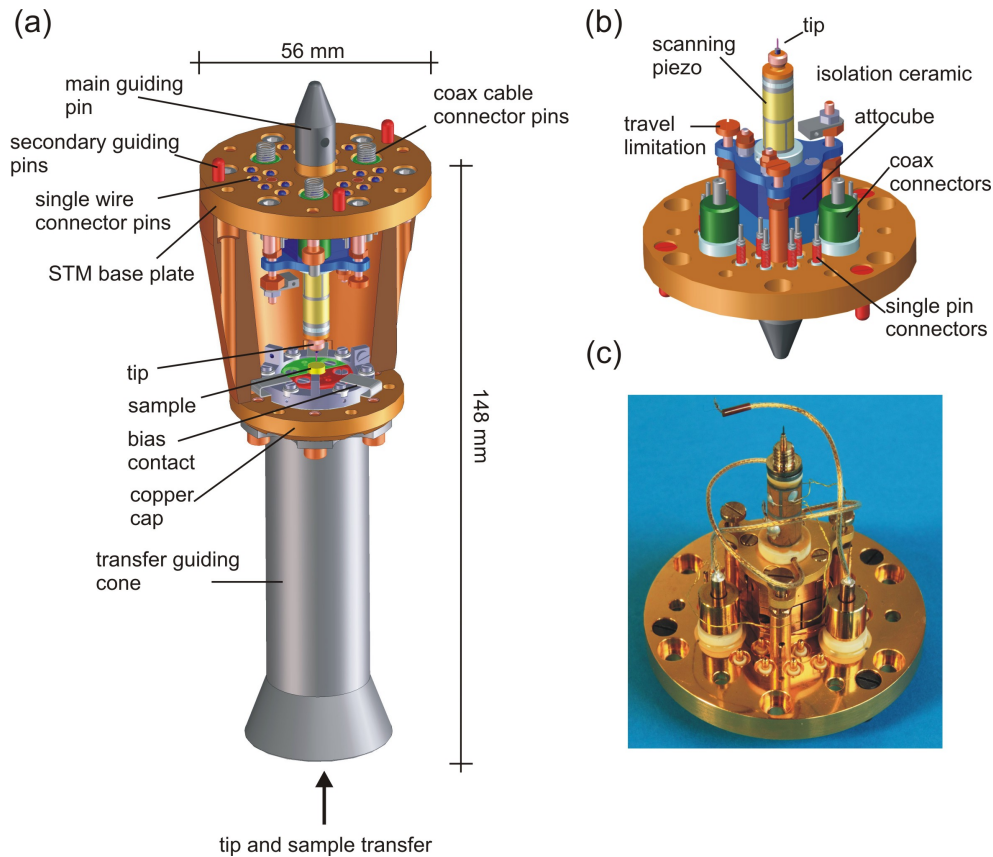


Figure 5.8: STM unit. (a) Full design of the STM unit. (b) View to the interior of the STM unit. (c) Photograph of the STM. See text for details

polyether ether ketone (PEEK) which is a low outgassing high performance organic thermoplastic material. The main guiding pin is used to orient the center of the base plate to the center of the link structure where the three secondary pins define the in-plane orientation. The secondary guiding pins are arranged in a non-symmetric way such that only one well defined orientation to the support structure is possible.

For the electrical connections, 18 spring connectors and three coaxial connectors (MPI design) are embedded into the STM base plate. The pins of the connectors are electrically isolated from the copper plate by Shapal¹ ceramics which is an aluminum nitride ceramic that has higher thermal conductivity compared standard aluminum oxide ceramics. Also sapphire has a high thermal conductivity [54] at low temperatures, but it is more difficult to machine than Shapal.

The coarse motor, which is a commercial stepper motor from attocube, is mounted to the base plate and carries the tip assembly including the scanning piezo (Fig. 5.9). To

¹Shapal M is widely used in vacuum and nuclear industries. It has five times larger thermal conductivity than aluminum oxide. Shapal can be easily machined with standard tools which allows complex shapes of the ceramic parts.

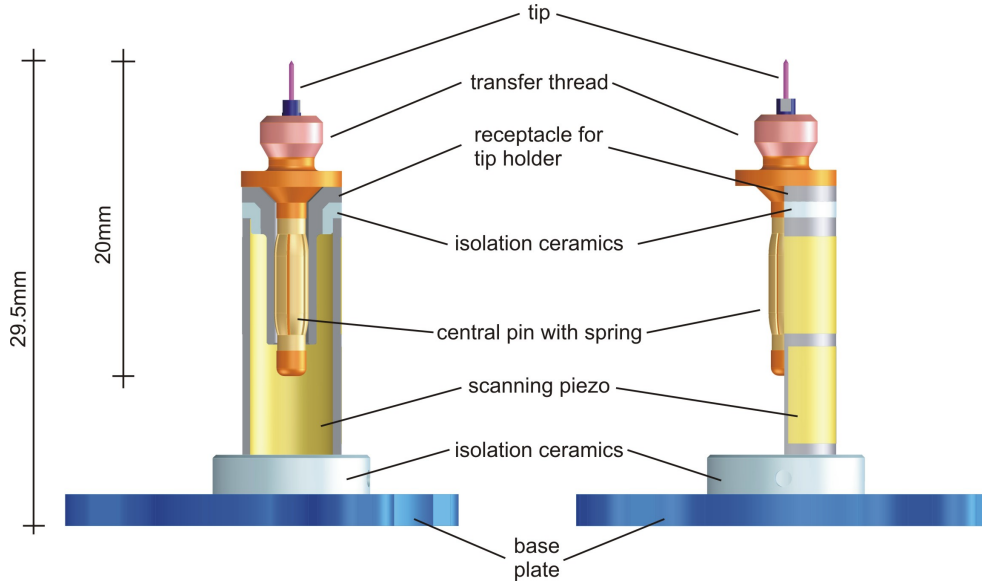


Figure 5.9: Tip assembly. The scanning piezo is attached to the base plate. It carries the receptacle into which the tip holder is inserted. The whole tip assembly is mounted to the attocube coarse motor.

prevent the axis of the attocube from slipping out of the bearing we implemented a travel limitation.

The tip assembly (Fig. 5.9) consists of a base plate to which the scanning piezo is mounted. To isolate the scanning piezo electrically from the base plate, Shapal isolation ceramics are used. On top of the scanning piezo a second isolation ceramics is mounted to which the receptacle for the tip holder is attached.

A rigid copper body connects the base plate with the sample stage and the bias contact (Fig. 5.10). The sample stage consists of a copper cap with an inner thread into which the sample holder is inserted. A copper ring, which is used for the bias contact, attaches to this cap being electrically isolated by a thin layer of Kapton foil. This isolation sheet has a thickness of $25\text{ }\mu\text{m}$. The thinner the isolation is, the more efficient the cooling of the bias contact will be. The contact to the cable is realized by a little clamping screw. Three bias contact clamps out of beryllium copper (Cu98 Be2 , CuBe) attach to the sample holder slightly touching the sample. CuBe is used because it keeps a certain flexibility also at low temperatures.

In Fig. 5.11 the sample holder is depicted. For thermal reasons the base body is machined of silver. We use silicon silver (Ag98 Si2) [112] which is more rigid than coin silver (Ag93.5 Cu6.5) due to the silicon impurities. For sample temperatures near 10 mK , silver has to be used as material for the sample holder because it has a smaller nuclear spin ($I = 1/2$) than copper ($I = 3/2$) giving a smaller contribution to the nuclear part of the heat capacity which cannot be neglected at these temperatures. An isolation ceramics (sapphire) isolates the parts of the sample holder that are on bias potential from those that are on

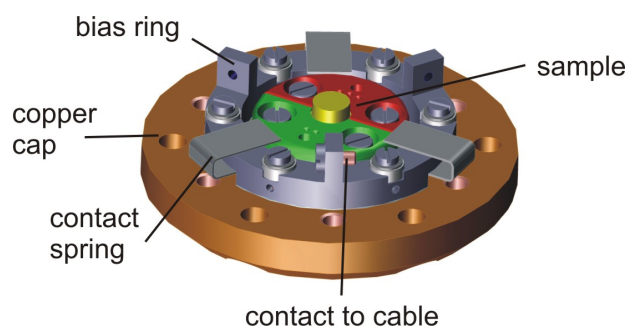


Figure 5.10: Sample stage. The sample holder is screwed into the copper cap. Three contact springs which are mounted to a contact ring are attaching to it. Cables for the electrical connection attach to the contact ring.

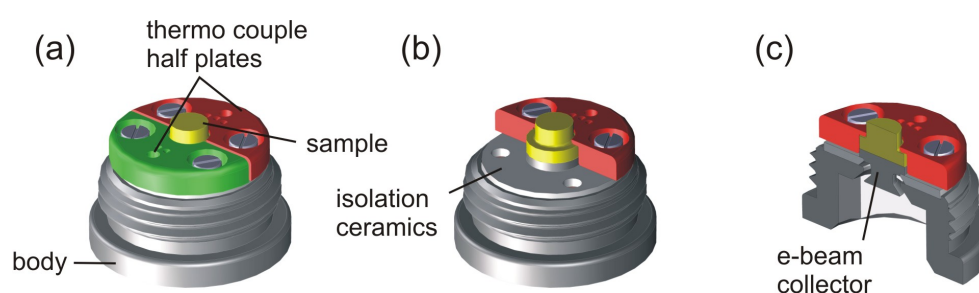


Figure 5.11: Sample holder. The sample holder consists of a base body. An isolation ceramics is used to isolate the sample from the base body. An e-beam collector and the sample are clamped to the base body by two half plates.

ground potential. Sapphire is a ceramic material with very good thermal conductivity at low temperatures like Shapal [54]. As it is more difficult to machine than Shapal, we use it only for simple parts like the isolation ceramic of the sample holder. An electron beam (e-beam) collector which is needed during the preparation cycle is inserted into the central hole of the ceramic. The purpose of the e-beam collector is to make the sample heating more efficient by collecting the electrons closer to the filament. The sample is placed onto this collector. To simplify the design, sample and e-beam collector are clamped to the sample holder by two discs which are machined from type S thermocouple material (Pt/Pt90 Rh10). This avoids additional threads or clamps for attaching thermocouples. During sample preparation, the discs function as thermocouple for temperature monitoring. They have to withstand temperatures up to 1000° C without melting² or alloying to the sample. In addition, they do not become superconducting at base temperature of our cryostat which is necessary for efficient cooling of the sample and have no magnetic moment.

For the tip holder we choose a banana plug design to clamp it into the receptacle at the scanning piezo (Figs. 5.10 and 5.12). A thread in the top part of the tip holder is used for the transfer tool to attach. By this, the tip can be moved in and out of the receptacle. The tip wire is crimped into a little capillary which connects to the center of the tip holder.

All screws in the STM unit are made of silicon aluminum bronze (bronze C64200 also Cu91.2 Al7.0 Si1.8). It is a stiff material which matches the expansion coefficients of copper and silver well [54]. This is important to ensure that connections do not loosen during cool down. Electrically insulating but thermally good conducting epoxy is used for joints involving ceramic parts. For all electrical connections an electrically conducting epoxy is used which has the advantage that one does not have to deal with tin³ [114], lead and corrosive flux at highly sensitive electrical connections.

5.3 Tip and sample transfer mechanism

An important aspect for the daily routine in the lab is a reliable tip and sample transfer mechanism.

A possibility is to transfer the whole STM unit out of the cryostat to realize tip and sample exchange [13,115]. To optimize the thermalization time after a transfer process we only transfer tip and sample. They have much smaller thermal masses than the STM unit which in our case stays permanently attached to the cryostat.

The transfer tool mimics the design of an Allen key (Fig. 5.13 (a)). To the top side of the Allen key a M4 thread is drilled. The Allen key is used to connect to the sample whereas the thread is used to attach to the tip holder. A CuBe spring at the head of the

²The melting point of Pt is 1768° C and for Pt90/Rh10 1830° C. However, even at temperatures lower than the melting point the alloy phase can become instable and Rh starts to segregate out of the Pt [113].

³ Three different phases of tin are known. At room temperature it is in the metallic (β phase). But as temperature is lowered tin starts to undergo a phase transition (10° C to 0° C) to the grey phase (α phase) where it becomes electrical insulating and mechanical brittle. Even lead in standard solder material might prevent the formation of the grey phase in tin, it remains still risky to use solder joints for electrical contacts in low temperature experiments.

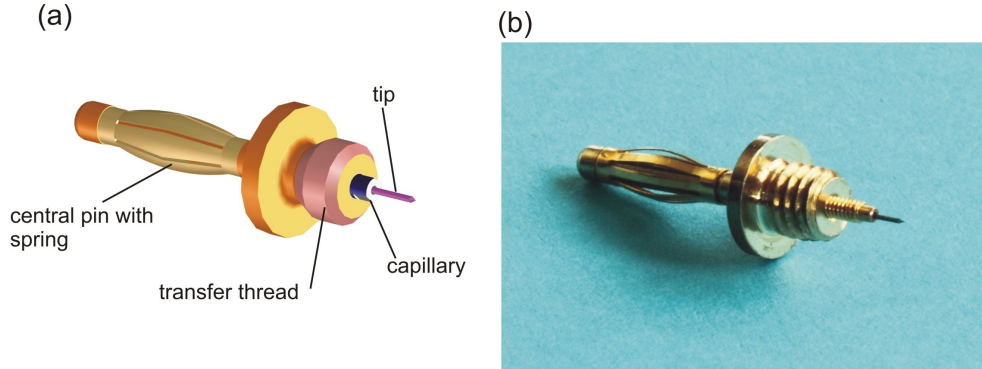


Figure 5.12: Tip holder. The design of the tip holder is based on a banana plug mechanism. A spring is mounted to the central pin. A socket with an outer thread offers a link for the transfer tool. The tip wire is crimped to a little capillary which is inserted into the socket.

transfer tool is used to fix the sample. This avoids that the sample rests loosely on the transfer tool. It is important that the axis of transfer tool, tip and sample are aligned with respect to each other. This ensures a secure pick up of the two by the transfer tool. In our setup we have a travel distance of about a meter which causes easily deviations in the axis alignment. For this reason there are two guiding rings attached to the mechanical axis of the transfer tool which will slide into the guiding cone of the STM unit. Two solid state joints are used to compensate any misalignment of the transfer tool with respect to the axis of the guiding cone. The transfer process is depicted in Fig. 5.13. As the sample blocks the access to the tip, the two have to be transferred serially: first the sample and finally the tip.

The initial configuration is shown in Fig. 5.13 (a). The Allen key of the transfer tool is moved into the sample holder base body and screws it out of the sample stage 5.13 (b). The sample can be stored in a magazine in the preparation chamber. With no sample in the STM head, the access to the tip is given which can be transferred in a second step 5.13 (c). Again, the transfer tool is moved into contact with the tip and the inner thread is used to attach it. The tip needs to be clamped strong enough into the scanning piezo, that it is possible to screw the transfer tool to the tip thread but soft enough that no crucial forces and angular momenta are acting which can break the piezo ceramic. Therefore the clamping strength of the banana spring has to be precisely adjusted to the receptacle in the scanning piezo. Once the transfer tool attaches to the tip, it can be pulled out of the scanning piezo and transferred to the preparation chamber.

5.4 Link structure

The link structure connects the STM unit to the MC of the DR. This structure is an independent unit which extends the wiring of the cryostat to the STM, emphasizing the modular character of our STM design. The length is chosen such, that the sample inside

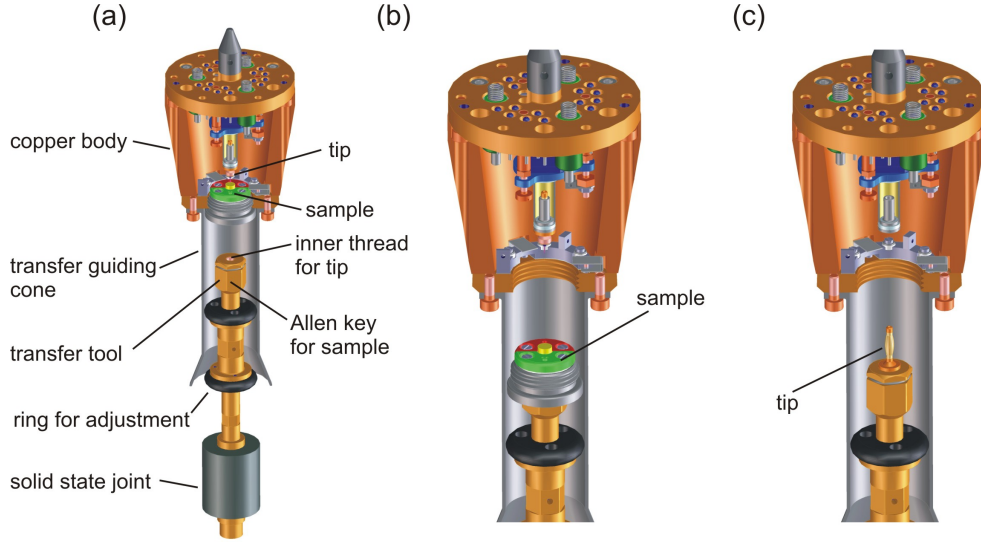


Figure 5.13: Tip sample transfer. (a) The transfer tool is moved into the STM to contact the sample. The sample is screwed out of the sample stage of the STM (b). In a second transfer step (c) the tip is transferred out of the STM. To transfer tip and sample back into the STM these steps have to be followed in reversed sequens.

the STM unit is in the region of maximal magnetic field. The structure consists of a gold plated copper top plate attaching to the mixing chamber and a silver support plate for the STM. Both plates are connected by four rods made of coin silver, a silver alloy which contains 93.5 % silver and 6.5 % copper (Ag935). For good thermalization, every wire that leads from the MC to the STM is attached to heat sink bobbins. These bobbins consist of gold plated copper and are assembled to MC side of the structure. To measure the temperature of the support plate close to the STM, we attached a resistive thermometer (RuO) to it. This give an indication of the STM temperature during measurements.

5.5 Wiring of cryostat and STM

This section deals with the wiring of the cryostat, the link structure and the STM unit. To find the correct choice of wires and cables, one has to include considerations about the signals to be transmitted along the lines and cryogenic design considerations.

Signals, that are sensitive to the coupling of external electric fields need to be transmitted through shielded cables. We use shielded cables for the current, bias and z-electrode of the scanning piezo because these signals are most sensitive. The design is such, that no spot along the total distance of the cables exists, where the shielding is interrupted. The current signal line has to transmit currents which have amplitudes in the order of a few pA. The bias defines the energy at which electrons tunnel. Every disturbance introduces noise which will lead to less defined energies for the tunneling electrons. In addition we

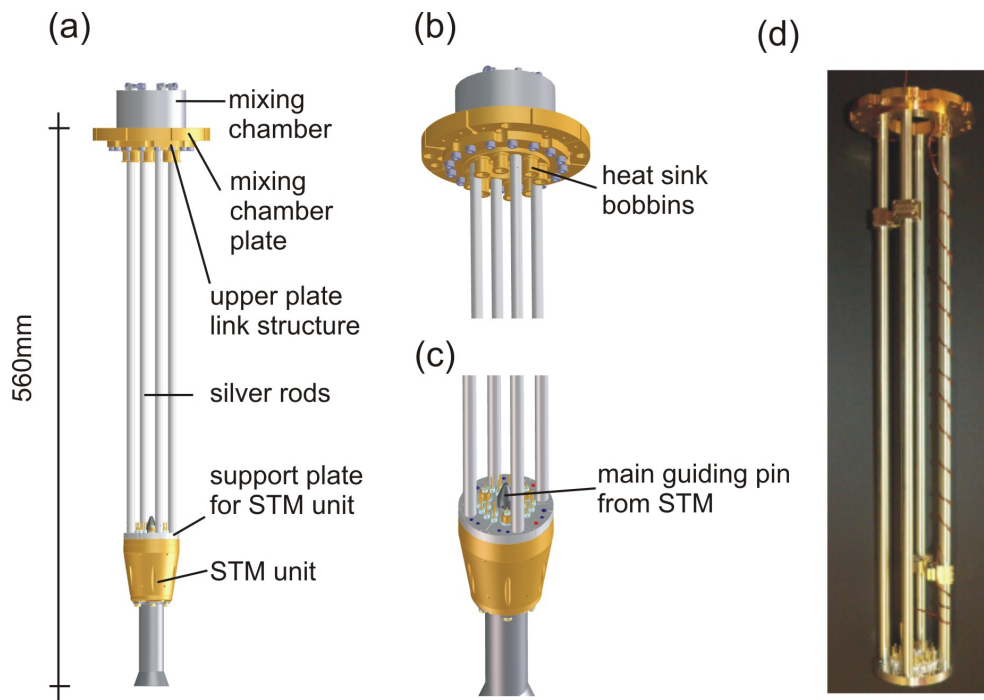


Figure 5.14: Link structure. (a) Overall view of the link structure which connects the STM to the mixing chamber of the DR. The length is adjusted such that the position of the sample coincides with the place of maximal magnetic field. (b) Perspective view to the connection between link structure and mixing chamber plate. (c) Perspective view to the connection between link structure and STM unit. (d) Photograph of the link structure with one semi-rigid cable assembled.

add for spectroscopy measurements a small modulation voltage in the order of $5\mu\text{eV}$ to the applied bias which is also extremely sensitive to electrical noise. Because of the high sensitivity of the tunneling current to the tip sample distance, the z signal has to have a low noise level as well. In this case electrical noise directly influences the distance between tip and sample and therefore acts on the tunneling current as well. Less sensitive signals are those applied to the x and y electrodes of the scanning piezo. Therefore unshielded wires are used.

All cables and wires used in the cryostat are attached to a room temperature feedthrough. They introduce heat to the mixing chamber and need to be carefully thermalized at the different temperature levels of the cryostat. The heat transfer along the wire depends on the thermal conductivity of the wire material which should be as low as possible. On the other hand one needs good thermal contact of the STM unit to mixing chamber because tip and sample should be cooled as effective as possible. These requirements can only be realized if the wiring is separated in different sections:

- Using low thermal conductivity wires and cables from room temperature to the coldest place of the cryostat
- Using high thermal conductivity wires and cables from the mixing chamber to the STM unit.

We use three sections of independent wiring in the cryostat: dilution refrigerator, support structure and STM unit. Every section is connected to an other by a well defined interface, allowing us a high flexibility in the case of maintenance. We can remove a single section for repair leaving the others unaffected.

Wiring of the dilution refrigerator for STM applications

As mentioned in the introduction, the number and choice of wires for a low temperature experiment is always a trade off between thermal considerations and the kind of signals that are transmitted by them. In general, low thermal conductivity wires are preferred for connecting the room temperature feedthrough with the wiring interface mounted to the MC. This minimizes the input of heat to the experiment. Beside this, a coaxial cable will always introduce more heat into the cryostat than a single wire of the same conductor material. The thermal conductivity is related to the electrical conductivity through the Wiedemann-Franz law which states that a low electrical conductivity implies a low thermal conductivity [54]. Higher resistance materials like manganin ($\text{Cu}_{86}\text{Mn}_{12}\text{Ni}_2$) and stainless steel are preferred in low temperature applications in comparison to copper and silver (which have a high thermal conductivity). A second method to avoid thermal conductivity and still benefit from a low wire resistance is the use of superconducting wires. When such wires are cooled below the transition temperature T_C the thermal conductivity is close to zero. The drawback of using superconducting wires is that they prohibit room temperature tests of the parts that are connected to them.

The wires and cables used inside the cryostat are terminated at the mixing chamber. They end in SMA or multi-pin plugs offering a well defined interface to proceed with the

wiring for the support structure. For shielded cables we use stainless steel cables that have a low thermal conductivity. The non-shielded wires are simple manganin wires in twisted pair configuration of which fourteen are terminated on the mixing chamber by an SMA array and twenty-five by a UHV compatible multipin plug.

For the connection of the coarse approach the arrangement is more advanced. To work properly, the motor allows a maximum wire resistance of $10\ \Omega$. The total wire length in our cryostat is about five meters which excludes the use of manganin wires because the overall resistance would be too high. The solution is the use of copper wires from room temperature to the 1K-pot temperature level and from 1K-pot proceeding with superconducting wires to the MC. This results in a total wire resistance smaller than $10\ \Omega$ but requires the cryostat to be at temperatures below 4 K in order to use the coarse motor.

Wiring of link structure and STM unit

The main guideline for the wiring of the link structure is to have good thermal conductivity. For the three shielded cables we change to copper semi-rigid cables where the unshielded wires are polyimide insulated silver wires. The polyimide insulation has low outgassing characteristics and can be used in UHV without concerns. All cables are attached to the mixing chamber by SMA connectors or a multi-pin plug. At the STM support plate of the link structure we use a home made design for the plugs. Care was taken to avoid any ferromagnetic materials⁴.

We have included three floating coaxial connections for the signals of current, bias and the z electrode of the scanning piezo into the base plate of the STM. Eighteen single wire connections are used for the in-plane electrodes of the scanning piezo, the coarse motor and for additional thermometers. For the STM unit itself we also use cables and wires with good thermal conductivity. Gold plated shielded copper cables are used for the signals of tip, bias and z and polyimide isolated silver wires for contacting the scanning piezo and the attocube.

5.6 UHV system

The advantage of the scanning tunneling microscopy system presented here is the *in situ* sample preparation capability. The samples can be transferred from the UHV preparation system into the cryostat without breaking the vacuum. The chamber has a compact and flexible design allowing standard UHV preparation procedures like sample sputtering, sample annealing and UHV cleaving. The UHV system (Fig. 5.15) is directly connected to the cryostat and consists of different sections: The main section (1), the manipulator section (8), the vacuum handling section (11) and the load-lock section (16). The main

⁴ Normally gold plated connector pin have a nickel adhesive layer underneath the gold. This prevents gold diffusing into the pin material

section (1) is the center of the UHV system. Samples and tips are transferred from here into the STM and vice versa by means of a magnetically coupled transfer mechanism (2). To reduce the time of thermalization after a transfer process it is possible to pre-cool the samples in a liquid nitrogen heat exchanger (3). An argon ion bombardment system (4) for sample cleaning as well as a metal evaporator (5) are included. A sample (6) and a tip magazine (7) allow the storage of up to three samples and tips.

The sample preparation section (8) is connected to the main section. This part contains the manipulator which includes the sample heating stage (9). For evaporating atoms or molecules on a cold surface the manipulator includes a flow cryostat which can be used for cooling the sample to temperatures of about 20 K. In addition, an *in situ* cleaving mechanism (10) is implemented.

The vacuum handling section (11) contains mainly parts for pressure monitoring and vacuum controlling. The main turbo pump (12) is used to pump the chamber to a pressure in the low 10^{-10} mbar range. To avoid disturbances during STM measurements this pump can be disconnected from the remaining vacuum system by a gate valve. This has the advantage that the turbo pump can be shut off, reducing the vibrations to the UHV chamber and the cryostat. In this configuration the chamber is only pumped by the ion pump (13). During sample preparation or leak search it is necessary to measure the composition of the residual gas in the vacuum by a residual gas analyzer (RGA) (14). To decrease the pressure in the UHV system further, titanium is evaporated on a daily base by use of a sublimation pump (TSP)(15).

The last section of the UHV system is the load-lock (16). This is a small chamber separated from the main chamber by a gate valve. It is independently pumped (18) by a small turbo pump (18) used to load and unload samples in and out of the main section through a transfer manipulator (17). The load-lock chamber can be vented to air while maintaining UHV in the rest of the vacuum system.

5.7 Vibration isolation system

As our STM is rigidly connected to the cryostat, it is necessary to mechanically decouple it against external disturbances and noise from the building. These disturbances can originate from different sources. First of all the building itself vibrates with frequencies that are normally placed in a range of 2 Hz-20 Hz. Beside this, vibration sources in neighboring labs especially pumps can transmit their noise through the floor. An other source of mechanical disturbances originate from the pumping lines used for the cryostat operation.

The complete isolation scheme of our setup is depicted in Fig. 5.16. Our setup extends over two building levels, but it is only connected to the floor of the upper lab. This avoids the use of two separate damping systems. Using two damping systems on each floor can introduce unwanted coupling between them caused by the relative motion of both floors. The isolation of the cryostat from the floor can be accomplished by a combined use of active and passive vibration isolators. The passive isolators (green color code) are effective through the whole frequency range of interest (1 to 1000 Hz) but they have a resonance

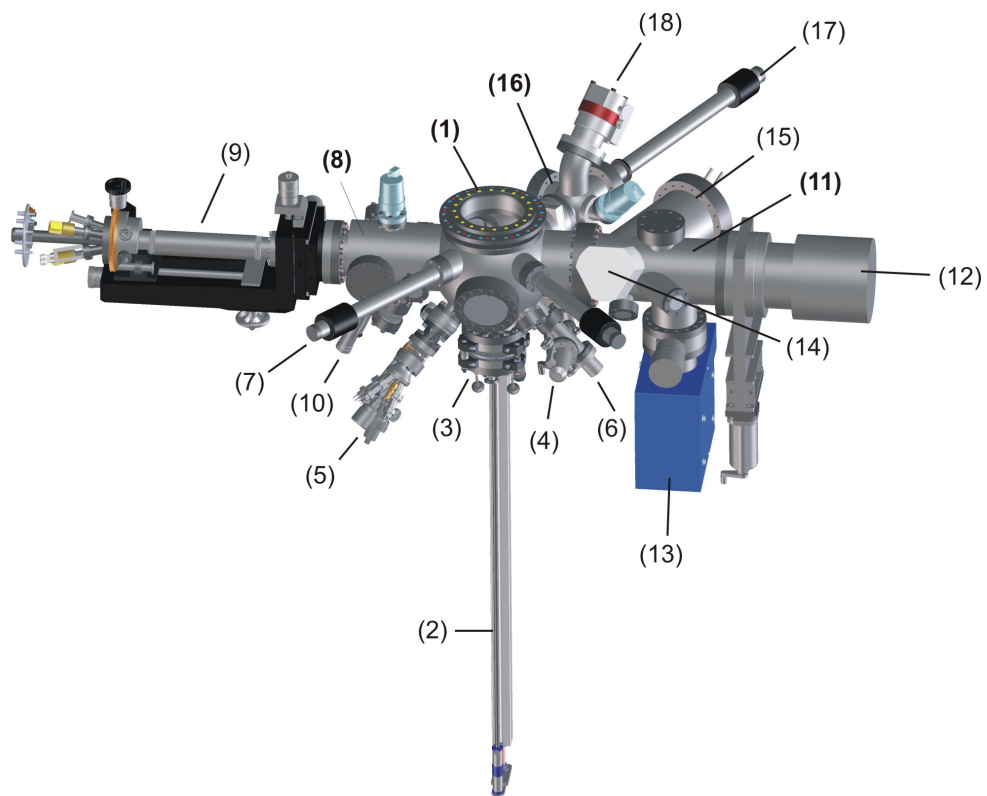


Figure 5.15: UHV system for sample preparation. See text for explanation.

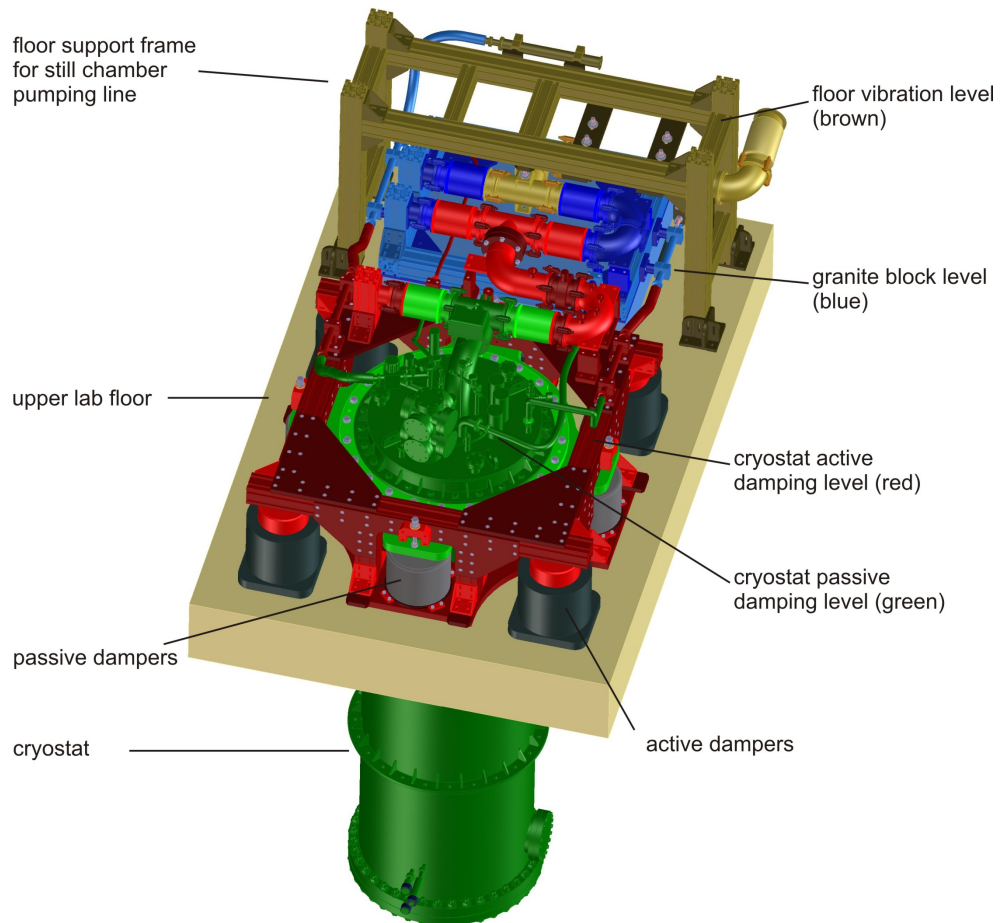


Figure 5.16: Schematic of different damping levels. For damping the cryostat a combined setup of active controlled and passive dampers are used. Vibrations transmitted through the pumping lines are eliminated by attaching the lines to a heavy mass, in our case the granite block. For the still chamber pumping line soft bellow segments are used to reduce the coupling among the various stages.

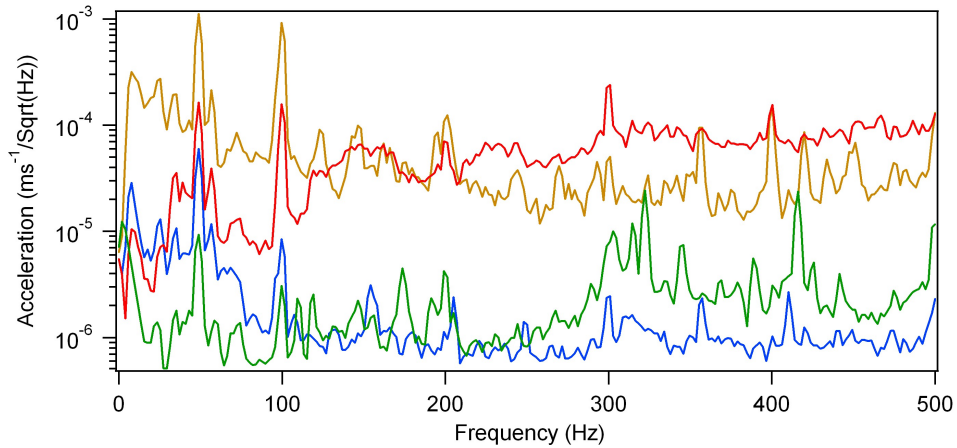


Figure 5.17: Fourier transformation of the vertical acceleration level of the different vibration stages. The image shows the floor level (yellow), granite block level (blue), active level (red) and the passive level (green).

at 1.6 Hz [116]. They consist of a piston which floats on an air volume [116] allowing a laminar air flow through the housing. This results in a damping effect of the piston level. To avoid any excitation at the resonance frequency, they are used in combination with active isolators (red color code). The active isolators are efficient in a frequency range from 0.5 Hz to 100 Hz. The combination of active and passive isolation has proven to be successful to block the transmission of vibrations from the floor to the cryostat.

To avoid disturbances from the pumps, we placed them in a separated isolated room. They are assembled in a frame which is mounted through springs to the ceiling of the lab. This avoids a direct connection with the floor level, which supports the cryostat. Every pumping line going to the cryostat consists of flexible hoses which are rigidly connected to the floor (Fig. 5.16 brown color code). Before they attach to the active stage they are anchored on a heavy, actively isolated granite block (blue color code). After leaving the granite block, the lines are supported on the active stage of the cryostat (red color code) until they finally connect to their ports on the passive stage (green color code). The vibrations which are most difficult to handle are those from the still chamber pumping line (see Chap. 4). The still line has a total diameter of 100 mm making it difficult to block the vibrations transmitted along it. We anchored this line on every vibration level mentioned above, but very soft bellows in an opposed configuration are used to decouple the different vibration levels among each other [117]. The opposed configuration is needed to prevent the bellows to collapse under the pressure difference of 1 bar which they experience to the ambient environment. Also vacuum forces are compensated this way which are substantial for lines with large diameter. The acceleration level for all stages, which is a measure of the vibration, is depicted in Fig. 5.17.

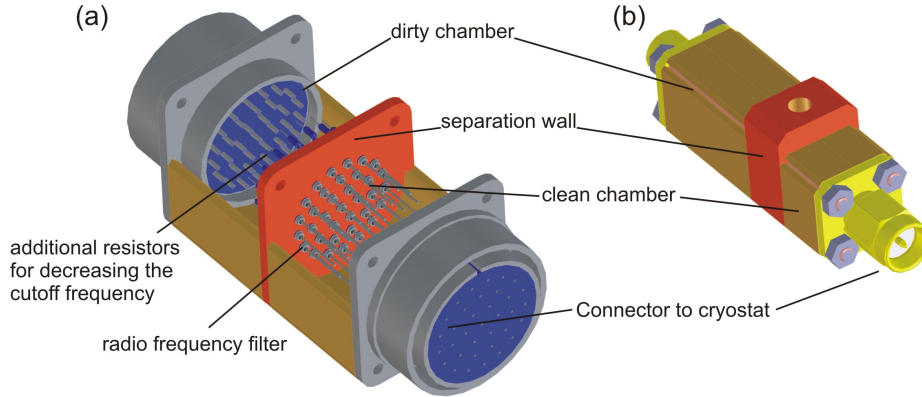


Figure 5.18: Radio frequency filters. Two types of filters are developed: (a) for multipin feedthrough and (b) for SMA feedthroughs. They are used to filter every signal line going into the UHV space of the cryostat.

5.8 Electronics and filtering

To achieve the ultimate spectroscopic resolution of our setup it is important to have as little electrical noise added to the measurement signal as possible. This includes capacitive noise within shielded signal lines, noise from external electromagnetic fields that couple to the wires, radio frequency noise coming from the measurement electronics and the surroundings as well as ground loops between different electrical devices attached to the cryostat. Capacitive coupling from within signal lines occurs, when the inner conductor moves with respect to the outer shield. This induces charge imbalances between both conductors which can be avoided by proper fixing the lines to rigid references (for example to the support structure inside the cryostat or the damping stages outside). The coupling of external electromagnetic fields is suppressed by using shielded cables for the measurement signals. But braided shields do not protect against electromagnetic fields in the GHz region. How to handle radio frequency within the wires, why it is important and how to deal with ground loops is explained for our setup in the following section.

Electronic filtering

What finally defines the electronic resolution limit of a tunneling spectroscopy measurement is the temperature of the electron bath (the electron temperature directly corresponds to the energy resolution) not the temperature measured by a thermometer. A thermometer is attached to a solid object (let it be the sample or the tip holder) and measures the temperature of their solid lattice. It has no access to the temperature of the electron bath near the Fermi energy. The lower the temperature of a conductor is the more are the electrons decoupled from the crystal (the electron phonon coupling between lattice and electrons is very small). This implies that thermal equilibrium between the two is

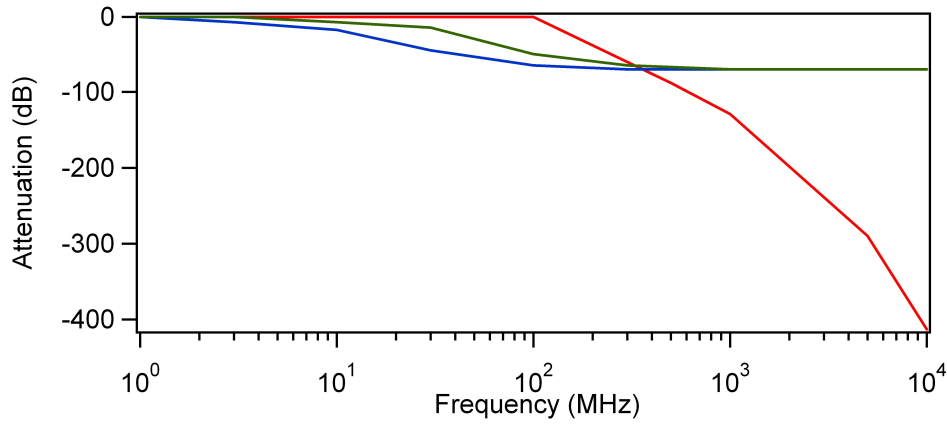


Figure 5.19: Attenuation of our radio frequency filters (blue and green) and the cryogenic coaxial cables (red). From the image one can see that filters and cables are forming combined blockage for high frequency radiation. The cables start to attenuate at that frequency at which the attenuation of the filters saturate.

difficult to achieve at very low temperatures and that the electrons are not as cold as the crystal lattice. As cables and wires are connected to instruments outside the cryostat, they experience a permanent load of radio frequency radiation ranging from several MHz into the GHz region heating up the electrons in the wires. As the cryostat is a closed metal container, it allows radiation only to enter at feedthroughs and flange connections. To prevent this radiation to find a way into the cryostat, we implemented a combined strategy of capping every unused feedthrough and filtering every signal line that goes into the vacuum space of the cryostat. In addition, for the STM current, bias and z connections we use cables that have an intrinsic filtering effect. Two kinds of filters were designed, one for the SMA connectors and one for the multi-pin feedthroughs, which are depicted in Fig 5.18. The design of the filters relies on the two-chamber design where the filterbox is divided into two parts, separated by a metal wall in the middle. Commercially available miniature radio frequency filters are integrated into the metal wall for filtering every signal line. This results in an electrically dirty side of the filter and a side that is clean (which is the one attaching to the feedthrough). The filters used for the piezo connections are specified for high voltages up to 300 V. The frequency response of our radio frequency filters and the coaxial cables for current, bias and z is depicted in Fig. 5.19. One notices that the cables start filtering at the frequency where the radio frequency filters level off.

Grounding strategy

A wrong grounding scheme of the electronics used to acquire the measurement signal results often in unwanted frequency components at 50 Hz and its higher harmonics. The basic philosophy behind eliminating ground loops is to use a single, well defined grounding point to which the ground of all electric devices is attached. Different grounding points

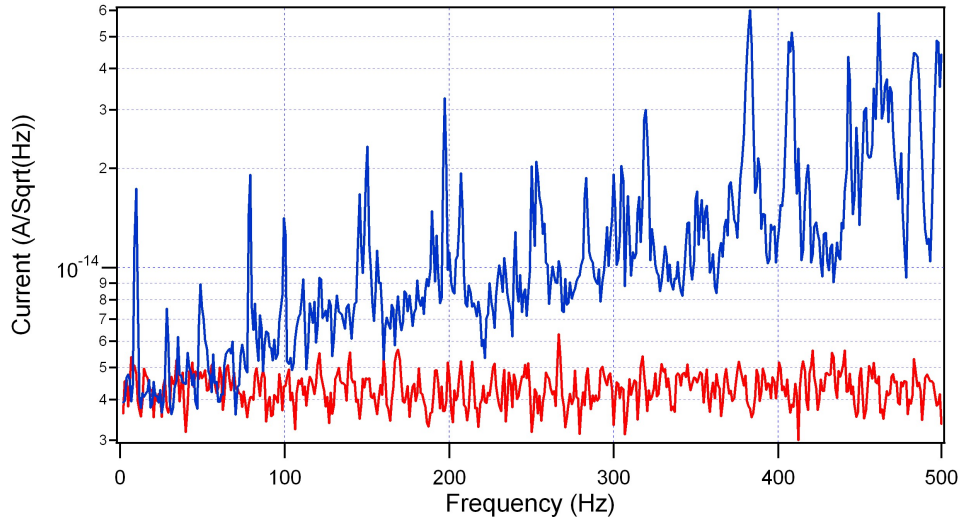


Figure 5.20: Fourier transformation of the current when the tip is not in tunneling contact. The red curve is the Fourier transformation of the current signal from the electronics to the I-V converter. The blue curve shows the Fourier transformation of the current signal including the current cable of the cryostat.

cause potential differences and unwanted current flow in the cable shields. In a first step we divided our system into two different electrical sections: (i) the cryostat including the STM, STM measurement electronics and thermometry and (ii) the preparation chamber including all wires and lines going to the devices attached to it. We isolate the two from each other at the interface UHV flange of the cryostat by using an electrically isolating connector flange. This ensures that the STM, the thermometry and all connections inside the UHV of the cryostat are decoupled from the electronics of the UHV system. In addition, we electrically isolated all pumping lines going to the cryostat to interrupt the connection to the ground potential of the pumps. This results in a cryostat which is totally electrically floating. Now, the cryostat can be used as the central grounding point for our measurement and thermometry electronics applying the star-like grounding arrangement for all devices that are connected to it. This means that the ground for all devices equals only in one point. No additional ground connections between two or more devices are present. The cryostat itself also needs to be connected to a single grounding point (which is in our case the institute ground). This results in a current signal from the I/V-converter which is free from any 50 Hz and higher harmonics (Fig. 5.20). For the measurement of the signal quality of the electronic (red curve) the current connection to the cryostat was detached and the input of the I/V-converter was shielded by a cap. Attaching the current connection (blue curve) results in a more noisy signal which can be attributed to the following reason: the cables might slightly move inside the cryostat which induces noise through internal capacitive coupling between conductor and shield.

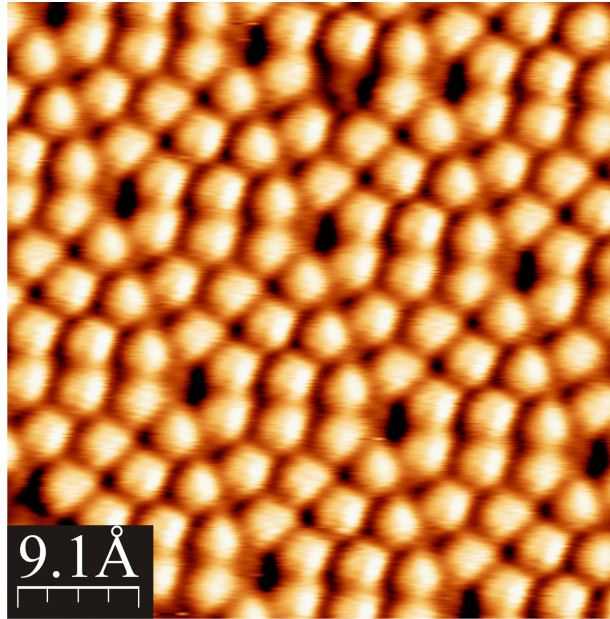


Figure 5.21: Si(111) 7x7 surface measured at room temperature. The room temperature STM was set up for initial testing of the STM unit. The image was taken at a bias voltage of 1 V and a current setpoint of 0.8 nA.

5.9 Tests systems for the STM head

As the STM unit including all techniques for tip/sample transfer and sample preparation is a prototype, careful testing of all components is necessary for a successful operation. Therefore, we assembled two complete test systems including UHV chamber and sample preparation stages. The first test system operates at room temperature and is used for initial tests of the STM unit. The UHV system is equipped with direct current heating stage for preparing semiconductor samples. For first tests we chose the Si(111) 7×7 surface. The results are shown in Fig. 5.21. The image was taken at a bias voltage of 1 V and a current set point of 0.8 nA showing the unoccupied states. Atomic resolution in a good quality is achieved.

For testing the STM at low temperatures we set up a second UHV system. It contains a home-built flow cryostat offering the possibility of temperature dependent STM measurements between 80 K and 300 K. Further, the final sample preparation stage for the mK-STM including the transfer mechanism was implemented into this system. To demonstrate the performance of this system, we measured a Bi surface alloy on Ag(111) as a benchmark experiment [118]. This surface alloy is formed within the first atomic layer of the Ag crystal. The spin degeneracy of the surface state bands is lifted by the Rashba effect which results in two band dispersions shifted about a certain wave vector \vec{k}_0 from the center of the Brillouin zone [119]. As the spins are all oriented in the plane of the surface no net magnetization exists for this system. The band structure results in very prominent

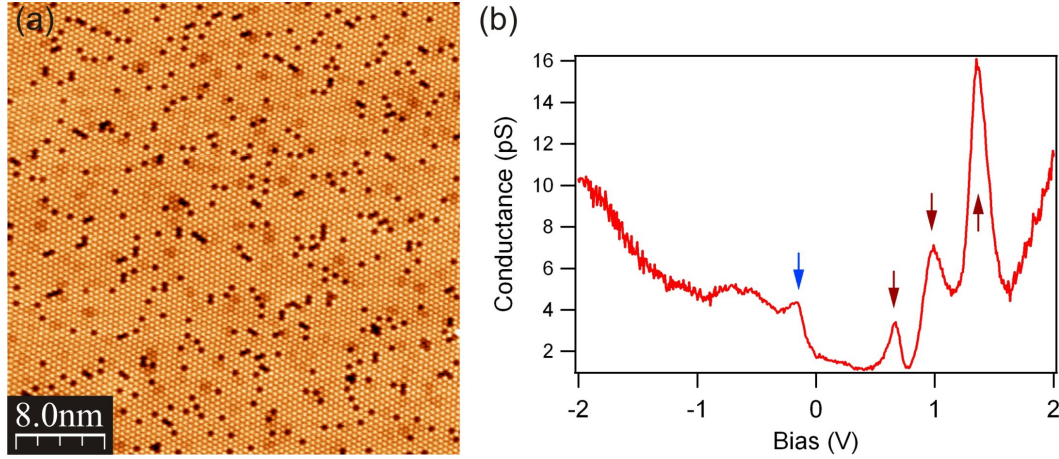


Figure 5.22: Bi surface alloy on Ag(111) measured at 120 K. This STM system was set up for testing the STM unit and the spectroscopy operation at low temperatures. (a) topograph of the surface. (b) representative spectrum taken on a spot in safe distance from an impurity. The band onsets are indicated by arrows. Red for the unoccupied and blue for the occupied states.

features in the local density of states which can be investigated scanning tunneling spectroscopy. For every band one would expect at the position of the energy onset a peak in the differential conductance [120].

A Bi/Ag(111) surface alloy was prepared by evaporating 1/3 monolayer Bi onto the silver crystal at a temperature of 570 K. Fig. 5.22 (a) shows an STM topograph of the Bi/Ag(111) surface alloy. Every third silver atom is replaced by a Bi atom forming a $\sqrt{3} \times \sqrt{3}$ reconstruction. The Bi atoms appear as protrusion whereas the silver atoms in between can not be resolved atomically. The dark spots are due to vacancies in the first atomic layer. In Fig. 5.22 (b) a representative spectrum is shown. The onset of the highest occupied band (blue arrow in Fig. 5.22 is at -160 meV which corresponds well with the result of Ast *et al.* [120] and photoemission data [118]. The occupied peaks in the spectrum appear at $+670$ meV, $+990$ meV and $+1.37$ eV. The corresponding bands are described theoretically by Bihlmayer *et al.* [121]. Their calculation corresponds qualitatively well to our STM spectroscopy results.

Chapter 6

Performance of the mK-STM

The first step after assembling the mK-STM in the final configuration is a careful characterization of its performance. The stability in STM topography measurements has to be verified and the electronic resolution needs to be determined.

In section Sec. 6.1 topography measurements and conductance maps at various temperatures are shown demonstrating the stability at different cryostat modi of operation. It shows the capability of the UHV preparation by using metal single crystal samples for STM measurements that where conditioned by cycles of sputtering and annealing. Finally a precise estimation of the stability between tip and sample is given.

In the next section (Sec. 6.2) the temperature is measured directly at tip and sample which is realized by using two pre-calibrated RuO thermometers instead the two. It is important to note that these temperatures give an estimate of the lattice temperatures of the materials used for tip and sample. It does not necessarily correspond to the electronic temperature value for the electronic resolution jet. An experiment to measure the electronic resolution has to be performed within a spectroscopic measurement of spectroscopic features whose broadening is only determined by the temperature of the electron system.

Finally Sec. 6.3 deals with the electronic temperature and the spectroscopic resolution. To determine the two, we use a tunneling measurement between a superconducting tip and a normal conducting sample.

6.1 Mechanical stability

The following measurements are taken in the final mK-setup at various He circulations resulting in different temperatures. They show the capability of the UHV sample preparation. In first topography measurements we focused on the Au(111) surface which is very well characterized. It features a $22 \times \sqrt{3}$ reconstruction resulting in the well-known herringbone pattern and a surface state with an onset at 0.5 eV below the Fermi energy [122]. These features are very well suitable for topographic and spectroscopic characterizations [123–125].

Fig. 6.1 shows a topography image of UHV prepared Au(111) surface measured at 1.5 K.

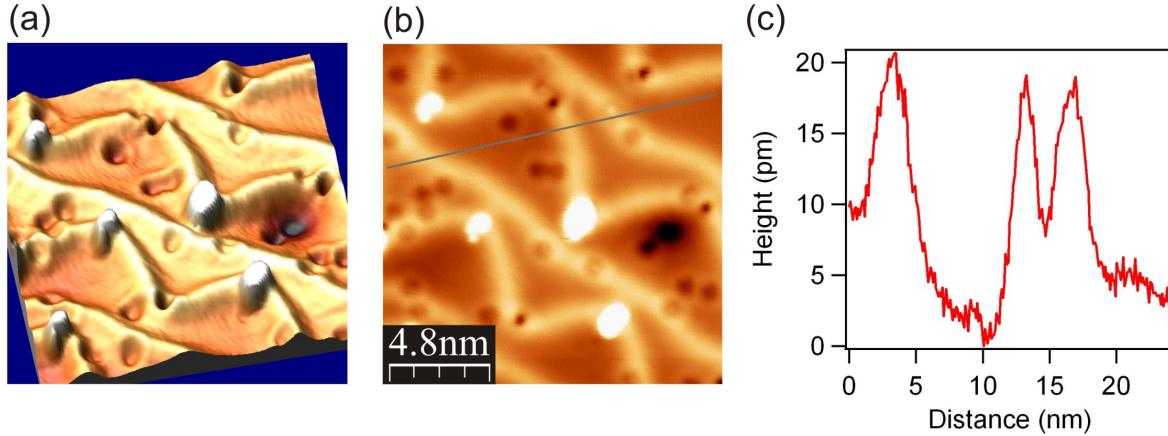


Figure 6.1: STM topograph of a Au(111) surface. (a) three dimensional view, (b) plane topograph and (c) line scan. $V = -100$ mV, $I = 0.5$ nA and $T = 1.5$ K.

At this temperature the STM is only cooled by the 1K-pot of the DR insert. The bright lines of the herringbone pattern separating fcc from hcp packed surface regions are clearly visible [126]. The surface reconstruction itself appears distorted. This can be attributed to strain in the surface. Despite the capability of the UHV preparation we still find defects on the sample most probably due to oxygen or carbon monoxide. The sample can become dirty during the transfer from the preparation chamber when it is inserted into the STM. It warms up the environment desorbing adsorbates from the cold STM body¹. When the STM thermalizes, they adsorb on the STM body again including the sample surface. To get a first estimate of the stability of our STM we analyzed line scans and extracted the peak to peak z noise to be 1 – 1.5 pm. The time per point was $\tau = 5$ ms. During this measurement the control loop of the STM controller was activated.

In Fig. 6.2 conductance maps at a step edge on Au(111) are shown. The same region of the sample was scanned at different bias voltages. A modulation of 5 mV was added for measuring the dI/dV signal by a lock-in amplifier (see Sec. 2.2).

An oscillatory pattern is seen, caused by the interference between scattered surface state waves at the step edge and around impurities. This results in the observation of standing waves in the dI/dV measurement. When the bias voltage is increased, the periodicity of the pattern becomes smaller. Because of the quadratic dependence of the energy on the wave vector of the surface state, an increase in energy results in a higher wave vector which implies a shorter wavelength of the surface state [20, 127].

The next step, the cryostat was cooled to a temperature of 800 mK just by cycling a

¹We have the possibility to bake out the cryostat to temperatures up to 350 K. However, this has to be done after both magnetization thermometers are removed. The paramagnetic salt in the CMN and FPD thermometers is dissolved in an aqueous solution, being in a hermetically sealed container. Heating the thermometers causes evaporation of the solvent inducing too much pressure on the encapsulation. As we are in a stage of the project where we still rely on the magnetization thermometers we decided not to bake out the cryostat jet.

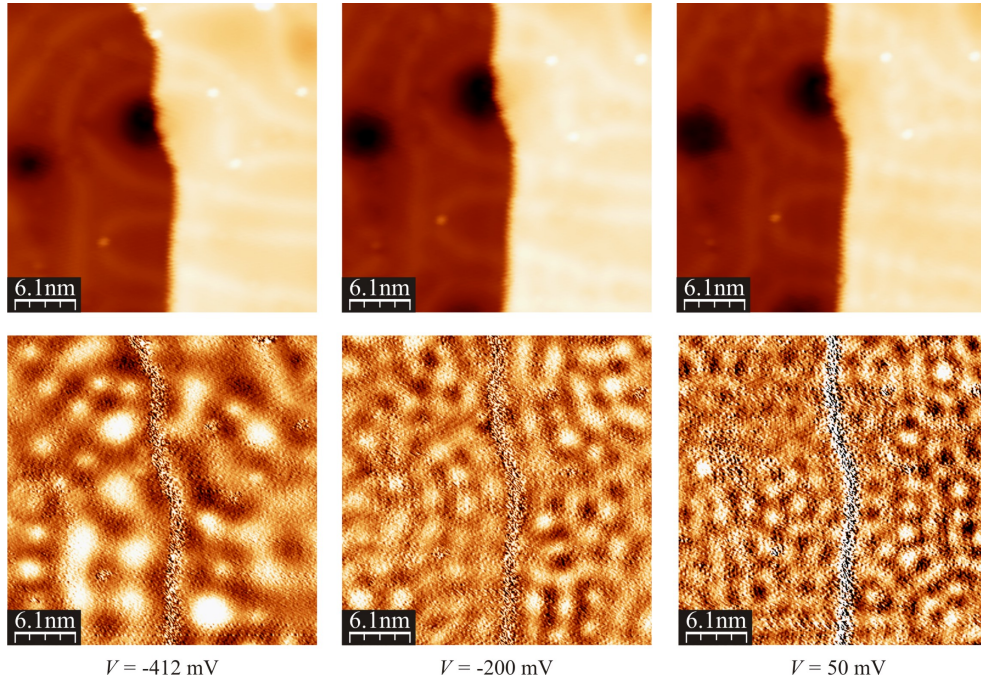


Figure 6.2: Surface state scattered at an Au(111) step edge and impurities. The STM topographic images and dI/dV signals are shown for three representative bias voltages. As the bias voltage (i.e. the energy) is increased the wavelength of the oscillation pattern in the surface state decreases. $I = 0.5$ nA and $T = 1.5$ K.

small amount of mixture. It condenses at the 1K-pot and only covers the bottom of the mixing chamber. The pumps of the gas handling system will reduce the pressure in the still and mixing chamber resulting in an evaporative cooling process. In Fig. 6.3 (a) a topography image of the Au(111) surface at 800 mK is shown. The stability in z decreased by a factor of two resulting in a noise level of 3 pm which we again extracted from line profiles. The averaging time per point was $\tau = 4.2$ ms. Also here the STM control loop was activated.

Finally measurements at a MC temperature of 15 mK are depicted in Fig. 6.3 (b). The whole mixture is condensed into the mixing chamber. To avoid vibration from the dilution stage, we only have a small amount of ^3He circulating ($33.6 \mu\text{mole/s}$) which evaporates in the Still without external heating power. The image shows standing waves of the Cu(111) surface state scattered at impurities. The noise level is between 4.0 pm and 4.5 pm for $\tau = 3.5$ ms and activated STM control loop.

These noise measurements show the tendency, that the magnitude of the noise level increases the lower the temperature is. The temperature is connected to the amount of mixture, which is circulated in the dilution cycle. When the cryostat has a temperature of 15 mK we find the largest circulation rate, and connected to it the highest noise level. The question of the origin of the increased noise level arises. A source of disturbances can be the 1K-pot. Even if we close the needle valve and prevent the flow of ^4He from the main bath into the pot, it experiences a higher heat load due to circulating ^3He which it has to precool. This can cause a higher boiling rate at higher circulations. We guess that the main contribution comes from the 1K-pot. A hint that strongly supports this scenario is that Song *et al.* do observe less noise in STM measurements when they run their cryostat using the Joule-Thompson mode for precooling ^3He [13].

A more precise stability analysis was done at a temperature of 800 mK as shown in Fig. 6.4. The aim is to perform a statistical analysis of the tunneling current when the STM control loop is deactivated. We have measured the tunneling current for a period of 30 s while the control loop of the STM was switched off. During this experiment the tunneling current is directly influenced by mechanical vibrations transmitted to the STM. It acts as extremely sensitive probe for vibrations. From a statistical analysis the number of events for given current values are extracted. Fitting a gaussian function to the current distribution allows us to extract the full width which is 65 ± 2 pA. In a next step the control loop is closed and the current dependence on the tip sample distance is recorded. Linear fitting of the $I(z)$ curve in the range of 1.0 nA to 1.2 nA gives a conversion factor of 24 ± 1 A/m between current and tip sample distance. The width extracted from the current statistics is converted into a distance yielding 2.7 ± 0.1 pm z stability in a frequency range $f \approx 0.03 - 25$ Hz. The given frequency range was estimated from the total time of the measurement and the sampling period of the electronics by using the Nyquist criterion, which states that the noise can be correctly sampled up to a frequency of half the inverse sampling time. Since the integration time for each measured point was short compared to the sampling interval, noise contributions coming from signal components that have higher frequencies than the upper frequency calculated from the Nyquist criterion also contribute to the measured noise. Strictly speaking, the bandwidth of the noise will be larger than

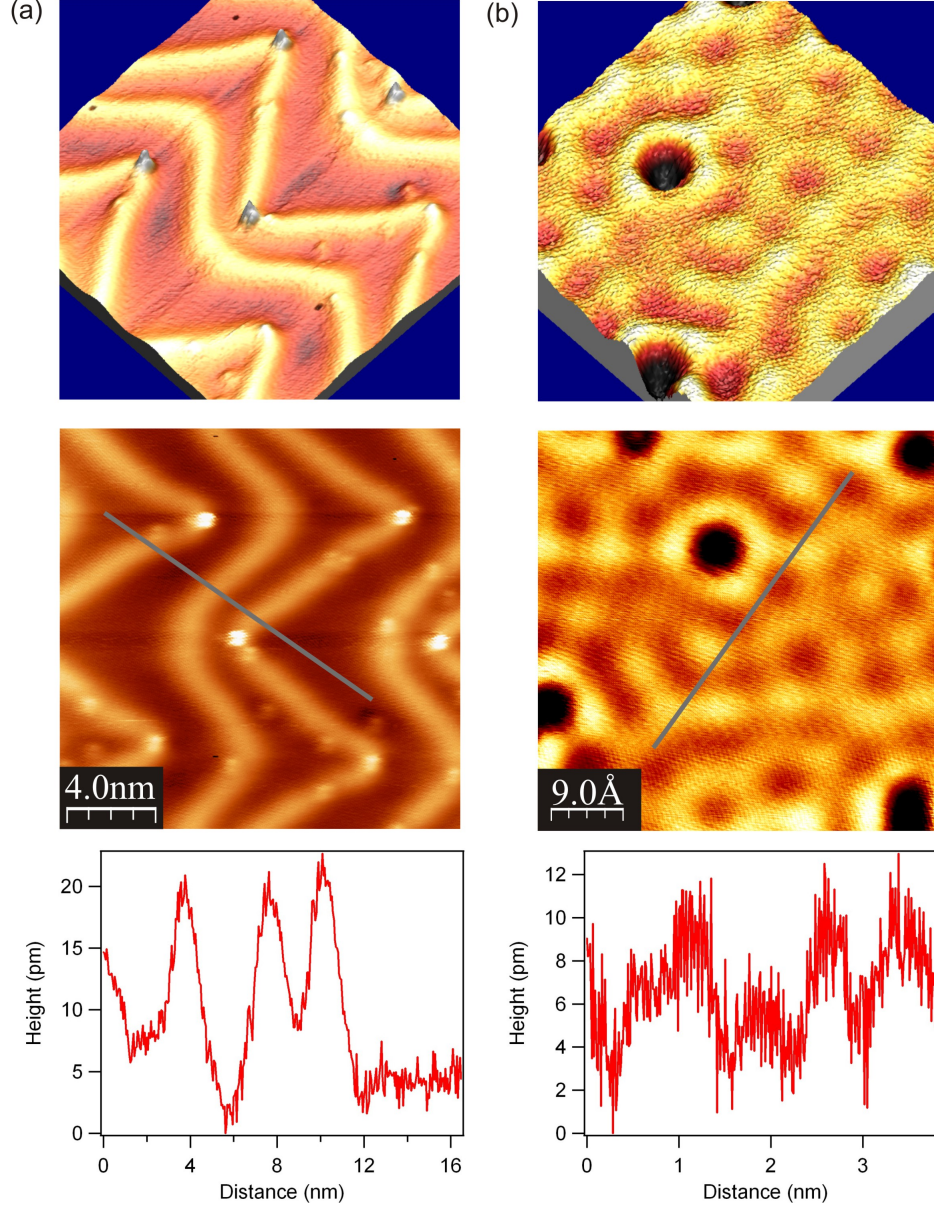


Figure 6.3: Topography image of the Au(111) and Cu(111) surfaces. (a) Topography image of Au(111) measured at $T = 800$ mK. $V = -1$ V, $I = 1$ nA. (b) Topography image of Cu(111) with standing wave pattern of the scattered surface state measured at 15 mK. $V = 50$ mV, $I = 5$ pA.

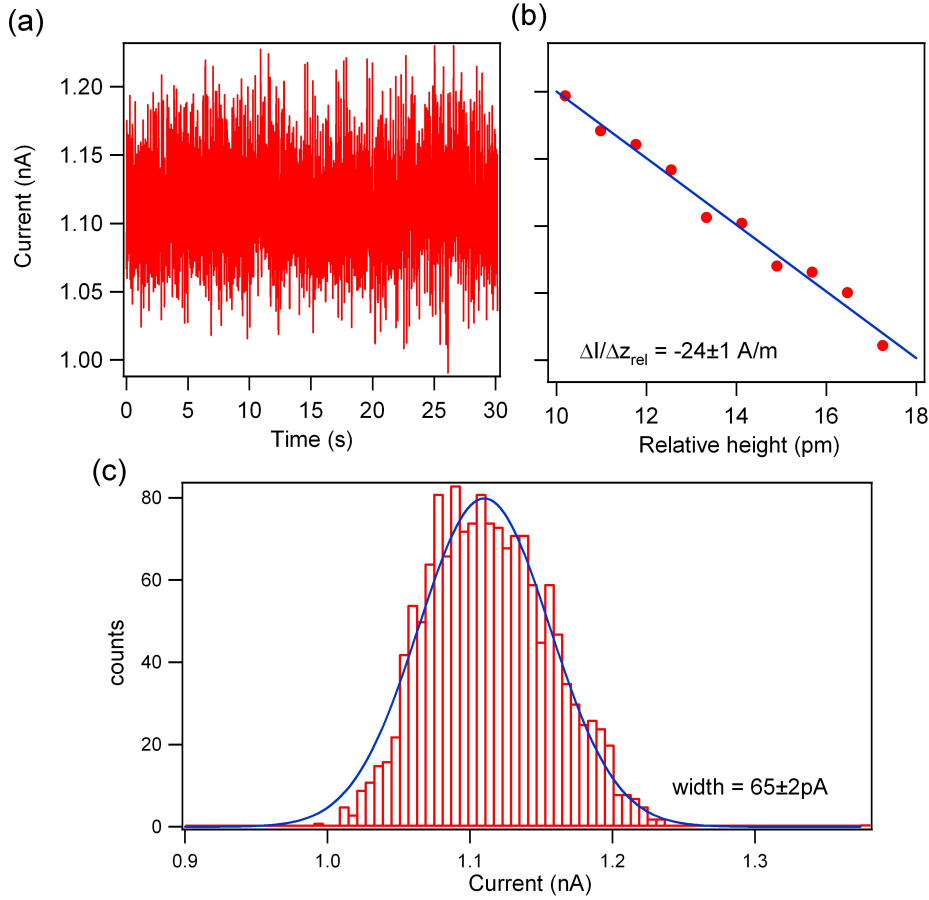


Figure 6.4: Analysis of the stability between tip and sample at $T = 800 \text{ mK}$. (a) The tunneling current is recorded without activated STM feedback loop. (b) In a second experiment the conversion factor between current and relative tip height is measured. (c) The conversion factor is used to related the full width of the current distribution to a distance value. This gives the stability of the tip sample distance.

the estimated value.

6.2 Temperature at tip and sample

To get an estimate of the temperature of tip and sample under realistic operation conditions, we assembled two pre-calibrated RuO thermometers into sample and tip holder. During this measurement the ^3He circulation of the cryostat was adjusted such, that the flow is $43 \mu\text{mole/s}$ which corresponds to the flow rate at which the curve in Fig. 4.15 was recorded. Having a temperature at the MC of 15 mK we find 17 mK at the tip and 20 mK at the sample (Fig. 6.5). It is further interesting to use this configuration for characterizing the temperature evolution during a simulated scan. For this purpose we applied a sine

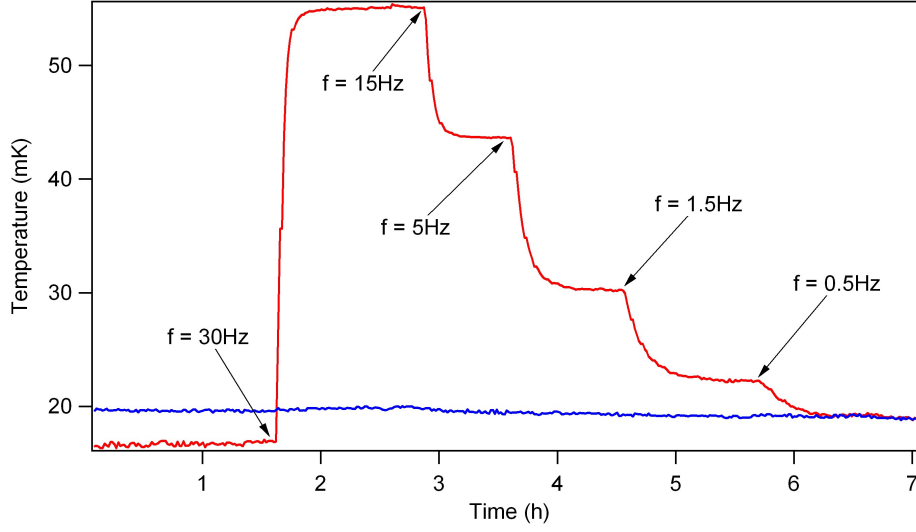


Figure 6.5: Temperature directly measured at tip and sample. Two precalibrated RuO thermometer were placed directly at tip and sample position. The warm up behavior was measured while a sine voltage $V_{PP} = 5$ V to the scanning piezo simulates a measurement process. The blue graph shows the sample temperature. The red graph shows the tip temperature.

voltage to the z electrode of the scanning piezo. The peak to peak value was 5 V which corresponds to a displacement of 2 nm at base temperature. Starting from a frequency of 30 Hz we observed an increase in the temperature of the tip thermometer to about 55 mK. This can be attributed to the heat which is released from the scanning piezo. Decreasing the frequency in steps to 0.5 Hz results in a stepwise cooling of the tip thermometer. The sample temperature stays constant during this experiment indicating that the heat from the piezo does not affect the sample.

6.3 Electronic resolution

The final estimation of the effective temperature (T_{eff}) has to be done in an experiment where a spectroscopic feature is measured, whose electronic broadening is essentially defined by the temperature. A suitable physical system for such a measurement is a superconductor. We therefore, perform tunneling spectroscopy measurements between a superconducting tip and a normal conducting sample. Our measurements are performed at MC temperatures of 15 mK. If this is well below the T_C of the tip material to be used, we can assume that the majority of electrons in the tip are condensed in the BCS ground state, yielding in temperature independent δ -like features at $\pm\Delta$. The formula to describe conductance spectra between a superconducting tip and a normal conducting sample is given in Chap. 3 by Equ. 3.9. Including a scaling factor ρ_0 and a conductance offset into

Equ. 3.9 gives the final fitting formula

$$\frac{dI}{dV} = \rho_0 \int_{-\infty}^{\infty} \rho_t(E) f'_s(E - eV) dE + \text{Offset}. \quad (6.1)$$

For a suitable superconducting tip material to determine the effective temperature the following restriction apply. The gap which is measured should be as close as possible to the theoretical BCS gap. The assumption that only the temperature is responsible for the broadening implies that intrinsic broadening effects are small and do not play a role. This means Γ in Equ. 3.8 is close to zero which implies a quasi-particle excitation gap that does not depend on the lattice orientation. The latter aspect is justified by the fact, that we have a nano sized cluster at the apex of the tip. This can be considered as a point-like probe which does not favor a orientational direction.

Also superconductivity arising from multiple bands at the Fermi surface of a material like it is discussed for NbS_2 , NbSe_2 and other layered superconducting systems has to be excluded [128–130]. Among the known superconducting compounds the only materials of interest for our characterization are type I superconductors. They can be described by the microscopic theory of Bardeen, Cooper and Schrieffer (BCS) [2, 131]. Including the aspects mentioned above, we choose Al as tip material [132]. It is a well characterized superconducting material showing a small anisotropy of the superconducting gap [10]. Aluminum has a theoretical critical temperature of $T_C = 1.2 \text{ K}$ resulting in energy positions for the quasi particle excitation peaks of $\pm\Delta(T = 0 \text{ K}) = \pm 1.764 k_B T = \pm 182.4 \mu\text{eV}$ at zero temperature.

We prepare our Al tips from 0.25 mm high purity Al wire by simply cutting it under ambient conditions. The tips are transferred into the vacuum chamber where the oxide layer is removed by Ar ion sputtering without further annealing. Tunneling measurements where performed on a Cu(111) surface which was cleaned by cycles of Ar ion sputtering and annealing. Tip and sample are transferred into the STM and the electronic behavior is verified by taking I-V curves over a voltage range for -1 V to 1 V. This procedure shows if the tip is conducting and no further oxide remains at the apex. After the transfer the cryostat runs at a temperature of 800 mK. Already at this temperature a small superconducting energy gap is expected for the Al tip. If this gap is observed, we condense the remaining mixture cooling the cryostat to 15 mK.

Two representative measurements at 15 mK are shown in Fig. 6.6. In both spectra the quasi-particle excitation peaks are clearly visible resulting in sharp features in the conductance. They appear at the edges of the excitation gap in the occupied and unoccupied states. From the fit to Equ. 6.1 we can extract the Δ -value and the effective temperature T_{eff} . The effective temperature is directly related to the thermal part of the electronic resolution $\Delta E = 3.5 k_B T_{\text{eff}}$ as shown by Equ. 2.16. The results from the fitting routine are summarized in Tab. 6.1. Our Δ -values are a bit smaller than the theoretical value given above. The reason for this deviation can be attributed to the fact that we have a superconducting tip with a small cluster at the apex. We have only limited control of the atomic arrangement at the end of the tip. However, deviations of the superconducting properties in small clusters compared to bulk are quite normal [133]. Beside this size effects, also

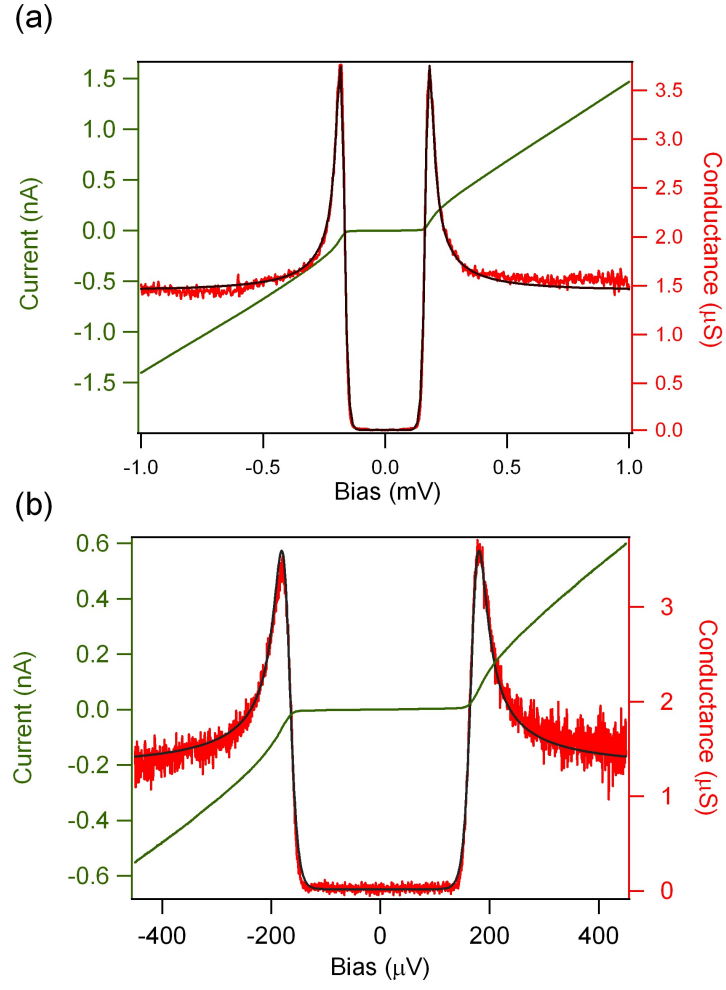


Figure 6.6: Superconducting gap of Al for estimating the electronic resolution. Both spectra are measured with an aluminum tip on a Cu(111) surface at a temperature of 15 mK at the MC of the cryostat. (a) Stabilization of the tip at $V = 2.6$ mV, $I = 4$ nA. (b) Stabilization of the tip at $V = 2.6$ mV $I = 3.9$ nA.

Value	Spectrum (a)	Spectrum (b)
Δ	$172 \pm 8 \mu\text{eV}$	$171.65 \pm 0.002 \mu\text{eV}$
T_{eff}	$97 \pm 3 \text{ mK}$	$87 \pm 3 \text{ mK}$
$\Delta E = 3.5k_B T_{\text{eff}}$	$29 \pm 1 \mu\text{eV}$	$26 \pm 1 \mu\text{eV}$
Γ	$< 0.3 \mu\text{eV}$	$< 0.02 \mu\text{eV}$

Table 6.1: Extracted quasi-particle excitation gap and effective temperature for the two aluminum gaps in Fig. 6.6.

impurities in the tip are affecting the the superconductivity which can lead to different gap sizes as well.

When performing these measurements, care must be taken not to crash the Al-tip into the Cu sample. A tip crash modifies not only the atomic arrangement at the apex of the tip but it also attaches a copper cluster to it. In Fig 6.7 an Al gap is shown after a serious tip crash. What mostly strikes out are the modifications of the gap edges which become round compared to the spectra shown in Fig. 6.6. The quasi-particle excitation peaks do not change that dramatically. This means, the gap is filled with additional states. Fitting these kind of spectra to Equ. 6.1 gives no satisfactory results. These gap shapes can be explained with the theory developed by Blonder, Tinkham and Klapwijk (BTK) which describes the filling of the gap [45] on the microscopic basis of Andreev reflections [43]. The theory is based on the influence of the coupling between a superconductor and a normal metal. The coupling can be tuned by a gap parameter Z which can be related to the normal state transmission of an energy barrier according to $(1 + Z^2)^{-1}$. Larger Z ($Z > 10$) means less influence of a normal metal onto the superconductor whereas $Z = 0$ direct contact defines. An enhanced probability for Andreev scattering is observed in the case of larger coupling. Assuming, we attach a normal metal cluster to our superconducting tip (what happens after a tip crash) we can model the spectrum by fitting it in two steps. First we use the a thermally broadened BCS density of states (Equ. 6.1) such that the fit shows good agreement for the quasi-particle excitation peaks. This fit is used to extract the effective temperature of the electrons. In a second step this temperature is used in the BTK model. We tune the Z parameter until it shows good agreement for the shape of the energy gap. For the spectrum in Fig. 6.7 we can extract an effective temperature $T_{\text{eff}} = 130 \text{ mK}$ and $Z=1.9$. These results indicate, that we are able to model an STM tip to which a normal metal cluster is attached by the amount of coupling between the two.

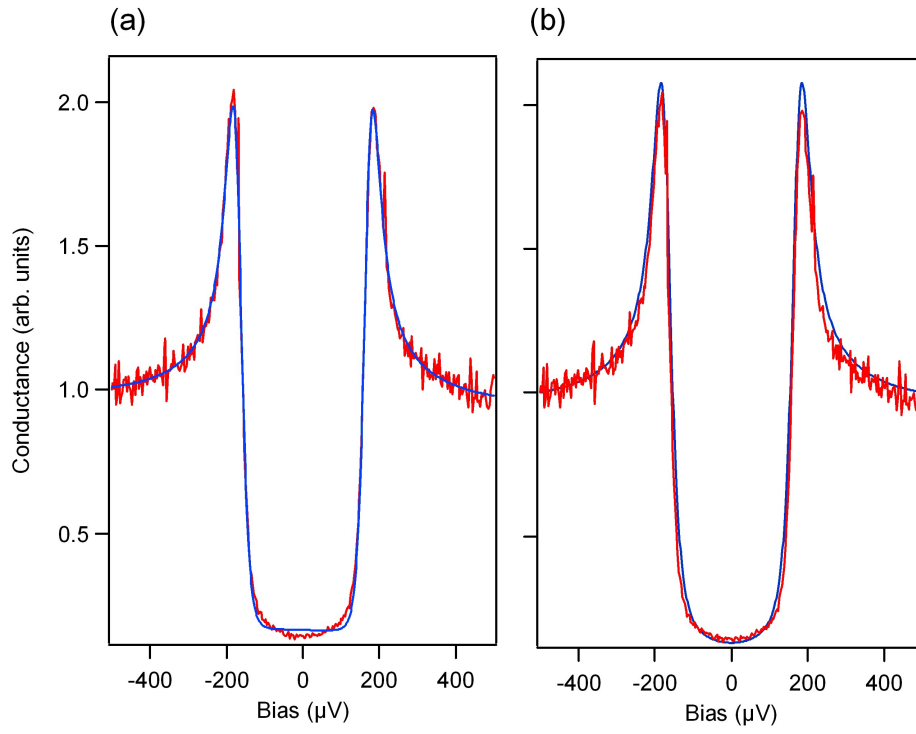


Figure 6.7: Variation of the spectra after tip crash. The tip was stabilized at $V = 2.6 \text{ mV}$, $I = 1 \text{ nA}$. (a) shows the fit to the BCS model to extract the effective temperature. (b) fit to the BTK model for including the effect of a normal metal cluster on the superconducting tip.

Chapter 7

Measurements with Superconductors

In this chapter tunneling measurements between two superconductors are presented. For our measurements we use a vanadium tip and a vanadium sample. Vanadium belongs to the transition metals and can be found at position 23 of the periodic table. It has a body-centered cubic structure with a critical superconducting temperature of 5.4 K [134]. This value depends strongly on the purity of the sample¹. Vanadium is a type II superconductor with a lower critical field of $H_{c1}(T = 0) \approx 0.12$ T and an upper critical field $H_{c2}(T = 0) \approx 0.3$ T [135]. By using Equ. 3.10, we can calculate the theoretical gap parameter for vanadium at zero temperature from $T_C = 5.4$ K to be $\Delta = 819 \mu\text{eV}$.

The V(100) crystal is prepared by two cycles of Ar ion sputtering (20min, 1kV) and annealing ($T_{\text{Final}} \approx 1200$ K). As it is very difficult to prepare a clean V surface² [136], we restrict ourselves only to this minor cleaning procedure. Vanadium tips are fabricated from high purity V wire with 250 μm diameter. They were cut at ambient conditions and transferred immediately into the UHV chamber. For further conditioning we performed a field emission on the V crystal. The I-V characteristic in a voltage range between ± 1 V was used to verify a metallic behavior of the tip.

Images of the surface are shown in Fig. 7.1. We can find flat areas with single and multiple steps. The inset shows a zoom in to a flat region, showing the surface covered with impurities that have a height of about 37 pm.

¹A way to estimate the purity of a sample is the residual resistance ratio (RRR). It is defined as the ratio of the resistance at $T=295$ K to the resistance at base temperature (mostly 4.2 K) R_{295}/R_0 . The crystal used in the measurements of Radebaugh *et al.* has a RRR of 140 which indicates a high purity for Vanadium [134].

²V itself contains a high amount of sulfur, carbon and oxygen impurities in the bulk which diffuse to the surface during the annealing cycle. For cleaning the crystal, Valla *et al.* apply a procedure of Ar ion sputtering at a sample temperature of 1200 K for 100 h [136].

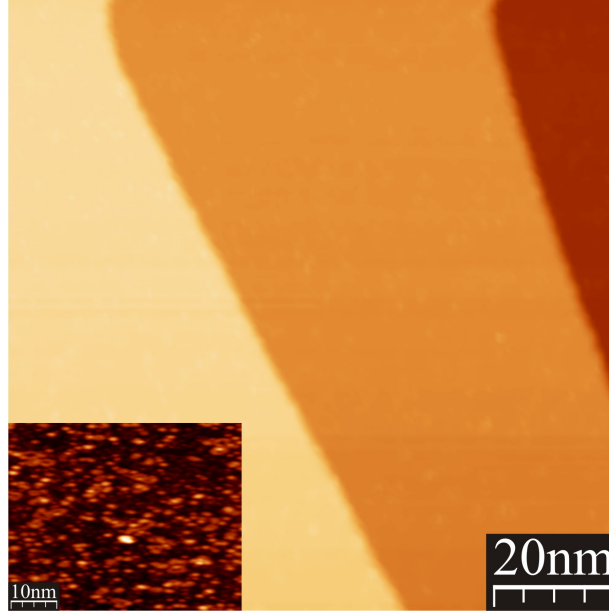


Figure 7.1: Topography of the V(100) surface taken at a bias voltage of $V = -4\text{ V}$ and $I = 50\text{ pA}$. The inset shows an image taken in a flat region. $V = 1\text{ V}$, $I = 100\text{ pA}$.

7.1 Tunneling measurements between a V tip and a V sample

A tunneling measurement of a V tip on V(100) surface at 800 mK is shown in Fig. 7.2. For tunneling between superconductors with equal Δ one would expect the quasi-particle excitation peaks in the tunneling conductance at voltage positions of $\pm 2\Delta/e$. If the superconductors have unequal gap-parameters the peaks are found at $\pm(\Delta_1 + \Delta_2)/e$. The width of the gap in Fig. 7.2 (a) is 2.5 meV resulting in a position of the quasi-particle excitation peaks of $\pm 1.25\text{ mV}$. This value is less than what would be expected from tunneling between vanadium superconductors with equal bulk gap sizes.

A rich peak structure is observed within the energy gap. Peaks at voltage positions of $\pm 750 \pm 5\text{ }\mu\text{V}$, $\pm 470 \pm 5\text{ }\mu\text{V}$ and $\pm 400 \pm 5\text{ }\mu\text{V}$ are observed. A well pronounced Josephson feature is visible with small abating side peaks in the negative and positive voltage range.

The peaks at $\pm 750\text{ }\mu\text{V}$, $\pm 470\text{ }\mu\text{V}$ and $\pm 400\text{ }\mu\text{V}$ can be explained within the framework of multiple Andreev reflections in asymmetric tunneling junctions [46]. From various measurements we know that the peak $V_1 = \pm 750\text{ }\mu\text{V}$ is very stable concerning the energy position whereas the peak at $V_2 = \pm 470\text{ }\mu\text{V}$ can shift. Therefore, the peak at V_1 can be attributed to the gap parameter of bulk vanadium Δ_1 which is smaller compared to the value calculated by Equ. 3.10. As we are far below the critical temperature of V, deviations from the gap parameter due to a finite temperature are not expected. What might have altered the gap parameter are the impurities at the surface. It is known that the critical

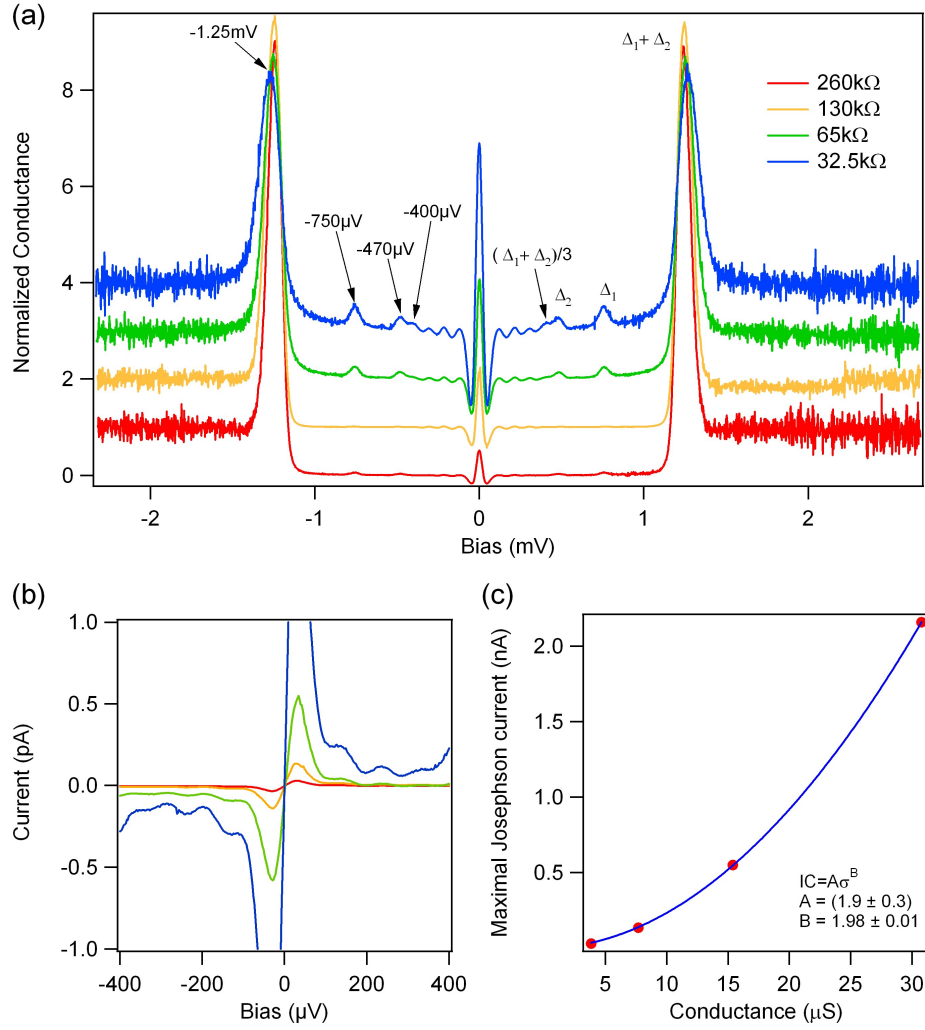


Figure 7.2: Tunneling spectroscopy measurement between a V tip on a V(100) surface at $T=800$ mK. $\Delta_1 = 750 \pm 5 \mu\text{eV}$, $\Delta_2 = 470 \pm 5 \mu\text{eV}$. (a) Conductance curves depending on the normal state tunneling resistance R_N . Curves are shifted against each other. (b) I-V curves in close vicinity of the Fermi energy showing the Josephson current. (c) Maximal Josephson current depending on the normal state conductance $1/R_N$.

temperature is very sensitive to impurities which would alter the gap parameter as well. The shift of the second peak can be related to changes in the tip indicating that $\Delta_2 = eV_2$ is the gap parameter of the tip. The sum of the two leads directly to the positions of the outer quasi-particle peaks. The third peak can be explained by a higher order Andreev reflection process. Using the gap parameters achieved above and inserting them into the relation $V = (\Delta_1 + \Delta_2)/e(2n + 1)$, we find for $n = 1$ a voltage position of $\pm 406 \mu\text{V}$. This value is in good agreement with the measured peak positions at $\pm 400 \mu\text{eV}$.

Very interesting are the peaks appearing to both sides of the Josephson feature in Fig. 7.2 (a). They are observed at voltages $V_1 = 122 \pm 5 \mu\text{V}$, $V_2 = 217 \pm 5 \mu\text{V}$ and $V_3 = 305 \pm 5 \mu\text{V}$. The distance ΔV between the first two peaks is $95 \mu\text{V}$ whereas it is $88 \mu\text{V}$ between the last two. This peak structure has not been reported yet in other STM experiments where tunneling between a superconducting tip and sample has been investigated [10, 46, 137, 138]. These peaks appear only together with the Josephson peak and must be related to it. In the following the dependence of these peaks on the Josephson binding energy, the temperature, the STM tip configuration and the magnetic field is investigated.

The main energy scale which dominates the Josephson effect is the binding energy E_J (Equ. 3.19). It can be tuned by approaching the tip to the sample, thus lowering the normal state resistance as can be seen from Eqs. 3.17 and 3.19. Continuous tuning of the coupling between the two superconducting electrodes is a great advantage of STM compared to planar tunneling junction experiments. The characteristic parameters of the Josephson junctions presented in Figs. 7.2 and 7.3 are summarized in Tab. 7.1. In all measurements the binding energy is smaller or comparable to the thermal energy which is expressed by $\alpha = E_J/k_B T$. This indicates that the influence of thermal fluctuations on the Cooper pairs that tunnel across the junction is not negligible. Values of α for the measurements in Figs. 7.2 and 3.19 are given in Tab. 7.2.

From the maximal current values of the I-V curves in Fig. 7.2 (b) we can construct the dependence of the critical current on the normal state resistance R_N . As it can be seen from Fig. 7.2 (c) it deviates from the behavior predicted by Ambegaokar and Baratoff and shows instead of a linear, a quadratic dependence on the inverse normal state resistance R_N . This quadratic behavior is also observed in [137, 138] and is characteristic for tunneling junctions placed in an electromagnetic environment.

Measurements of the tunneling conductance at a mixing chamber temperature $T = 15 \text{ mK}$ are shown in Fig. 7.3. The positions of the outer quasi-particle excitation peaks changed to $\pm 1.03 \text{ mV}$. We find the value for the bulk gap at a bias value $V = 760 \pm 5 \mu\text{V}$ which leads to a second gap parameter of $\Delta_2 = 240 \mu\text{eV}$. Here we can argue again that the change in the position of $V_2 = \Delta_2/e$ can be attributed to a modification of the STM tip. Therefore Δ_2 can be related to the gap parameter of the tip. The positions of the side peaks around the Josephson feature nevertheless remained constant. For calculating the values in Tab. 7.1 an effective temperature of 100 mK was assumed. This is justified by the measurements of the effective temperature with Aluminum tips.

Another example of two tunneling conductance measurements with a huge tip change in between is shown in Fig. 7.4. Both spectra were recorded at 15 mK with a normal state tunneling resistance $R_N = 520 \text{ k}\Omega$. The positions of the outer quasi-particle peaks

Values for Fig. 7.2: $T = 800 \text{ mK}$, $k_B T = 69 \mu\text{eV}$			
	I_C from Equ. 3.17 (nA)	I_{\max} (nA)	E_J from Equ. 3.19 (μeV)
$R_N = 260 \text{ k}\Omega$	4	29.3	8.2
$R_N = 130 \text{ k}\Omega$	8	134.5	16.3
$R_N = 65 \text{ k}\Omega$	16	549.3	32.8
$R_N = 32.5 \text{ k}\Omega$	32	$2.2 \cdot 10^3$	65.6
Values for Fig. 7.3: $T_{\text{eff}} = 100 \text{ mK}$, $k_B T = 8.6 \mu\text{eV}$			
$R_N = 520 \text{ k}\Omega$	1.34	8	2.75
$R_N = 260 \text{ k}\Omega$	2.68	29	5.5
$R_N = 86.7 \text{ k}\Omega$	8.02	285	16.5

Table 7.1: Values characterizing the Josephson junctions in Figs. 7.2 and 7.3. In the latter case, the MC chamber temperature was at 15 mK. For the calculations the effected temperature estimated in Chap. 6 was used.

Values for Fig. 7.2: $T = 800 \text{ mK}$, $k_B T = 69 \mu\text{eV}$	
	$\alpha = E_J/k_B T$
$R_N = 260 \text{ k}\Omega$	0.12
$R_N = 130 \text{ k}\Omega$	0.24
$R_N = 65 \text{ k}\Omega$	0.48
$R_N = 32.5 \text{ k}\Omega$	0.95
Values for Fig. 7.3: $T_{\text{eff}} = 100 \text{ mK}$, $k_B T = 8.6 \mu\text{eV}$	
$R_N = 520 \text{ k}\Omega$	0.32
$R_N = 260 \text{ k}\Omega$	0.46
$R_N = 86.7 \text{ k}\Omega$	1.92

Table 7.2: Relation between Josephson binding energy and thermal energy in Figs. 7.2 and 7.3. In the latter case, the MC chamber temperature was at 15 mK. For the calculations the effected temperature estimated in Chap. 6 was used.

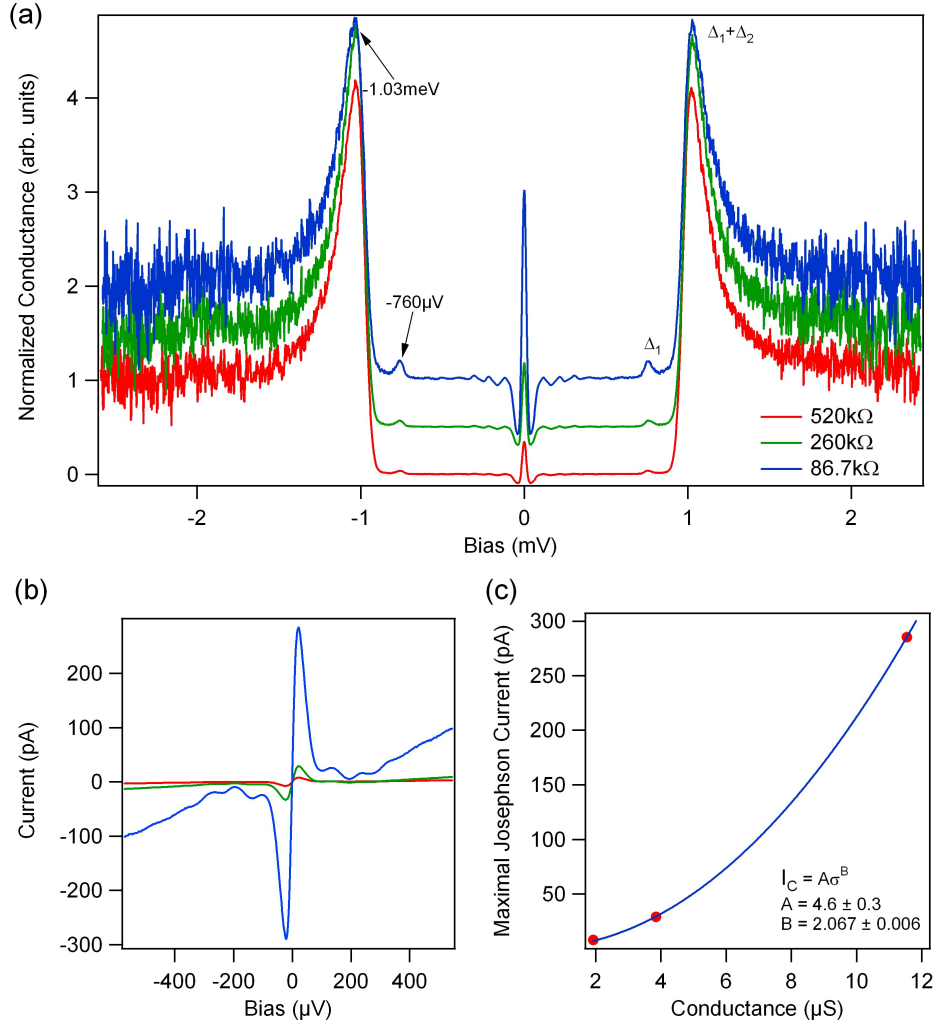


Figure 7.3: Tunneling spectroscopy measurement between a V tip on a V(100) surface at $T=15$ mK. $\Delta_1 = 760 \pm 5 \mu\text{eV}$, $\Delta_2 = 240 \pm 5 \mu\text{eV}$. (a) Conductance curves depending on the normal state tunneling resistance R_N . Curves are shifted against each other. (b) I-V curves in close vicinity of the Fermi energy showing the Josephson current. (c) Maximal Josephson current depending on the normal state conductance $1/R_N$.

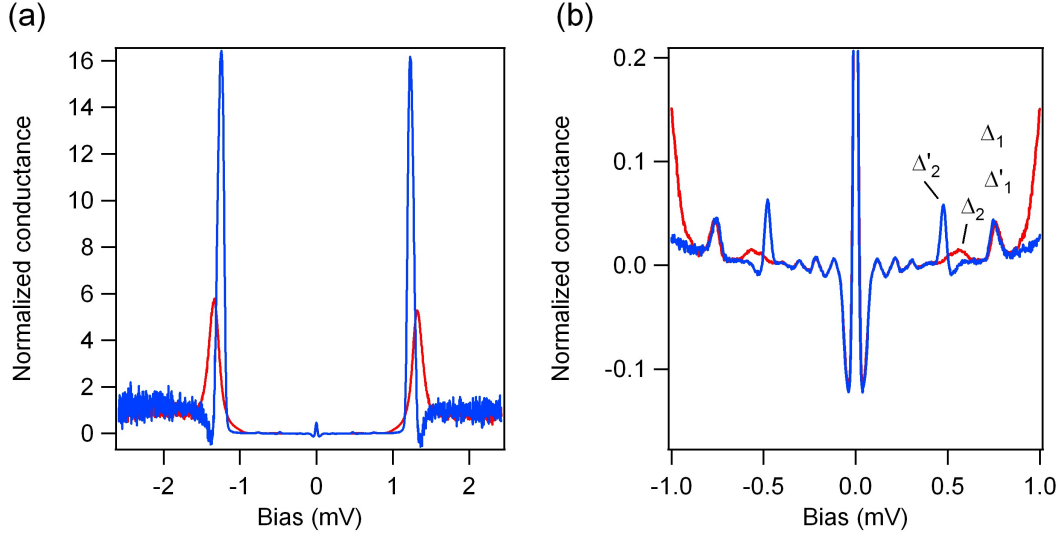


Figure 7.4: Dependence of the Josephson side peaks on the tip arrangement. The Andreev reflection peak for the bulk crystal stayed constant, where the one of the tip changed. Stabilization of the tip at $V = 2.6$ mV, $I = 5$ nA. Red curve: before tip change. $\pm(\Delta_1 + \Delta_2)/e = (1.34 \pm 0.01)$ mV, $\pm\Delta_1/e = (0.76 \pm 0.01)$ mV and $\pm\Delta_2/e = (0.57 \pm 0.01)$ mV. Blue curve: after voltage pulses to -4 V. $\pm(\Delta'_1 + \Delta'_2)/e = (1.24 \pm 0.01)$ mV, $\pm\Delta'_1/e = (0.76 \pm 0.01)$ mV and $\pm\Delta'_2/e = (0.48 \pm 0.01)$ mV.

changed due to different gap parameters of the tip. As seen from Fig. 7.4 (b) the Andreev reflection peak which identifies the gap parameter of the bulk sample Δ_1 stayed constant. Again this tip change did not affect the side peaks of the Josephson current.

Further, we investigated the behavior of the side peaks on the magnetic field (Fig. 7.5). The image shows the whole superconducting gap (a) and a close up of the voltage range around the Fermi level (b). Note, that for this particular tip Δ_2 coincides with the third side peak of the Josephson current. During increasing the magnetic field, the effect on the bulk gap is clearly seen. The energy gap fills up with single electron states due to the breaking of Cooper pairs from the energy supplied by the magnetic field. At the Andreev reflection position of the tip $V_2 = \Delta_2/e$ an independent energy gap starts to form which is unaffected by the magnetic field. At magnetic fields high enough, the bulk sample becomes normal and only the tip remains superconducting. Like in the other experiments also here the side peaks are not affected.

To sum up these experiments, the side peaks of the Josephson current show a strong robustness of the voltage position and the magnitude to the change of the various parameters in the experiments mentioned above. The peaks appear in all experiments at the same voltage position which indicates that their energy stays unaffected. The robustness of the magnitude indicates that the tunneling probability from or into these states remains constant. This leads to the conclusion that the effect behind these peaks, even if only observable together with the Josephson conductance peak, is more fundamental. We believe

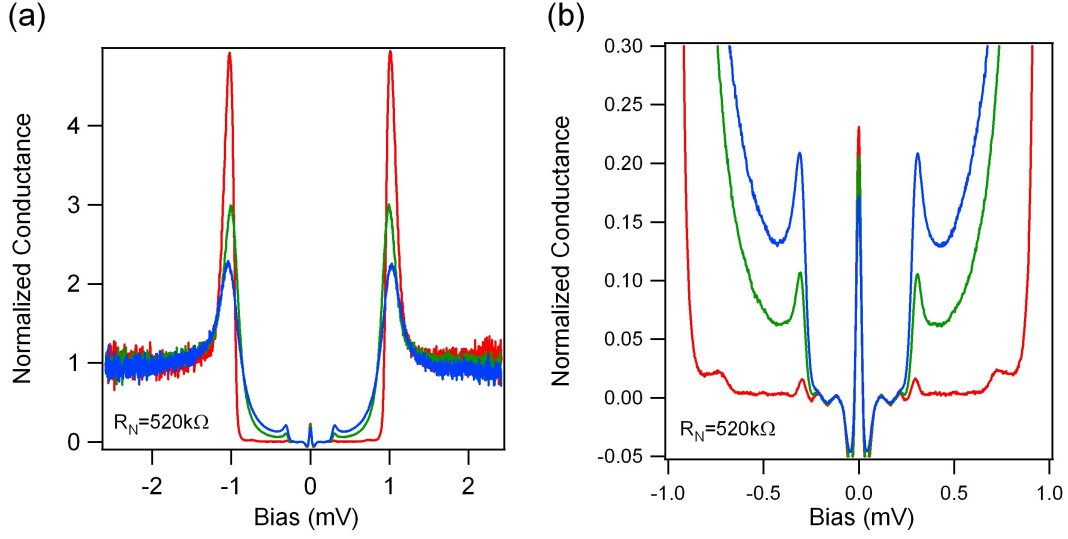


Figure 7.5: Dependence of the Josephson side peaks on an external magnetic field. Red curve 50 mT, green curve 100 mT and blue curve 200 mT. Stabilization of the tip at $V = 2.6$ mV, $I = 5$ nA.

that it is a signature of our setup. Hints to the origin of this phenomena can be found in transport measurements on superconducting single electron transistor devices [139, 140].

For interpreting the Josephson current the electromagnetic environment of the setup is important. The capacitance of the tunneling junction including the inductance of the tip form a parallel resonator circuit which affects the Cooper pairs that are tunneling through the junction due to the Josephson effect. By using the energy of the first side peak of the Josephson effect in the conductance, it is possible to estimate a characteristic frequency $\nu_0 = 29.5$ GHz. The wavelength $\lambda_0 = c/\nu_0$ is 10.2 mm resulting in a $\lambda_0/2$ of 5 mm. It is now interesting to note that this value is of the same order than the extension of the tunneling tip $l_{\text{tip}} = 4$ mm which might act as a resonator for electromagnetic energies associated with ν_0 . Thus, a junction resonator system is formed which can only be treated in combination [140–142]. Cooper pairs tunneling across the junction experience a resonance at energies of $V = h\nu_0/e$ being able to exchange energy with the resonator. This can explain the robustness of the effect because these electromagnetic resonances would be a fingerprint of the experimental setup. It would not depend on material properties of sample and tip as long as the two are superconducting.

7.2 Lifting the spin degeneracy of a quasi-particle density of states on the local scale

The STM offers amazing opportunities when it is combined with the possibility of spin selective measurements [143]. A great variety of systems show interesting magnetic properties on the nano scale depending on the substrate, the lattice orientation or the surrounding environment [144–146].

First spin selective tunneling measurements were achieved by Tedrow and Meservey in 1971 using planar tunneling junctions between a superconducting aluminum film and a nickel electrode [4].

These measurements rely on the lifting of the spin degeneracy of the quasi-particle DOS discovered by Meservey, Tedrow and Fulde one year before [3]. They showed, that in thin aluminum films with a thickness of about 5 nm and a high magnetic field applied parallel to the film the BCS quasi-particle density of states changes into a four peak structure. This is due to the Zeemann splitting as shown in Fig. 7.6. The externally applied magnetic field acts on the electron spins shifting the quasi-particle DOS for the two spin directions by $\pm\mu_B B$, where μ_B is the Bohr magneton and B the external magnetic field. The total BCS DOS can be written as [147]

$$\rho(E) = \rho_{\uparrow}(E) + \rho_{\downarrow}(E) = \frac{1}{2} (\rho_{\text{BCS}}(E + \mu_B B) + \rho_{\text{BCS}}(E - \mu_B B)) \quad (7.1)$$

where $\rho_{\text{BCS}}(E)$ can be expressed with Equ. 3.8.

To observe this splitting in an experiment the following main conditions have to be fulfilled. The in-plane critical magnetic field of the film has to be much higher than the bulk critical field because the superconductivity has to remain in the magnetic fields which are needed to observe the splitting. These fields are in the order of 1 – 2 T which is larger than the bulk critical field of many superconductors. Beside this, the effect on the electron orbits has to be small compared to the effect on the electron spins. The more the external magnetic field affects the electron orbits in the cooper pairs, the larger the broadening of the peaks in the tunneling conductance and the more difficult is it to resolve the spin splitting. These two conditions are fulfilled for the aluminum films used by Meservey, Tedrow and Fulde.

The Meservey-Tedrow-Fulde effect can be used to determine the absolute spin polarization P at E_F of ferromagnetic materials. Different electron densities for spin up (n_{\uparrow}) and spin down (n_{\downarrow}) electrons contribute to the tunneling conductance. The electron spin is assumed to be conserved during tunneling events. Using the fraction a of electrons with majority spin

$$a = n_{\uparrow}/(n_{\uparrow} + n_{\downarrow}) \quad (7.2)$$

the combined tunneling conductance from a superconductor in an applied field into a spin polarized material with polarization along the field direction is

$$\sigma = \frac{dI}{dV} = (a\rho_{\text{BCS}}(E + \mu_B B) + (1 - a)\rho_{\text{BCS}}(E - \mu_B B)) \otimes f'(E - eV, T). \quad (7.3)$$

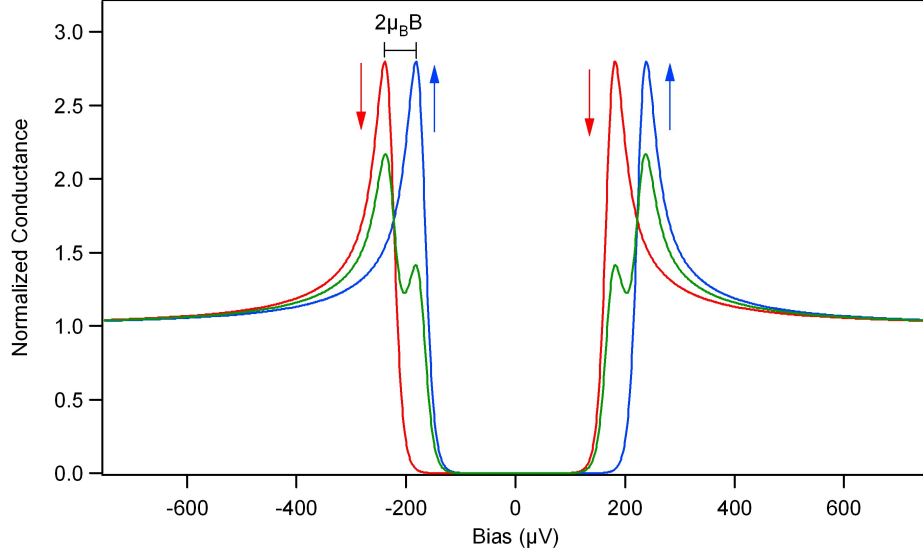


Figure 7.6: Calculation of the spin splitting of the SC quasi-particle density of states in magnetic fields. The effect of an external magnetic field is shown when the spin orbit interaction is neglected. The red and the blue curve show the quasi-particle conductance ($\Delta = 200 \mu\text{eV}$) for the two spin directions that are shifted by $\pm\mu_B B$. The resulting conductance (green) was calculated according to Equ. 7.1 using a field of 0.5 T at a temperature of 100 mK.

The convolution \otimes with the derivative of the Fermi function is used to include temperature broadening effects. The electron polarization P at the Fermi level is

$$P \equiv \frac{n_{\uparrow} - n_{\downarrow}}{n_{\uparrow} + n_{\downarrow}} = 2a - 1 \quad (7.4)$$

This results in an asymmetry in the magnitude among the inner and the outer peaks as shown in Fig. 7.7. This asymmetry is more pronounced for the inner peaks, because here the spin polarization of the quasi-particle DOS for the superconductor is higher. At the outer peaks both spin channels contribute to the tunneling conductance. The polarization is extracted by comparing two pairs of measured conductance values $\sigma_1 = G(-V_0 - \mu_B B)$, $\sigma_2 = G(-V_0 + \mu_B B)$, $\sigma_3 = G(V_0 - \mu_B B)$, $\sigma_4 = G(V_0 + \mu_B B)$, with G the conductance and V_0 an arbitrary but fixed bias value [147]

$$P = \frac{(\sigma_4 - \sigma_2) - (\sigma_1 - \sigma_3)}{(\sigma_4 - \sigma_2) + (\sigma_1 - \sigma_3)}. \quad (7.5)$$

The splitting of the quasi-particle density of states in a superconductor was up to now only demonstrated for planar tunnel junction. It could so far not achieved with an STM tip. Difficulties arise in the use of the right tip material. One has to limit the effect on the electron orbits indicating that the tip material should have low spin-orbit

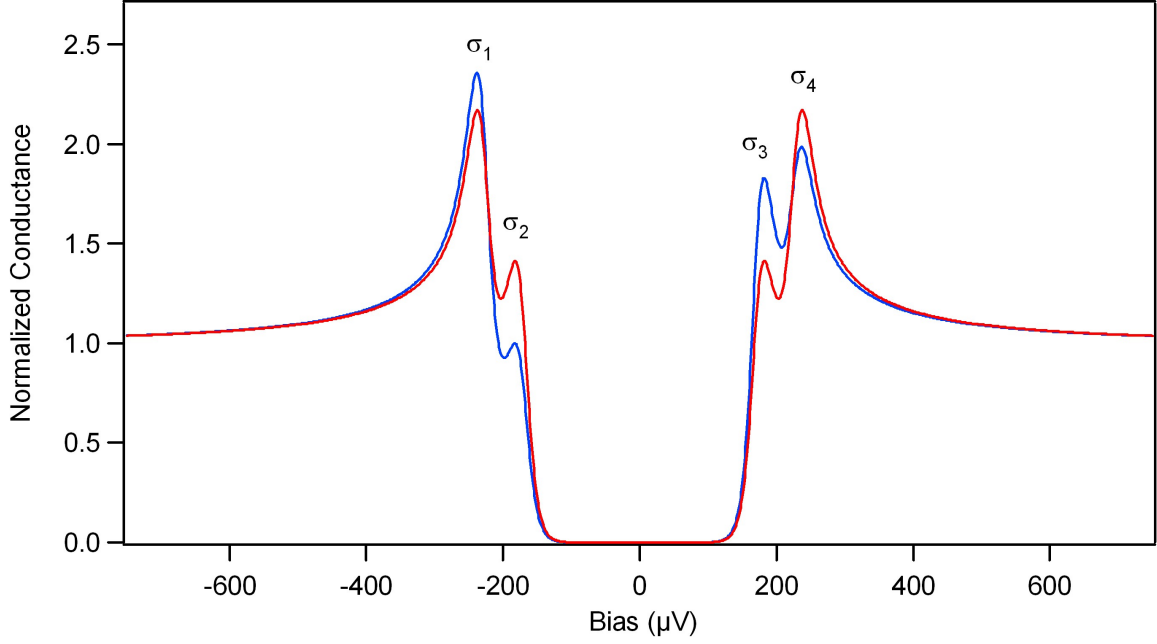


Figure 7.7: Calculation of the asymmetry in the spin-split quasi-particle DOS when tunneling into a spin polarized material. Red curve: the second electrode is a normal metal showing no spin polarization at the Fermi level. No asymmetry is observed. Blue curve: the second electrode has a finite spin polarization P at the Fermi level. An asymmetry in the combined quasi-particle DOS is observed. Different tunneling probabilities for electrons with majority and minority spin contribute to the conductance. $\Delta = 200 \mu\text{eV}$, $T = 100 \text{ mK}$, $P = 30\%$.

interaction. Beside this a high transition temperature and high critical fields are needed. Spin-orbit interaction increases with Z^4 (Z atomic number of the superconducting element) demanding that the Z is as low as possible. Al is a superconductor with atomic number $Z=13$ and has the lowest spin orbit interaction among the superconductors but also low bulk critical fields of 10mT [148]. Vanadium in our case has $Z=23$ with a bulk critical field of 0.3 T. The condition of low spin orbit coupling is fulfilled and also the critical fields are high enough when using a V tip. As already mentioned in the last section it is common that the tip remains superconducting if the external magnetic fields are above the bulk critical field [149, 150]. We observed superconductivity in our V tip up to fields of $B = 2$ T. In the following, first measurements are shown that demonstrate the splitting of the quasi-particle density of states in the tip of an STM.

The measurements are performed using a V-tip on a V(100) crystal. The applied external magnetic field was high enough to destroy the superconductivity in the bulk crystal. Only the tip remained superconducting. This was confirmed by the absence of the Josephson effect which cannot be observed in superconductor-normal conductor tunneling junctions. The magnetic field dependence of tunneling spectra was measured for three different tip-sample distances having the following normal state resistances: (i) $R_N = 5.2 \text{ M}\Omega$, (ii) $R_N = 520 \text{ k}\Omega$ and (iii) $R_N = 86.67 \text{ k}\Omega$. Representative results for $R_N = 520 \text{ k}\Omega$ are shown in Fig. 7.8. In the conductance spectra clear shoulders in the quasi-particle coherence peaks are visible. These shoulders are observed for finite temperatures in superconducting conductance spectra, when the measured DOS is a sum of different single DOS, like it is the situation in multi band superconductors [130, 151]. In our case the kinks shift clearly when the external magnetic field is increased which proves the magnetic origin. We contribute this magnetic field dependence to the Meservey-Tedrow-Fulde effect. Fitting these curves to Equ. 7.1 leads to the results shown in Fig. 7.8. On the measured spectra the curves from the fitting procedures are superimposed.

From the fitting results we get the values for the energy shift $\mu_B B$ of the quasi-particle DOS for spin up and spin down electrons. The extracted values for the energy shift are displayed in Fig. 7.9 for normal state resistances R_N of 5.2 M Ω , 520 k Ω and 86.7 k Ω . They scale linearly with the applied magnetic field. A linear fit yields a slope of $41.5 \pm 1.5 \mu\text{eV/T}$ which is a factor 1.4 smaller than μ_B . It is not uncommon to have deviations from theory [22] because the g-value, that relates the magnetic moment to a quantum number does not necessary need to be two.

Still a finite error between the fit and measured data is observed. As the theory is used without spin orbit coupling it can not be treated as complete. Spin orbit interaction is discussed by Meservey *et al.* [152]. It leads to additional broadening of the quasi-particle densities of states that could limit the resolution of the combined peak structure. A general description by Maki [153], which includes spin-orbit interaction and an additional orbital depairing parameter might result in more accurate fits [154].

Also here we have to be aware of tip effects. Therefore, different tips may result in different shapes of the conductance curve allowing the effect to be resolved with one tip more clearly than with the other.

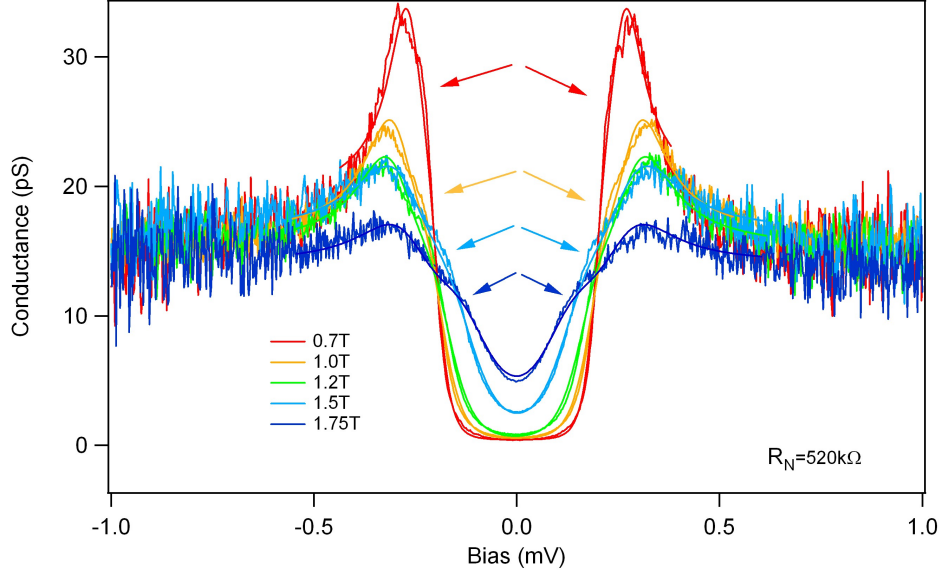


Figure 7.8: Quasi-particle DOS depending on the magnetic field. The arrows indicate kinks in the spectrum that change with magnetic field. These kinks occur if the measured DOS is formed out of different single quasi-particle DOS. Straight lines are fits to the data by using the Meservey-Tedrow-Fulde model. $T = 15$ mK.

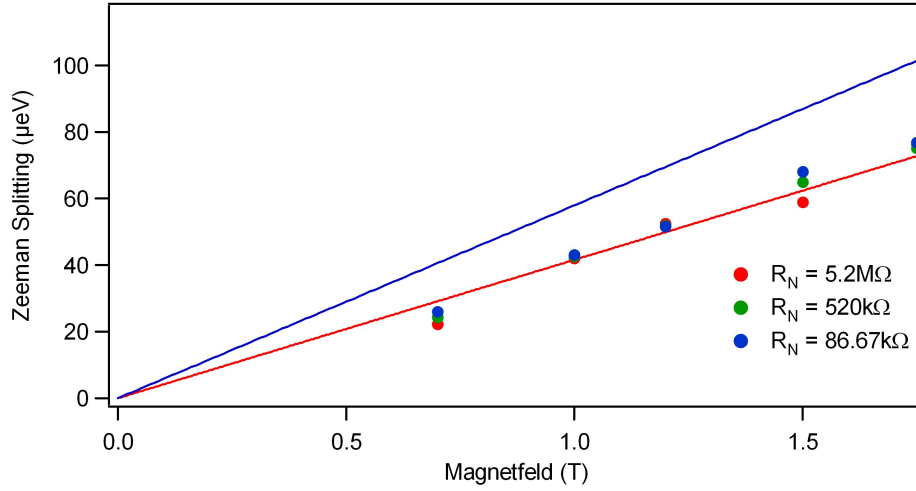


Figure 7.9: Extracted Energy shift $\pm\mu_B B$ of the quasi-particle DOS depending on the magnetic field. Red data points: $R_N = 5.2 M\Omega$, green data points: $R_N = 520 k\Omega$ and blue data points: $R_N = 86.7 k\Omega$. The red line is the fit to the data, the blue line corresponds to the theoretical value $E = \mu_B B$.

Chapter 8

Summary and Outlook

During this thesis a scanning tunneling microscopy system for measurements at temperatures below 20 mK in high magnetic fields was developed and set up. This was achieved by attaching the STM to the mixing chamber of a $^3\text{He}/^4\text{He}$ dilution cryostat. The setup allows *in situ* preparation of the samples to investigate. Tips and samples can be transferred from the UHV chamber into the STM without breaking the vacuum between both. This setup is suited to study two different classes of subjects that have so far been difficult to access with STM. It is possible now, to investigate the physics of low temperature phase transitions locally. Beside this, one has the possibility to perform high resolution tunneling spectroscopy measurements on an atomic scale of single adsorbates on surfaces.

In the framework of this thesis the construction details for the mK-STM are given. We implemented a modular design concept which enables easy maintenance of the single components. For the realization it is important to include cryogenic considerations into the design. One has to be careful with the materials to be used concerning their thermal conductivity at low temperature and their thermal expansion. The STM unit was constructed using an optimization criterion for the geometrical design. The main structure of the STM was realized such, that external disturbances have less effect on the spacing between tip and sample. To connect the STM to the mixing chamber of the dilution cryostat a link structure has to be used. A point of main concern is the wiring of the cryostat and the STM unit. From the room temperature feedthrough to the MC the input of heat transmitted along the wire should be as small as possible. From the MC to the STM a good thermal contact is desired. Based on these aspects the wiring scheme for the mK-STM is explained. For a stable tunneling contact we need a low vibration level of the STM and the cryostat. To achieve this, we isolate the cryostat from the floor by a combined use of active and passive dampers. Pumping lines for the cryostat operation are carefully anchored to a heavy mass (also damped actively) before they reach the cryostat. For testing the STM unit two independent test systems have been set up. The first operates at room temperature whereas the second is a variable temperature setup. Both are equipped with independent preparation chambers. Results from these systems demonstrate the stability of the STM unit.

A temperature measurement proved a lattice temperature of 17 mK at tip and 20 mK

at sample position of the STM unit. The effective temperature which corresponds to the energy resolution of the STM was estimated by taking tunneling spectra using a type I superconductor (Al) as tip material and a normal conducting sample (Cu(111)). From fits to the BCS theory we could extract the lowest effective temperature T_{eff} to be 87 ± 3 mK which corresponds to an electronic resolution of $3.5k_B T_{\text{eff}} \approx 26 \pm 1$ μeV . T_{eff} can be seen as an upper limit for the electron temperature of our setup because it includes the broadening of all noise sources within the setup. This measurement was done at a mixing chamber temperature of 15 mK. It was achieved without any filtering at low temperatures. A precise estimation of the tunneling stability between tip and sample was done at a temperature of 800 mK by recording the tunneling current without activated feedback loop of the STM controller. Using a calibration which we got from $I - z$ spectroscopy curves we could extract a stability of ± 1.35 pm.

Tunneling spectroscopy measurements between two superconductors were presented using a V(100) sample and a V tip. A sub-gap structure was observed which could be attributed to multiple Andreev reflection processes in asymmetric tunneling junctions. The zero bias conductance peak resulting from the Josephson effect showed robust side peaks which can be attributed to the interaction of the tunneling Cooper pairs with the electromagnetic environment into which the tunneling junction is integrated.

Applying external magnetic fields that exceed the bulk critical field of vanadium results in a quenching of the superconductivity in the sample. As the tip consists of a cluster at the apex, the superconductivity could resist fields that are larger than the bulk critical field. Increasing the magnetic fields further results in kinks in the quasi-particle excitation peaks which is an indication of a multiple gap structure in the conductance. The position of these kinks scales linearly with the magnetic field. This behavior is well described by the model of Meservey, Tedrow and Fulde [3] using the spin separation of the quasi particle density of states. This is the first observation of this effect in an STM measurement.

In the following I will outline two experiments for which the setup described in this thesis is ideally suited as they demand a combination of high energy resolution and *in situ* sample preparation. The first experiment is based on spin polarized tunneling using the Meservey-Tedrow-Fulde effect. The second is the investigation of the hyperfine interaction of electrons with magnetic nuclear moments using an STM.

8.1 Spin polarized tunneling using the Meservey-Tedrow-Fulde effect

Lifting the spin degeneracy of the quasi-particle density of states in superconductors can be used to measure the absolute spin polarization of tunneling electrons at the Fermi level. As shown in Equ. 7.3 the effect of tunneling into a ferromagnetic material is accounted by including a weighting factor a into the spin polarized quasi-particle density of states [4,147]. The value a is the fraction of tunneling electrons with magnetic moment parallel to the external magnetic field. A well studied system to test the capability of measuring the spin

polarization are Co nanoislands on Cu(111) [144, 155]. In the regime of sub-monolayer coverage Co forms triangular islands of two monolayer height. They have an out of plane magnetically axis with relatively high coercive magnetic fields $1\text{ T} < \mu_0 H_C < 1.5\text{ T}$. So far, measurements with STM tips coated with ferromagnetic and anti-ferromagnetic materials where successful in extracting a relative magnetization between tip and Co island in an energy range at 400 meV below the Fermi energy [156]. Further, not only ferromagnetism and anti ferromagnetism but also spin polarized currents through single nano structures are of interest. For example, the question can be addressed how the spacial distribution of spin currents in single molecules adsorbed to a ferromagnet varies. By using the Meservey-Tedrow-Fulde effect, we have a tool to directly measure the absolute spin polarization of these systems at the Fermi energy on a local scale.

8.2 Measuring the hyperfine interaction of single atoms on the local scale

A second experiment for which the capabilities of the mK-STM system would be suited is the measurement of the interaction between electron and nuclear spins at the atomic scale. Nuclear spins are of particular interest in quantum computation because they are well isolated from their environment and are proposed as qu-bits with a low decoherence rate [157]. The nuclear spin of an adsorbate is connected to tunneling electrons through nuclear-spin interaction which leads to a hyperfine splitting of the different spin states.

One way to measure the hyperfine splitting in STM is to look for high frequency resonances in the noise spectrum of the tunneling current. The hyperfine splitting is observed as small side peaks around a main peak centered at the atoms Larmor frequency [158]. The measurement of these peaks demands an electronics that is able to detect signals in the GHz range.

Another method of measuring the hyperfine interaction could be inelastic scanning tunneling spectroscopy (IETS) given the electronic resolution of the setup is high enough. A concrete proposal for this is given by Delgado and Fernández-Rossier [159]. Similar to single spin flip transitions, the hyperfine interaction is predicted to lead to conductance steps in the IETS spectra. The observation of the transitions between single hyperfine levels should therefore be possible.

The Heisenberg Hamiltonian describing the magnetic properties of a single atom on surfaces can be written as

$$H_S = g\mu_B \vec{B} \cdot \vec{S} + A \vec{S} \cdot \vec{I} \quad (8.1)$$

The first term of Equ. 8.1 is the Zeemann splitting of the spin states where the second term couples the electron spin \vec{S} with the nuclear spin \vec{I} . Here A is the hyperfine constant which depends on the nuclear magnetic moment and the environment in which the atom is embedded. A normally is in the order of μeV . Splitting of the electronic energy levels due to asymmetry terms and the Zeemann splitting of the nuclear levels are not considered. This in total results in $(2S+1) \times (2I+1)$ states where S is the electron spin quantum number and

I the nuclear spin quantum number for a given atom. In zero magnetic field the spin states are degenerated if no hyperfine interaction is present. Including the hyperfine interaction leads to a splitting of the spin states with conductance steps at energies $eV = S_z A \Delta I$ assuming $\Delta S_z \simeq 0$. For a nuclear spin of I every spin level splits into $2I + 1$ hyperfine levels separated by A .

Delgado and Fernández-Rossier suggested ^{232}Bi atoms in Si as material system to measure, because it shows a high A value of $6.1 \mu\text{eV}$ between the $I = 9/2$ energy level and an electronic donor state. They calculated the zero field splitting to be $5A$ which should give rise to a conductance step at $V_{\text{hyperfine}} \approx \pm 30 \mu\text{eV}$. This results in a total separation of the conductance steps of $\Delta E_{\text{IETS}} \approx 60 \mu\text{eV}$. In an IETS experiment the electronic resolution is $5.4 k_B T$. Inserting the best effective temperature $T_{\text{eff}} = 87 \pm 3 \text{ mK}$ achieved in the tunneling experiments between the Al tip on the Cu sample (Chap 6) yields $\Delta E \approx 41 \mu\text{eV}$. This means our energy resolution is smaller than the energy separation of the conductance steps for the transition between two hyperfine levels. We therefore have a good chance of observing the hyperfine transitions of ^{232}Bi atoms on Si.

Appendix A

Abbreviations and Symbols

BCS	<i>Bardeen, Cooper and Schrieffer</i>
BTK	<i>Blonder, Tinkham and Klapwijk</i>
CF	<i>Conflat</i>
CM	<i>Coarse Motor</i>
CMN	<i>Cerium Manganese Nitrate</i>
CuBe	<i>Beryllium copper</i>
DOS	<i>Density of states</i>
DR	<i>Dilution refrigerator</i>
e-beam	<i>Electron beam</i>
ICP	<i>Intermediate cold plate</i>
IETS	<i>Inelastic tunneling spectroscopy</i>
FPD	<i>Fixed point device</i>
HV	<i>High voltage</i>
LDOS	<i>Local density of states</i>
MC	<i>Mixing chamber</i>
NTC	<i>Negative Temperature Coefficient</i>
PTFE	<i>Polytetrafluorethylen</i>
PZT	<i>Lead zirconate titanate</i>
RGA	<i>Residual gas analyzer</i>
RuO	<i>Ruthenium oxide</i>
SIS	<i>Superconductor – Insulator – Superconductor</i>
SIN	<i>Superconductor – Insulator – Normal conductor</i>
SP	<i>Scanning piezo</i>
STM	<i>Scanning Tunneling Microscopy</i>
TSP	<i>Titanium sublimation pump</i>
UHV	<i>Ultra High Vacuum</i>

Appendix B

Component models and companies

Cryostat

dewar	<i>JANIS, model 27CNDT liquid nitrogen shielded dewar</i>
insert	<i>JANIS, model JDR-500</i>
roots pump	<i>Alcatel, model 601</i>
^3He pump	<i>Alcatel, model 2063H</i>
LN pump	<i>Oerlikon Leybold, model: Sogevac SV65B</i>
1K-pot pump	<i>Oerlikon Leybold, model: Sogevac SV65B</i>
coaxial cables	<i>JANIS, model N12-50F-257-0</i>
single wires	<i>JANIS, Manganin</i>

Link structure and STM unit

coaxial cables	<i>Elspec, model: DA50047-821 and LakeShore, model: CC-SC-500</i>
silver wires	<i>GoodFellow, model: AG005842</i>
coarse motor	<i>attocube systems AG, model: ANPz50/LT/UHV z-positioner</i>
scanning piezo	<i>EBL, model: 1, piezoceramic tube</i>
insulating epoxy	<i>Epoteck, model: H77</i>
conducting epoxy	<i>Epoteck, model: E4110</i>

UHV chamber

transfer mechanism	<i>Ferrovac, model: MD40HT-1050</i>
Argon bombardment system	<i>Omicron, model: ISE 10</i>
sample magazine	<i>VAB, model: MDS40-200</i>
tip magazine	<i>VAB, model: MDS40-200</i>
manipulator	<i>VAB, model: PM12-250 with DDF63p</i>
flow cryostat for manipulator	<i>VAB, model HVK-St-250</i>
main turbo pump	<i>Pfeiffer, model: HiPace 700M</i>
ion pump	<i>Leybold, model: IZ 100</i>
titanium sublimation pump	<i>VAB, model: LN 200 with TVP 40</i>
load-lock turbo pump	<i>Pfeiffer, model: TMU 071</i>
load-lock transfer	<i>Ferrovac, model: GMD40-400</i>
residual gas analyzer	<i>Pfeiffer, model: QME 200</i>

Damping and Electronics

Active isolators	<i>TMC, model: Stacis 2100/3000</i>
Passive isolators	<i>Newport, model: I-2000</i>
I-V Converter	<i>Femto, model: DLPCA-200</i>
STM electronics	<i>Nanonis, model: RC4, SC4, HVA4, HVS4, PMD4</i>
AC resistance bridge	<i>Lake Shore, model: 370</i>
LCR meter	<i>Agilent, model: 4263B</i>
RF Filters for Current, Bias and z	<i>Spectrum control Inc., model: 51-726-017</i>
RF Filters for piezo connections	<i>Spectrum control Inc., model: 1289-004</i>

Bibliography

- [1] Kamerlingh-Onnes, H. *Comm. Phys. Lab. Univ. Leiden* **122b** (1911).
- [2] Bardeen, J., Cooper, L., and Schrieffer, J. *Physical Review* **108**, 1175 (1957).
- [3] Meservey, R., Tedrow, P., and Fulde, P. *Physical Review Letters* **25**, 1270 (1970).
- [4] Tedrow, P. and Meservey, R. *Physical Review Letters* **26**, 192 (1971).
- [5] Binnig, G., H.Rohrer, Gerber, C., and Weibel, E. *Applied Physics Letters* **40**, 178 (1982).
- [6] Binnig, G., H.Rohrer, Gerber, C., and Weibel, E. *Physical Review Letters* **49**, 57 (1982).
- [7] Binnig, G., H.Rohrer, Gerber, C., and Weibel, E. *Physical Review Letters* **50**, 120 (1983).
- [8] Shvarts, V., Zhao, Z., Bobb, L., and Jirmanus, M. *Journal of Physics: Conference Series* **150**, 012046 (2009).
- [9] Moussy, N., Courtois, H., and Pannetier, B. *Review of Scientific Instruments* **72**, 128 (2001).
- [10] Rodrigo, J., Suderow, H., and Vieira, S. *European Physical Journal B* **40**, 483 (2004).
- [11] Marz, M., Goll, G., and Löhneysen, H. *Review of Scientific Instruments* **81**, 045102 (2010).
- [12] T. Matsui, H. K. and Fukujama, H. *J. Low Temp. Phys.* **121**, 803 (2000).
- [13] Song, Y., Otte, A., Shvarts, V., Zhao, Z., Kuk, Y., Blankenship, S., Band, A., Hess, F., and Strocio, J. *Review of Scientific Instruments* **81**, 121101 (2010).
- [14] Michaelson, H. *Journal of Applied Physics* **48**, 4729 (1977).
- [15] Bardeen, J. *Physical Review Letters* **6**, 57 (1961).
- [16] Giaever, I. *Physical Review Letters* **5**, 147 (1960).

- [17] Tersoff, J. and Hamann, D. *Physical Review Letters* **50**, 1998 (1983).
- [18] Tersoff, J. and Hamann, D. *Physical Review B* **31**, 805 (1985).
- [19] Feenstra, R., Thompson, W., and Fein, A. *Physical Review Letters* **56**, 608 (1986).
- [20] Crommie, M., Lutz, C., and Eigler, D. *Nature* **363**, 524 (1993).
- [21] Stipe, B. and Ho, W. *Review of Scientific Instruments* **70**, 137 (1999).
- [22] Heinrich, A., Gupta, J., Lutz, C., and Eigler, D. *Science* **306**, 466 (2004).
- [23] Matsui, T., Kambara, H., Niimi, Y., Tagami, K., Tsukada, M., and Fukuyama, H. *Physical Review Letters* **94**, 226403 (2005).
- [24] Yazdani, A., Jones, B., Lutz, C., Crommie, M., and Eigler, D. *Science* **275**, 1767 (1997).
- [25] Ibach, H. and Lüth, H. *Festkörperphysik*. Springer, (2002).
- [26] Lauhon, L. and Ho, W. *Review of Scientific Instruments* **72**, 216 (2001).
- [27] Lambe, J. and Jaklevic, R. *Physical Review* **165**, 821 (1968).
- [28] Klein, J., Léger, A., Belin, M., Defourneau, D., and Sangster, M. *Physical Review B* **7**, 2336 (1973).
- [29] Mamin, H., Abraham, D., Ganz, E., and Clarke, J. *Review of Scientific Instruments* **56**, 2168 (1985).
- [30] Besocke, K. *Surface Science* **181**, 145 (1987).
- [31] Pan, S., Hudson, E., and Davis, J. C. *Review of Scientific Instruments* **70**, 1459 (1999).
- [32] Pohl, D. *Review of Scientific Instruments* **58**, 54 (1986).
- [33] van Delft, D. and Kes, P. *Physics Today* **63**, 38 (2010).
- [34] Meissner, W. and Ochsenfeld, R. *Naturwissenschaften* **44**, 787 (1933).
- [35] London, F. and London, H. *Proceedings of the Royal Society of London: Series A* **149**, 71 (1935).
- [36] Abrikosov, A. *Sov. Phys. JETP* **5**, 1174 (1957).
- [37] Tinkham, M. *Introduction to Superconductivity*. Dover Publication, Inc, (1996).
- [38] Annett, J. *Superconductivity, superfluids and condensates*. Oxford University Press, (2004).

-
- [39] Fröhlich, H. *Physical Review* **79**, 845 (1950).
- [40] Fröhlich, H. *Proceeding of the Royal Society of London* **215**, 291 (1952).
- [41] Bardeen, J. and Pines, D. *Physical Review* **99**, 1140 (1955).
- [42] R.C. Dynes, V. N. and Garno, J. P. *Physical Review Letters* **41**, 1509 (1978).
- [43] Andreev, A. *Sov. Phys. JETP* **19**, 1228 (1964).
- [44] Klapwijk, T., Blonder, G., and Tinkham, M. *Physica* **109**, 1657 (1982).
- [45] Blonder, G., Tinkham, M., and Klapwijk, T. *Physical Review B* **25**, 4515 (1982).
- [46] Ternes, M., Schneider, W., Cuevas, J., Lutz, C., Hirjibehedin, C., and Heinrich, A. *Physical Review B* **74**, 132501 (2006).
- [47] Ternes, M. *Scanning tunneling spectroscopy at the single atom scale*. PhD thesis, École polytechnique fédérale de Lausanne, (2006).
- [48] Josephson, B. *Physics Letters* **1**, 251 (1962).
- [49] Ambegaokar, V. and Baratoff, A. *Physical Review Letters* **10**, 486 (1963).
- [50] Ambegaokar, V. and Baratoff, A. *Physical Review Letters, erratum* **11**, 104 (1963).
- [51] Joyez, P., Vion, D., Götz, M., Devoret, M., and Esteve, E. *Journal of Superconductivity* **12**, 757 (1999).
- [52] Lounasmaa, O. V. *Experimental principles and methods below 1K*. (1974).
- [53] Betts, D. S. *An introduction to millikelvin technology*. Cambridge Univ Pr, (1989).
- [54] Pobell, F. *Matter and Methods at Low Temperatures*. Springer, 3rd ed. edition, October (2007).
- [55] Pobell, F. *Journal of Low Temperature Physics* **87**, 635 (1992).
- [56] Huiku, M. T., Jyrkkiö, T. A., Kynnäräinen, J. M., Lojonen, M. T., Lounasmaa, O. V., and Oja, A. S. *Journal of low temperature physics* **62**, 433 (1986).
- [57] Oja, A. S. and Lounasmaa, O. V. *Reviews of Modern Physics* **69**, 1 (1997).
- [58] Johnson, R. *Physical Review Letters* **22**, 449–451 (1969).
- [59] Osheroff, D. *Physical Review Letters* **28**, 885–888 (1972).
- [60] Wheatley, J. C., Vilches, O., and Abel, W. *Physics* **4**, 1 (1968).
- [61] London, H. *Proc. Int. Conf. Low Temperature Physics*, 157 (1951).

- [62] London, H., Clarke, G., and Mendoza, E. *Physical Review* **128**, 1992 (1962).
- [63] Das, T., de Bruyn Ouboter, R., and Taconis, K. *Proc. 9th Int. Conf. Low Temperature Physics* , 1253 (1965).
- [64] Hall, H., Ford, P., and Thompson, K. *Cryogenics* **6**, 80 (1966).
- [65] Frossati, G. *Journal de Physique* **39**, 1578 (1978).
- [66] Vermeulen, G. and Frossati, G. *Cryogenics* **27**, 139–147 (1987).
- [67] Keller, W. *Helium-3 and Helium-4*. Plenum Press, (1969).
- [68] Wheatley, J. C. *American Journal of Physics* **36**, 181 (1968).
- [69] Bardeen, J., Baym, G., and Pines, D. *Physical Review* **156**, 207 (1967).
- [70] Ebner, C. and Edwards, D. *Physics Reports* **2**, 77 (1971).
- [71] Peshkov, V. *Sov. Phys. JETP* **24**, 1227 (1968).
- [72] Watson, G., Reppy, J. D., and Richardson, R. *Physical Review* **188**, 384 (1969).
- [73] Pobell, F. *Matter and Methods at Low Temperatures*. Springer, 3rd ed. edition, October (2007).
- [74] Wheatley, J. C., Rapp, R. E., and Johnson, R. T. *Journal of Low Temperature Physics* **4**, 1–39 (1971).
- [75] Uhlig, K. *Cryogenics* **27**, 454–457 (1987).
- [76] DeLong, L. E., O.G.Symko, and Wheatley, J. *Review of Scientific Instruments* **42**, 147 (1971).
- [77] van der Maas, J., Probst, P., Stubi, R., and Rizzuto, C. *Cryogenics* **26**, 471–474 (1986).
- [78] Greywall, D. *Physical Review B* **27**, 2747 (1983).
- [79] Greywall, D. *Physical Review B* **33**, 7520 (1986).
- [80] Lawes, G., Zassenhaus, G. M., Koch, S., Smith, E. N., Reppy, J. D., and Parpia, J. M. *Review of Scientific Instruments* **69**, 4176 (1998).
- [81] Raccanelli, A., Reichertz, L. A., and Kreysa, E. *Cryogenics* **41**, 763–766 (2001).
- [82] Gorla, P., Bucci, C., and Pirro, S. *Nuclear Instruments and Methods in Physics Research Section A: Accelerators, Spectrometers, Detectors and Associated Equipment* **520**, 641–643 (2004).

-
- [83] Sawada, A., Inoue, S., and Masuda, Y. *Cryogenics* **26**, 486 (1986).
- [84] Childs, P., Greenwood, J., and Long, C. *Review of Scientific Instruments* **71**, 2959 (2000).
- [85] Greywall, D. and Busch, P. *Review of Scientific Instruments* **60**, 471 (1989).
- [86] Bat'ko, I., Flachbart, K., Somora, M., and Vanický, D. *Cryogenics* **35**, 105 (1995).
- [87] Schoepe, W. *Physica B* **165/166**, 299 (1990).
- [88] Watanabe, M., Morishita, M., and Ootuka, Y. *Cryogenics* **41**, 143 (2001).
- [89] Mott, S. *Conduction in non-crystalline materials*. Oxford University Press, (1993).
- [90] Mott, S. *Nobel Lecture* (1977).
- [91] Ambegaokar, V., Halperin, B., and Langer, J. *Physical Review B* **4**, 2612 (1971).
- [92] Pike, G. and Seager, C. *Journal of Applied Physics* **48**, 5152 (1977).
- [93] Affronte, M., Campani, M., Piccinini, S., Tamborin, M., Morten, B., M. Prudenziati, and Laborde, O. *Journal of Low Temperature Physics* **109**, 461 (1997).
- [94] Efros, A. and Shklovskii, B. *Journal of Physics C: Solid State Physics* **8**, L49 (1975).
- [95] Abe, O. and Taketa, Y. *Journal of Physics D: Applied Physics* **24**, 1163 (1991).
- [96] Ast, C. R., Assig, M., Ast, A., and Kern, K. *Rev. Sci. Instrum.* **79**, 093704 (2008).
- [97] Pohl, D. *IBM Journal of Research and Developement* **30**, 417 (1986).
- [98] Okano, M., Kajimura, K., Wakiyama, S., Sakai, F., Mizutani, W., and Ono, M. *Journal of Vacuum Science and Technology A* **5**, 3313 (1987).
- [99] Krapf, P., Lainé, J., Robach, Y., and Porte, L. *Journal de Physique III* **5**, 1871 (1995).
- [100] Rost, M. and *et al.* *Review of Scientific Instruments* **76**, 053710 (2005).
- [101] Croft, D. and Devasia, S. *Review of Scientific Instruments* **70**, 4600 (1999).
- [102] Chen, C. *Introduction to scanning tunneling microscopy*. Oxford University Press, (1993).
- [103] Park, S. and Quate, C. *Review of Scientific Instruments* **58**, 2010 (1987).
- [104] Libioulle, L., Radenovic, A., Bystrenova, E., and Dietler, G. *Review of Scientific Instruments* **74**, 1016 (2003).

- [105] Bott, M., Michely, T., and Comsa, G. *Review of Scientific Instruments* **66**, 4135 (1985).
- [106] Behler, S., Rose, M., Dunphy, J., Ogletree, D., Salmeron, M., and Chapelier, C. *Review of Scientific Instruments* **68**, 2479 (1997).
- [107] Inman, D. *Engineering Vibration*. Prentice Hall.
- [108] Hibbeler, R. *Engineering Mechanics - Dynamics*. Prentice Hall, (2006).
- [109] Dorf, R. and Bishop, R. *Modern Control Systems*. Prentice Hall, (2001).
- [110] Bathe, K. *Finite Element Procedures*. Prentice Hall, (1996).
- [111] Hagedorn, P. and DasGupta, A. *Vibration and Waves in Continuous Mechanical Systems*. John Wiley & Sons, (2007).
- [112] Olesinski, R., Gokhale, A., and Abbaschian, G. *Bulletin of Alloy Phase Diagrams* **10**, 635 (1989).
- [113] Athenstaedt, W. and Leisch, M. *Applied Surface Science* **94**, 403 (1996).
- [114] Burns, N. *Journal of Failure, Analysis and Prevention* **9**, 461 (2009).
- [115] Mashoff, T., Pratzer, M., and Morgenstern, M. *Review of Scientific Instruments* **80**, 053702 (2009).
- [116] Richardson, R. and Smith, E., editors. *Experimental techniques in condensed matter physics at low temperatures*. Addison Wesley Longman, Inc., (1998).
- [117] Kirk, W. and Twerdochlib, M. *Review of Scientific Instruments* **49**, 765 (1978).
- [118] Ast, C., Henk, J., Ernst, A., Moreschini, L., Falub, M., Pacilé, D., Bruno, P., Kern, K., and Grioni, M. *Physical Review Letters* **98**, 186807 (2007).
- [119] Bychkov, Y. and Rashba, E. *JETP Letters* **39**, 78 (1984).
- [120] Ast, C., Wittich, G., Wahl, P., Vogelgesang, R., Pacilé, D., Falub, M., Moreschini, L., Papagno, M., Grioni, M., and Kern, K. *Physical Review B* **75**, 201401 (2007).
- [121] Bihlmayer, G., Blügel, S., and Chulkov, E. V. *Physical Review B* **75**, 195414 (2007).
- [122] Reinert, F. and Nicolay, G. *Applied Physics A: Materials Science & Processing* **78**, 817 (2004).
- [123] Ibach, H. *Physics of Surfaces and Interfaces*. Springer, (2006).
- [124] Chen, W., Madhavan, V., Jamneala, T., and Crommie, M. *Physical Review Letters* **80**, 1469 (1998).

-
- [125] Bürgi, L., Brune, H., and Kern, K. *Physical Review Letters* **89**, 176801 (2002).
- [126] Repain, V., Berroir, J., Rousset, S., and Lecoeur, J. *Applied Surface Science* **162-163**, 30 (2000).
- [127] Vitali, L., Wahl, P., Schneider, M., Kern, K., Silkin, V., Chulkov, E., and Echenique, P. *Surface Science* **523**, L47 (2003).
- [128] Kiss, T., Yokoya, T., Chainani, A., Shin, S., Hanaguri, T., Nohara, M., and Takagi, H. *Nature Physics* **3**, 720 (2007).
- [129] Guillaumon, I., Suderow, H., Vieira, S., Cario, L., Diener, P., , and Rodière, P. *Physical Review Letters* **101**, 166407 (2008).
- [130] Noat, Y., Cren, T., Debontridder, F., Roditchev, D., Sacks, W., Toulemonde, P., and Miguel, A. S. *Physical Review B* **82**, 014531 (2010).
- [131] Matthias, B., Geballe, T., and Compton, V. *Reviews of Modern Physics* **35**, 1 (1963).
- [132] Guillaumon, I., Suderow, H., Vieira, S., and Rodiere, P. *Physica C* **468**, 537 (2008).
- [133] Bose, S., Garcia-Garcia, A., Ugeda, M., Urbina, J., Michaelis, C., Brihuega, I., and Kern, K. *Nature Materials* **9**, 550 (2010).
- [134] Radebaugh, R. and Keesom, H. *Physical Review* **149**, 209 (1966).
- [135] Radebaugh, R. and Keesom, H. *Physical Review* **149**, 217 (1966).
- [136] Valla, T., Pervan, P., and Milun, M. *Surface Science* **307**, 843 (1994).
- [137] Naaman, O., Teizer, W., and Dynes, R. *Physical Review Letters* **87**, 097004 (2001).
- [138] Naaman, O. and Dynes, R. *Solid State Communications* **129**, 299 (2004).
- [139] Haviland, D., Harada, Y., Delsing, P., Chen, C., and Claeson, T. *Physical Review Letters* **73**, 1541 (1994).
- [140] Pashkin, Y., Im, H., Leppäkangas, J., Li, T., Astafiev, O., Jr., A. A., Thuneberg, E., and Tsai, J. S. *Physical Review B* **83**, 020502(R) (2011).
- [141] Devoret, M., Esteve, D., Grabert, H., Ingold, G., Pothier, H., and Urbina, C. *Physical Review Letters* **64**, 1824 (1990).
- [142] Ingold, G., Grabert, H., and Eberhardt, U. *Physical Review B* **50**, 395 (1994).
- [143] Wiesendanger, R. *Reviews of Modern Physics* **81**, 1495 (2009).
- [144] Diekhöner, L., Schneider, M., Baranov, A., Stepanyuk, V., Bruno, P., and Kern, K. *Physical Review Letters* **90**, 236801 (2003).

- [145] Repetto, D., Lee, T., Rusponi, S., Honolka, J., Kuhnke, K., Sessi, V., Starke, U., Brune, H., Gambardella, P., Carbone, C., Enders, A., and Kern, K. *Physical Review B* **74**, 054408 (2006).
- [146] Krause, S., Berbil-Bautista, L., Herzog, G., Bode, M., and Wiesendanger, R. *Science* **317**, 1537 (2007).
- [147] Tedrow, P. and Meservey, R. *Physical Review B* **7**, 318 (1973).
- [148] Harris, E. and Mapother, D. *Physical Review* **165**, 522 (1968).
- [149] Poza, M., Bascones, E., Rodrigo, J., Agrait, N., Vieira, S., and Guinea, F. *Physical Review B* **58**, 11173 (1998).
- [150] Suderow, H., Bascones, E., Belzig, W., Guinea, F., and Vieira, S. *Europhysics Letters* **50**, 749 (2000).
- [151] Martinez-Samper, P., Rodrigo, J., Rubio-Bollinger, G., Suderow, H., Vieira, S., Lee, S., and Tajima, S. *Physica C* **385**, 233 (2003).
- [152] Meservey, R., Tedrow, P., and Bruno, R. *Physical Review B* **11**, 4224 (1975).
- [153] Maki, K. *Progress of Theoretical Physics* **32**, 29 (1964).
- [154] Worledge, D. and Geballe, T. *Physical Review B* **62**, 447 (2000).
- [155] Oka, H., Ignatiev, P., Wedekind, S., Rodary, G., Niebergall, L., Stepanyuk, V., Sander, D., and Kirschner, J. *Science* **327**, 843 (2010).
- [156] Pietzsch, O., Kubetzka, A., Bode, M., and Wiesendanger, R. *Physical Review Letters* **92**, 057202 (2004).
- [157] Kane, B. *Nature* **393**, 133 (1998).
- [158] Balatsky, A., Fansson, J., Mozyrsky, D., and Manassen, Y. *Physical Review B* **73**, 184429 (2006).
- [159] Delgado, F. and Fernández-Rossier, J. *arXiv cond-mat* , 1101.4772v1 (2011).

Curriculum Vitae

Personal Information

Date of birth 26.04.1980
Place of birth Weimar, Germany
Nationality Germany

Recent activities

2006-2011 PhD Thesis, at the Max-Planck-Institute for Solid State Research in Stuttgart in the department of Prof. Klaus Kern
Development and setup of a Millikelvin Scanning Tunneling Microscope for Applications in Ultra High Vacuum and High Magnetic Fields

Studies

2000-2005 Physics, Technische Universität Berlin.
Main focus, Solid State Physics, Surface Science
Projects, Setup of an Apertureless Scanning Nearfield Optical Microscope (Diploma thesis)

Community Service

1999-2000 Community Service at the St. Josephs hospital in Potsdam

School education

1992-1999 High School, High School of sports "Friedrich Ludwig Jahn" in Potsdam with the grade of general qualification of university entrance (Abitur)
1991-1992 Elementary School, attendance of the elementary school 23 in Potsdam
1886-1991 Elementary School, attendance of the elementary school "Pablo Neruda" in Potsdam

Additional Activities

2000-2006 Research Assistant, Escotec Lasertechnik GmbH
Teltow, Germany

Acknowledgments

During the work of my thesis I received support from a lot of people to whom I want to address thanks:

- I am grateful to *Prof. Klaus Kern* for giving me the opportunity and the honor to work in his group at the Max-Planck-Institute in Stuttgart and for the great support during the different stages of the mK-STM project.
- Many thanks I want to address to *Dr. Christian Ast*. His excellent supervision, motivation and guidance often kept me from getting lost in details.
- To *Peter Andler, Andreas Koch and Wolfgang Stiepany* for professional technical support. The speed and accuracy with which technical solutions and ideas were realized was impressive.
- *Dr. Markus Etzkorn* and *Dr. Markus Ternes* for very good company in the lab and many stimulating discussions.
- I thank the *low temperature service group, the mechanical workshops, the supply store, the library and the computer service* for their great efforts to solve the major and the minor problems that come along on a scientist's day.
- The members of the Emmy group at the Max-Planck-Institute *Isabella, Carola, Fabian, Hadj* and all friends and members in the Kern group for a great time in Stuttgart.
- Last, but not least I want to thank my family for their encouragement.